


July 2019

## MODIFICATION OF 2D MATERIALS UTILIZING FUNCTIONAL POLYMER INTERFACIAL LAYERS

Ryan Selhorst

Follow this and additional works at: [https://scholarworks.umass.edu/dissertations\\_2](https://scholarworks.umass.edu/dissertations_2)

 Part of the [Materials Chemistry Commons](#), [Organic Chemistry Commons](#), [Physical Chemistry Commons](#), and the [Polymer Chemistry Commons](#)

---

### Recommended Citation

Selhorst, Ryan, "MODIFICATION OF 2D MATERIALS UTILIZING FUNCTIONAL POLYMER INTERFACIAL LAYERS" (2019). *Doctoral Dissertations*. 1549.  
[https://scholarworks.umass.edu/dissertations\\_2/1549](https://scholarworks.umass.edu/dissertations_2/1549)

This Open Access Dissertation is brought to you for free and open access by the Dissertations and Theses at ScholarWorks@UMass Amherst. It has been accepted for inclusion in Doctoral Dissertations by an authorized administrator of ScholarWorks@UMass Amherst. For more information, please contact [scholarworks@library.umass.edu](mailto:scholarworks@library.umass.edu).

**MODIFICATION OF 2D MATERIALS UTILIZING FUNCTIONAL POLYMER  
INTERFACIAL LAYERS**

A Dissertation Presented

by

**RYAN C. SELHORST**

Submitted to the Graduate School of the  
University of Massachusetts Amherst in partial fulfillment  
of the requirements for the degree of

**DOCTOR OF PHILOSOPHY**

May 2019

Polymer Science & Engineering

© Copyright by Ryan C. Selhorst 2019

All Rights Reserved

**MODIFICATION OF 2D MATERIALS UTILIZING FUNCTIONAL POLYMER  
INTERFACIAL LAYERS**

A Dissertation Presented

by

**RYAN C. SELHORST**

Approved as to style and content by:

---

Todd S. Emrick, Chair

---

E. Bryan Coughlin, Member

---

Michael D. Barnes, Member

---

E. Bryan Coughlin, Department Head  
Polymer Science & Engineering

## **DEDICATION**

*To my **Family** - A constant source of unconditional love, inspiration, and imagination.*

*And to **Temperance** - The most compassionate and loving soul I have had the privilege to know.*

## ACKNOWLEDGMENTS

I thank my thesis advisor, Todd Emrick for, among many things, proving that all this time spent learning the ins-and-outs of polymer chemistry and a firm dedication to an education yield a fruitful career. You have been a one-of-kind mentor, guiding me throughout my graduate school experience and providing a grounding voice of reason that has and will continue to echo in my professional life. I also thank my committee members Bryan Coughlin and Michael Barnes for offering their expertise to my research as well as my professional career. Many times, both Bryan and Mike have challenged me to probe further into the depths of my work always asked me the difficult questions, forcing me to either see the bigger picture or understand the very fine details. I thank you all very much and can't express my gratitude enough at having great scientists on my committee.

I acknowledge the sources of funding that have supported the research that is featured in this dissertation, including the National Science Foundation (NSF) Materials Research Science & Engineering Center (MRSEC) on Polymers (DMR-0820506), NSF grant (NSF-CHE-1506839), NSF grant (NSF-DMR-1808011), and the U.S. Department of Education Graduate Assistance in Areas of National Need (GAANN) Fellowship.

I want to acknowledge Dr. Ashwin Ramasubramaniam, Dr. Doron Naveh, Dr. Peijian Wang, Dr. Egle Puodziukinaite, Dr. Raymond Gasper, Hadas Alon, Jeffery Dewey for collaborating with me on this research and significantly enhancing the quality of the science produced. I also want to thank the Polymer Science & Engineering faculty and staff for consistently providing me guidance in my research, ensuring smooth transitions in the bureaucratic side of graduate school, and always giving me much needed comic relief.

I extend my deepest gratitude to the Emrick group both past and present for being great friends and an awesome graduate school family, it would have been much harder to get through graduate school without you. I want to especially thank Zak Page, Rachel Letteri, Egle Puodziukinaite, Matt Skinner, Stephen Strassburg, Andreas Kourouklis, Jack Ly, Kara Martin, Cristiam Santa, Nick Posey, Marcus Cole, Ned Burnett, Ben Cherniowski, Steve Rosa, Christian Steinmetz, and Marcel Brown. I must thank the members of the Drunken Chickens softball team and our awesome winning 2017 season. I also thank Marcus Cole, Matt Skinner, and Ben Blodgett for being the best ragtag team of Sunday golfers Amherst had to offer. Furthermore, I want to thank those same people and Stephen Strassburg for our Sunday night bowling leagues when it got too cold to golf. I thank my mom and dad Deborah and Chris Selhorst for being the best people I know. They have always been so supportive and loving and continually get me through challenging moments in my life with their wisdom and kind words. Thank you to my sister Jennifer who always makes me laugh and I am lucky to have a big sister who has the best life experiences to share with me all the time. Thank you to the Amherst Starbucks staff who also have kept me running (literally) with coffee and supplying a great workspace for writing and meeting wonderful people especially Ralph and Ted who are constant sources of intriguing conversation. Finally, I thank Temperance Dewar for making me a better person, always expanding my mind, showing me how to be an open and accepting individual. You are a constant source of love and imagination and have brightened my days by being one of the most influential individuals in my life.

## ABSTRACT

### MODIFICATION OF 2D MATERIALS UTILIZING FUNCTIONAL POLYMER INTERFACIAL LAYERS

May 2019

RYAN SELHORST, B.S., WRIGHT STATE UNIVERSITY

M.S., UNIVERSITY OF MASSACHUSETTS AMHERST

Ph.D., UNIVERSITY OF MASSACHUSETTS AMHERST

Directed by: Professor Todd S. Emrick

This dissertation describes the modification of 2D transition metal dichalcogenides (TMDCs). These materials exhibit unique electronic properties, ranging from metallic to insulating, and can transport either electrons (n-type) or holes (p-type). Polymers containing electronically-active moieties offer a path to control the electronic properties of a 2D material without altering the inherent structure of the semiconductor. This dissertation focuses on the synthesis of polymers bearing chalcogen-rich or zwitterionic moieties to alter the electronic and solution properties of 2D materials.

Chapter 2 describes polymers containing sulfur-rich tetrathiafulvalene (TTF) and their effects as electroactive coatings on the TMDC molybdenum disulfide ( $\text{MoS}_2$ ). These polymers were anticipated to not only promote adhesion to  $\text{MoS}_2$  through sulfur-sulfur interactions but also modify the work function of the semiconductor through the donation



of electrons at the semiconductor/polymer interface. TTF polymers were synthesized by ring-opening metathesis copolymerization (ROMP) and reversible addition fragmentation chain transfer (RAFT) polymerization. TTF polymers stabilize suspensions of chemically exfoliated MoS<sub>2</sub> nanosheets, contrary to a pyrene-substituted polymer of similar structure, demonstrating the importance of a sulfur-rich structure for interaction with MoS<sub>2</sub>. Kelvin probe force microscopy (KPFM) was used to examine the shift in work function after a thin polymer layer was applied to MoS<sub>2</sub> which revealed a *decrease* in work function by 0.24 eV, expected for n-doping.

Chapter 3 examines the complementary case to TTF—doping with a sulfur rich electron acceptor bithiazolidinylidene (BT). Functional BT monomers were synthesized by the reaction of a primary amine with carbon disulfide and dimethylacetylene dicarboxylate. BT-containing polymers were then accessed by condensation of a BT-diol with hexamethylene diisocyanate to form polyurethanes. The polymers exhibited thermal stability and solubility in an array of solvents and, upon coating single layer MoS<sub>2</sub> grown by chemical vapor deposition (CVD), the SPC decreased by 0.16 V, signifying an *increase* work function and confirming p-doping.

Chapter 4 progresses the previous two chapters through the analysis of the underlying substrate and its role in the efficacy of doping MoS<sub>2</sub> with small molecules TTF and BT. CVD grown MoS<sub>2</sub> on silicon oxide (SiO<sub>2</sub>) and aluminum oxide (Al<sub>2</sub>O<sub>3</sub>, sapphire) were coated with thin layers of TTF and BT and the change in work function was monitored by KPFM. MoS<sub>2</sub> on Al<sub>2</sub>O<sub>3</sub> showed a work function *decrease* of 1.24 eV when coated with TTF, displaying a remarkable increase in the efficacy of n-doping compared to using SiO<sub>2</sub> as the underlying dielectric. Similarly, when coated with BT, MoS<sub>2</sub> with Al<sub>2</sub>O<sub>3</sub> as the

dielectric displayed a 0.8 eV *increase* in the work function representing a four-fold increase in the magnitude of work function shift when compared to using SiO<sub>2</sub> as the underlying substrate. We rationalize this increase in the efficacy of doping MoS<sub>2</sub> by an increase in the static polarizability of the substrate when using Al<sub>2</sub>O<sub>3</sub> causing a decrease in the effective measured dipole screening being probed at the dopant/semiconductor interface.

Chapter 5 concludes with the development of zwitterionic photoresists used to simultaneously pattern and dope 2D materials. We developed a novel photoresist composed of zwitterionic poly(sulfobetaine methacrylate) (PSBMA) copolymers with methyl methacrylate and implemented these photoresist in the fabrication of graphene transistors. Multiple copolymers were synthesized by conventional free-radical polymerization in trifluoroethanol with feed ratio matching experimental incorporations. These zwitterionic photoresists displayed resolutions approaching 100 nm, matching conventional methacrylic photoresists. Transistors were fabricated on CVD-grown single layer graphene deposited on p-type Si/SiO<sub>2</sub> and the polymer was used to pattern over the device to afford multiple, unique devices on a single graphene flake. Polymer covered devices showed n-doping indicated by a shift in the charge neutrality point in the current-voltage curves. Furthermore, a single device with polymer covering half of the device exhibited p-n junction characteristics (high on currents at high gate biases) demonstrating the ease of fabrication of these devices using this class of polymer photoresists.

## TABLE OF CONTENTS

	Page
ACKNOWLEDGMENTS .....	v
ABSTRACT .....	vii
LIST OF TABLES .....	xii
LIST OF FIGURES .....	xiii
CHAPTER	
1.TWO DIMENSIONAL MATERIALS AND THEIR MODIFICATION WITH ORGANIC MOIETIES.....	1
1.1 Introduction.....	1
1.1.1 Synthesis of TMDCs.....	3
1.1.2 Electronic Behavior of TMDCs.....	6
1.1.3 Defect and Interfacial Engineering.....	9
1.1.4 Doping of Semiconducting TMDCs.....	10
1.2 Thesis Outline .....	12
1.3 References.....	16
2.TETRATHIAFULVALENE-CONTAINING POLYMERS FOR THE MODIFICATION OF MoS <sub>2</sub> .....	21
2.1 Introduction.....	21
2.2 Synthesis of TTF-Containing Polymers .....	23
2.3 Electrochemistry of TTF Compounds .....	26
2.4 Solution Behavior of Polymer/MoS <sub>2</sub> Suspensions .....	29
2.5 Theoretical Considerations .....	32
2.6 Electronic Interactions of TTF Polymers With MoS <sub>2</sub> .....	36
2.7 Conclusions.....	39
2.8 References.....	40
3.BITHIAZOLIDINYLDENE POLYMERS AS P-DOPANTS FOR MoS <sub>2</sub> .....	43
3.1 Introduction.....	43
3.2 Synthesis of Functional BT Monomers and Polymers .....	44
3.3 BT Stability .....	47
3.4 Electronic Impacts of BT Polymers on MoS <sub>2</sub> .....	50
3.5 Electrochemistry of BT Polymers.....	51
3.6 Conclusions.....	53
3.7 References.....	55
4. BIDIRECTIONAL DOPING OF MoS <sub>2</sub> AND THE ROLE OF THE SUBSTRATE....	57
4.1 Introduction.....	57

4.2 Optical Characterization of MoS <sub>2</sub> .....	58
4.3 Synthesis of BT and KPFM Studies on Doped MoS <sub>2</sub> .....	59
4.4 Mechanism of Substrate Influence on Doping MoS <sub>2</sub> .....	65
4.6 Conclusions.....	66
4.7 References.....	68
5. ZWITTERIONIC PHOTORESISTS FOR SIMULTANEOUS PATTERNING AND DOPING OF GRAPHENE.....	71
5.1 Introduction.....	71
5.2 Synthesis of Polymer Zwitterions.....	73
5.3 PSBMA-co-PMMA Photoresists: Optimization and Spectroscopy .....	75
5.4 Graphene Field-Effect Transistors and Doping .....	78
5.5 Theoretical Insights on the Zwitterion/Graphene Interface .....	82
5.6 Conclusions.....	84
5.7 References.....	85
6. OUTLOOK .....	87
6.1 Doping <i>via</i> Polymer Coordination Complexes .....	87
6.2 Covalent Organoselenium Doping of TMDCs .....	91
6.3 Polymer Zwitterion for Bidirectional Doping of 2D Materials .....	93
6.4 References.....	95
7. EXPERIMENTAL SECTION .....	97
7.1 Materials .....	97
7.2 Instrumentation.....	98
7.3 Methods .....	100
7.4 References.....	143
BIBLIOGRAPHY.....	145

## LIST OF TABLES

Table	Page
2.1. Summary of polymer characterizations for the TTF methacrylate series .....	26
2.2. Summary of results from DFT calculations .....	33
3.1. Summary of reduction potentials for functional BT monomer and polymers .....	53

## LIST OF FIGURES

Figure	Page
1.1. (A) Layered structure of TMDCs showing the individual layers stacking, held together through van der Waals interactions. (B) Unit cell of the semiconducting 2H phase of TMDCs. (C) Unit cell of the metallic 1T phase of TMDCs.....	2
1.2. Diagram of a CVD furnace for the growth of TMDCs showing the relative positions of the precursor materials for successful growth of layer-controlled TMDCs. ....	4
1.3. Illustration of chemical exfoliation of TMDC via lithium intercalation chemistry.....	5
1.4. (A) Energy band diagram showing the evolution of the band gap of MoS <sub>2</sub> moving from an indirect gap of 1.2 eV at bulk thicknesses (a) to a direct gap of 1.8 eV at monolayer thickness (d). (B) Depiction of the real space lattice of MoS <sub>2</sub> and the first Brillouin zone highlighting the symmetry points in momentum space ( $\Gamma$ , M, and K) Figure 1.4a was reprinted with permission from Nano Letters, ref. 43, copyright 2010 American Chemical Society.....	7
1.5. Diagram of the active Raman signatures ( $E_{2g}$ and $A_{1g}$ ) stemming from in-plane and out-of-plane vibrations.....	8
1.6. Depiction of the two types of defects found in TMDCs (left) line defects in the form of grain boundaries and (right) point defects in the form of chalcogen vacancies....	9
1.7. (A) Cartoon showing non-covalent functionalization of TMDC through physisorption of organic molecules and polymers. (B) Covalent functionalization of TMDCs by backfilling chalcogen vacancies with organic thiols.....	11
2.1. Synthesis of TTF-containing polymers by ROMP copolymerization of TTF-NB and hexyl-NB.....	23
2.2. (A) Kinetics of ROMP copolymerization showing linear monomer consumption with time and low PDIs, indicative of living polymerization. (B) Gel permeation chromatograph of polymer <b>P1a</b> displaying a monomodal molecular weight distribution. (C) <sup>1</sup> H NMR spectroscopy of polymer <b>P1e</b> showing the TTF and norbornene backbone olefin resonances .....	24
2.3. Synthesis and post-polymerization modification of polymers <b>P3a-h</b> to afford <b>P4a-h</b> .....	25

2.4. (A) Cyclic voltammograms of small molecules TTF (black) and a model compound methoxyethyl TTF (blue) showing two reversible oxidation potentials. (B) Cyclic voltammograms of polymers <b>P1e</b> (norbornene) and <b>P4d</b> (methacrylate) depicting the absence of a second oxidation for the norbornene backbone and suppression of the second oxidation for the methacrylate backbone .....	27
2.5. Spectroelectrochemistry traces of TTF showing the evolution of the UV-Vis spectrum over time. At low potentials, the TTF radical cation and dimer dication absorbances appear and at high potentials the dication species appears .....	28
2.6. (A) AFM scan and 3D rendition of MoS <sub>2</sub> nanosheets prepared by liquid exfoliation in NMP. (B) High resolution transmission electron microscopy of MoS <sub>2</sub> nanosheets prepared by liquid exfoliation and (C) chemically exfoliated MoS <sub>2</sub> prepared by lithium intercalation showing distinct differences in the pristine 2H and the defective 1T phases.....	29
2.7. Photographs of suspensions containing chemically exfoliated MoS <sub>2</sub> nanosheets with polymers <b>P1a-e</b> and a negative control (-) containing no polymer and positive control (+) containing poly(norbornene) with no TTF). The photos were taken a different times (A) immediately after redispersion in THF (B) 2 days, (C) 4 days, and (D) 8 days. Optical micrographs showing (E) aggregated nanosheets from control suspensions and (F) dispersed nanosheets from suspensions containing TTF polymers.....	30
2.8. (Left) Photographs of MoS <sub>2</sub> nanosheets before and after redispersion in THF with and without TTF polymers. (Right): FT-IR of MoS <sub>2</sub> , Polymer <b>P4d</b> , and MoS <sub>2</sub> nanosheets with TTF polymer <b>P4d</b> showing the persistence of polymer on the nanosheets after rinsing the nanosheets several times .....	31
2.9. Results of DFT calculations for TTF on MoS <sub>2</sub> in three scenarios: TTF on pristine MoS <sub>2</sub> (a,b), TTF on MoS <sub>2</sub> with a sulfur vacancy (c,d) and TTF dimer on pristine MoS <sub>2</sub> . Figures a,c, and e are isosurfaces with the cyan representing charge depletion and yellow representing charge accumulation. Figures b,d, and f are density of states plots shown before and after adsorption of TTF to MoS <sub>2</sub> .....	32
2.10. Comparison of the two methods used for DFT calculations (A) optB86b and (B) Heyd-Scuseria-Ernzerhof (HSE) hybrid-DFT functional .....	35
2.11. Time-resolved UV-Vis spectroscopy of MoS <sub>2</sub> nanosheets in the presence of (A) small molecule TTF and (B) polymer <b>P4a</b> .....	36
2.12. (Left) Physical representation of KPFM as a scan probe technique and (Right) a simple band diagram showing the equalization of work functions of the sample and the tip with the voltage required to maintain this balance recorded as surface potential contrast (SPC) .....	37

2.13. KPFM SPC images before and after addition of TTF polymers and their corresponding histograms showing an increase in the SPC and representing n-doping of MoS <sub>2</sub> .....	38
3.1. (A) <sup>13</sup> C NMR of BT-diol and Polymer <b>P5b</b> showing the BT (195, 167, and 124 ppm) and urethane (157 ppm) resonances. (B) Gel permeation chromatograph showing the monomodal molecular weight distribution from polymer <b>P5c</b> .....	47
3.2. (A) UV-Vis spectrum of BT-diol showing degradation after heating at 100 °C for 24 hrs. (B) UV-Vis spectrum of BT-diol after heating in 10 °C increments up to 95 °C showing that degradation begins at 65-75 °C. (C) UV-Vis spectrum of Polymer <b>P5c</b> showing degradation after heating at 100 °C for 48 hrs. (D) Thin film UV-Vis of polymer <b>P5b</b> showing no degradation after 48 hrs. and the appearance of a new peak at 380 nm. ....	48
3.3. (A) <sup>1</sup> H NMR spectra of allyl-BT before and after heating a 100 °C in DMSO-d <sub>6</sub> showing the appearance of a new methylene resonance. (B) <sup>13</sup> C NMR spectra of allyl-BT before and after heating a 100 °C in DMSO-d <sub>6</sub> showing the appearance of a new carbamate and olefin resonances suggesting breaking of molecular symmetry.....	49
3.4. Small angle x-ray scattering (SAXS) diffractogram of polymer <b>P5b</b> showing the evolution of the domain size from 5 nm to 10 nm after annealing at 100 °C for 24 hrs.....	50
3.5. (A) KPFM of MoS <sub>2</sub> on Si/SiO <sub>2</sub> before and after coating with polymer <b>P5b</b> and the corresponding SPC histograms showing a 0.22 eV decrease after coating, indicative of p-doping. (B) SPC image and histograms showing the recovery of the MoS <sub>2</sub> work function after rinsing the polymer from the MoS <sub>2</sub> flake.....	51
3.6. (Left) Cyclic voltammograms of BT-diol, methoxyethyl BT and polymer <b>P5c</b> (Center) Energy band diagram constructed from the redox potentials and band gap from the UV-Vis traces indicating non-favorable overlap for ground state charge transfer. (Right) Energy band diagram showing the potential mechanism of doping do to aggregation induced bandgap closure and intrinsically n-doped MoS <sub>2</sub> .....	53
4.1. Cartoon depicting the scope of the experiments in this chapter using TTF and BT as dopants for single layer MoS <sub>2</sub> with control over the dielectric to probe the influence of the substrate on doping efficacy. ....	59
4.2. Raman spectrum of MoS <sub>2</sub> on (Top) SiO <sub>2</sub> /Si and (Bottom) sapphire showing the two active in-plane (E <sub>2g</sub> ) and ou-of-plane (A <sub>1g</sub> ) stretches .....	60
4.3. (A) Synthesis of BT derivative by the addition of DMAD to a stirring solution of a primary amine and carbon disulfide. (B) Two isomers ( <i>cis</i> and <i>trans</i> ) hypothesized to result from the reaction of methylamine with carbon disulfide and DMAD.....	61



4.4. (A) SPC images of single layer MoS <sub>2</sub> on SiO <sub>2</sub> /Si (left) and sapphire (right) before (top) and after (bottom) coating with TTF showing a SPC increase after coating and a more significant change on sapphire vs. SiO <sub>2</sub> /Si indicating n-doping. B) SPC images of single layer MoS <sub>2</sub> on SiO <sub>2</sub> /Si (left) and sapphire (right) before (top) and after (bottom) coating with BT showing a SPC decrease after coating and a more significant change on sapphire vs. SiO <sub>2</sub> /Si indicating p-doping .....	62
4.5. SPC images of single layer MoS <sub>2</sub> with (A) before doping and (B) after rinsing dopant of the substrate. (C) The resultant SPC histograms before doping and after rinsing the dopant off of the substrate with methanol showing the recovery of the original work function .....	63
4.6. (A) A summary of the changes in SPC of single layer MoS <sub>2</sub> before and after doping with TTF, methyl BT, and butyl BT. The left portion shows the results of doping with TTF and BTs on SiO <sub>2</sub> /Si and the right portion shows the results from doping MoS <sub>2</sub> with TTF and BTs on sapphire. (B) PL spectra of single layer MoS <sub>2</sub> on SiO <sub>2</sub> /Si before drop-casting dilute solutions of TTF and BT and after one and two additions of TTF and BT showing wavelength shifts corresponding to n- or p-doping, insets show the MoS <sub>2</sub> B peak. The colors of the curves correspond to consecutive additions of dopants: <i>Blue</i> is uncoated MoS <sub>2</sub> , <i>Red</i> is after a single addition of dopant, and <i>Pink</i> is after a second addition of dopants .....	64
4.7. Physical picture of dipole and induced static polarization for the work function shift in MoS <sub>2</sub> after doping with TTF. Left: TTF donates electrons through charge transfer to MoS <sub>2</sub> . Right: BT accepts electrons from MoS <sub>2</sub> . The transfer of electrons gives rise to dipoles between TTF and MoS <sub>2</sub> and corresponding induced dipoles from static charge at the dielectric/semiconductor interface. This polarized static charge effectively screens the measured work function of MoS <sub>2</sub> and the screening strength will vary with dielectric constant of the underlying substrate .....	66
5.1. Outline of the implementation of the polymer zwitterion PSBMA-co-PMMA as a functional photoresist that is used to simultaneously pattern and dope graphene .....	74
5.2. (A) Scheme showing the synthesis of PSBMA-co-PMMA by conventional free-radical polymerization. (B) <sup>1</sup> H NMR spectra of PSBMA-co-PMMA confirming the successful synthesis of the polymer, specifically noting the sulfobetaine resonances indicated by the colored ovals. (C) Gel Permeation Chromatography in trifluoroethanol of PSBMA-co-PMMA showing high molecular weight and a monomodal molecular weight distribution. ....	75

- 5.3. (A) Scanning Electron Micrograph of a PSBMA-co-PMMA polymer film after e-beam lithography and development showing the dependence of resolution on electron beam power. (B) Atomic Force Micrograph of line patterns after development with the corresponding height profile showing the high fidelity with which these patterns can be fabricated .....76
- 5.4. (A) Optical micrograph of single layer CVD graphene coated with PSBMA-co-PMMA in which half of the polymer film was developed such that the left side is bare graphene and the right side is polymer coated. (B) Visualization of the vibration responsible for the Raman G-band – the probe for molecular doping. (C) Band diagram of graphene showing the appearance of the G-band vibration by a Raman active optical phonon relaxation. (D) Raman mapping of the border between bare and polymer-coated graphene and the corresponding spectra (E) showing the Raman upshift due to PSBMA doping of graphene.....77
- 5.5. Raman spectra of bare graphene and PSBMA-co-PMMA before (Top) and after (Bottom) coating the polymer on the graphene bar showing that there is no interference of the polymer with the G-band of graphene and that successful n-doping is taking place after polymer coating.....78
- 5.6. (A) Diagram of a field-effect transistor, specifically the setup used for the device studies in the chapter. (B) Graphene band structure showing the charge neutrality point at the Dirac point in pristine undoped graphene, however, the position changes depending on the type of dopants introduced onto graphene.....79
- 5.7. (A) Optical micrograph of five graphene FETs either bare graphene (1,2), PSBMA-co-PMMA coated graphene (3,4) or half-coated (3). (B) Control FET device characteristics showing similar behavior before and after coated with PMMA. (C) Transfer curves for devices 1 and 4 showing a drastic shift in the CNP towards negative gate voltages, indicating n-doping. (D) Transfer curve of device 3 showing high currents above and below the CNP indicative of a p-n junction .....81
- 5.8. (A) DFT calculation showing the equilibrium geometry of a sulfobetaine moiety physisorbed to a graphene lattice showing charge accumulation/depletion due to the charged atoms in the zwitterion. (B) side profile of a sulfobetaine moiety showing the in-plane and out-of-plane components of the dipole moment. (C) Density of states plot indicating an upshift in the Fermi energy after doping toward the conduction band of graphene, visually depicted in (D). .....83
- 6.1. (A) Pre-polymerization coordination of ruthenium(III) chloride to a terpyridine-containing styrene monomer. (B) Attempted free-radical copolymerization of the ruthenium coordinated styrene monomer with styrene that resulted in only starting material after reaction. (C) Copolymerization of styrene-terpyridine with styrene with successful polymer formation confirmed by gel permeation chromatography (D). .....90

- 6.2. (A) Attempted post-polymerization coordination of ruthenium (III) chloride with a terpyridine-containing polymer that resulted in crosslinking. (B) Model small molecule complex formed by the reaction of 1 eq. of ruthenium (III) chloride with 2 eq. of methoxy terpyridine. (C) Model small molecule complex formed by the reaction of 1eq. of gold (III) chloride with 2 eq. of methoxy terpyridine with the reaction producing both mono- and bis-complexes .....91
- 6.3. (A) Degradation pathways of SDZ using heat, light, and base to produce active alkyne selenide anions or radicals. (B) *In situ* functionalization of selenium-based TMDCs with the products of SDZ degradation .....92
- 6.4. (A) Synthesis of semicarbazide HCl and functional semicarbazones as precursors to SDZs. (B) <sup>1</sup>H NMR spectra showing the successful synthesis of precursors .....93
- 6.5. (A) Synthesis of heptyl SDZ from octyl semicarbazone. (B) <sup>1</sup>H NMR spectrum of heptyl SDZ noting the aromatic SDZ resonance at 8.25ppm. (C) <sup>13</sup>C NMR spectrum of heptyl SDZ displaying the two aromatic SDZ resonances at 145 ppm and 168 ppm .....93

## CHAPTER 1

### TWO DIMENSIONAL MATERIALS AND THEIR MODIFICATION WITH ORGANIC MOIETIES

#### 1.1: Introduction

Two-dimensional materials are crystalline substances with thicknesses ranging from single to few atomic layers and composed of either organic and inorganic substituents that are arranged in a two-dimensional structure. These materials possess a wide range of electrical,<sup>1-2</sup> optical,<sup>3-4</sup> and mechanical,<sup>5-6</sup> properties dictated by both structure and composition. One of the most studied 2D materials is graphene, an atomically thin lattice of  $sp^2$  hybridized carbon atoms, first produced by cleavage of graphite to a single layer.<sup>7</sup> Graphene electrically behaves as a metal due to its lack of an energy gap between the valance and conduction bands (*i.e.*, bandgap) and led to an explosion of research implementing it in field-effect transistors (FETs),<sup>8</sup> optoelectronic devices,<sup>9</sup> as well as biomedical devices,<sup>10</sup> chemical sensors,<sup>11</sup> and conductive polymer composites.<sup>12</sup> However, due to the lack of a bandgap, the use of graphene in devices have encountered many issues associated with short circuit and leakage currents, requiring further modification of the material to utilize in electronics.<sup>13</sup> Since the advent of graphene, a plethora of 2D materials have been discovered bearing properties that are advantageous over graphene inciting further exploration of their fundamental material properties.

One such set of 2D materials are transition metal dichalcogenides (TMDCs), a class of two dimensional inorganic materials that are used in a wide variety of applications including electronics,<sup>14</sup> catalysis,<sup>15</sup> and tribology,<sup>16</sup> The structure of TMDCs comprises a layer of transition metal, typically molybdenum or tungsten, bonded in between two

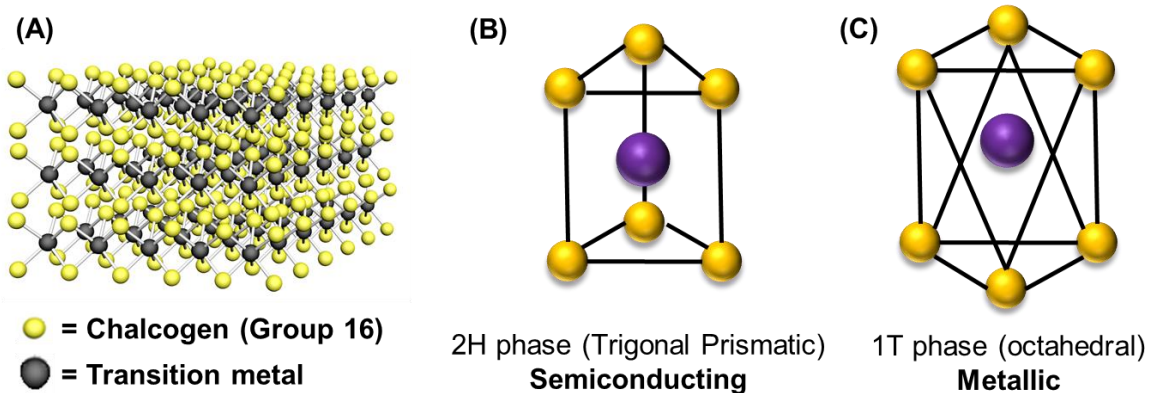


**Figure 1.1.** (A) Layered structure of TMDCs showing the individual layers stacking, held together through van der Waals interactions. (B) Unit cell of the semiconducting 2H phase of TMDCs. (C) Unit cell of the metallic 1T phase of TMDCs.

layers of a group 16 element such as sulfur, selenium, or tellurium (denoted as  $\text{MX}_2$ , where M is a transition metal and X is a chalcogen) (Figure 1.1a). This arrangement yields a two-dimensional structure with a chalcogen-rich basal plane in which the individual layers stack to form a bulk structure through van der Waals interactions. These intermolecular forces give rise to the material's interesting electronic and tribological properties including quantum confinement at single to few layers and low coefficients of friction at few layer to bulk thicknesses, making them useful as solid-state lubricants and grease additives.<sup>17,18</sup>

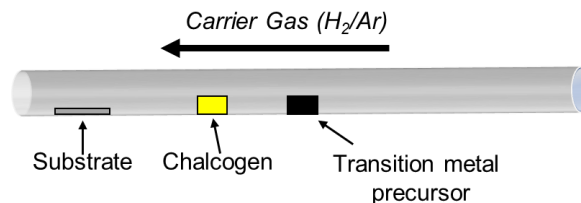
Depending on the growth or processing method, TMDCs occur in several crystallographic structures that impact the resultant electronic properties of the material. For instance, molybdenum disulfide primarily exists in two phases: the 2H phase in which the layers of the material are arranged hexagonally with bonding to the transition metal center adopting trigonal prismatic coordination structure and the 1T phase adopting a tetragonal layer structure and octahedral coordination geometry (Figure 1.1 b, c).<sup>19</sup> The thermodynamically stable 2H phase endows  $\text{MoS}_2$  with semiconducting characteristics while the metastable 1T phase yields  $\text{MoS}_2$  with metallic conduction characteristics. The

phases are interchangeable by chemical,<sup>20</sup> thermal,<sup>21</sup> and optical<sup>22</sup> treatments allowing control over the inherent electronic properties of the TMDC. Phase engineering of TMDCs has led to a broader applicability of the material in both device and catalysis contexts. Chhowalla and coworkers demonstrated that treatment of MoS<sub>2</sub> with *n*-butyl lithium led to a phase change from 2H to 1T, with the 1T phase acting as a more efficient contact layer to gold electrode than the 2H phase.<sup>23</sup> Furthermore, the 1T phase has proven more efficient for catalysis due to the higher conductivity than the 2H phase. The exploration of phase behavior in TMDCs has initiated further synthetic efforts to control structure, phase, and morphology in a scalable manner.

### **1.1.1: Synthesis of TMDCs**

TMDCs can be found naturally as in MoS<sub>2</sub>, which is refined from molybdenite, or be synthesized by chemical vapor deposition (CVD),<sup>24</sup> molecular beam epitaxy (MBE),<sup>25</sup> or chemically using precursors such as MoO<sub>3</sub> or ammonium molybdate ((NH<sub>4</sub>)<sub>6</sub>Mo<sub>7</sub>O<sub>24</sub>) and a source of sulfur, selenium, or tellurium.<sup>20</sup> A large effort has been directed toward the growth of TMDCs by CVD to synthesize pristine materials (*i.e.*, lacking point and edge defects), to fabricate new TMDCs and provide a more scalable and high yielding approach for quality TMDCs.<sup>26</sup> The past 5 years of work on CVD growth has produced a plethora of TMDC compositions, utilizing many of the transition metals and their combinations with chalcogens, each providing new and unexplored material properties.<sup>27</sup> CVD growth entails bulk TMDC powders or a transition metal precursor (typically a metal chloride or oxide) loaded into the center of a furnace with a chalcogen source in a lower temperature area downstream from the precursors. The substrate is placed further downstream from the

**Figure 1.2.** Diagram of a CVD furnace for the growth of TMDCs showing the relative positions of the precursor materials for successful growth of layer-controlled TMDCs.



chalcogens in a zone of the furnace with temperatures favorable for the nucleation and growth of the TMDC crystals (Figure 1.2). Temperatures of up to 1000 °C and a carrier gas of H<sub>2</sub>/Ar mixture are required for the growth large area crystals, with single crystal sizes reaching hundreds of microns in lateral dimensions and monolayer thicknesses (~ 1 nm). CVD produces single crystal TMDCs with the ability to control the number of layers deposited on the substrate and the morphology of the resulting crystals, ranging from triangular to dendritic depending on the growth conditions. The quality of TMDC produced by CVD varies but, in general, affords TMDCs with a low density of defects compared to other hydrothermal or chemical syntheses.

Due to their layered structure, pristine layers and colloiddally stable suspensions of TMDC nanosheets are produced by mechanical<sup>28</sup> or chemical exfoliation,<sup>29</sup> respectively. For mechanical exfoliation, the “Scotch-tape” method is the preferred choice for preparation, involving the attachment of a bulk crystal of the TMDC to the adhesive layer of tape. The tape is then removed from the crystal and placed on a substrate and further peeled away which simultaneously deposits and cleaves layers of the TMDC leaving behind near pristine TMDC crystals suitable for device fabrication. The yield of pristine flakes from mechanical exfoliation is low, and device fabrication on a single isolated flake prepared by mechanical exfoliation is cumbersome, typically used only for fundamental device research.

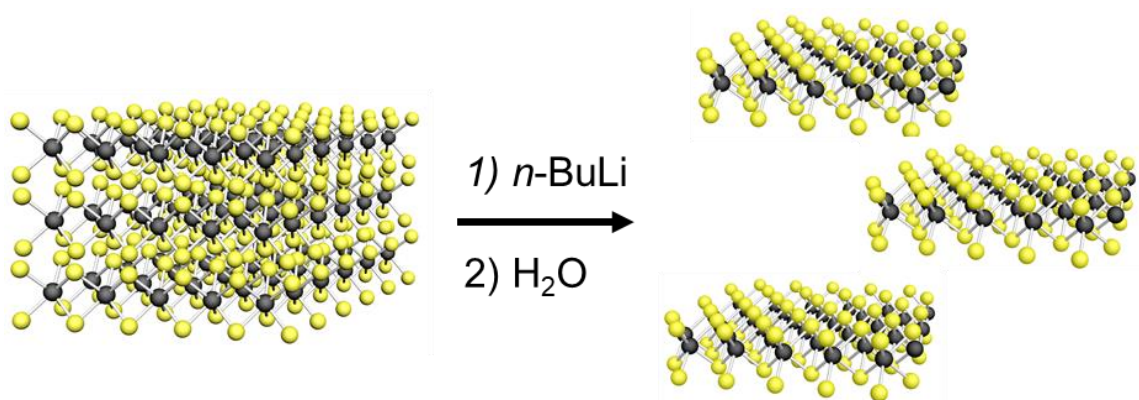


**Figure 1.3.** Illustration of chemical exfoliation of TMDC *via* lithium intercalation chemistry.

Alternatively, chemical exfoliation provides homogeneous suspensions of TMDCs in an array of solvents and in high yield. Lithium intercalation chemistry is used for exfoliation in which bulk TMDC powder is immersed in a solution of a lithium source (typically *n*-butyllithium) and during reaction, lithium ions intercalate the layers of the TMDC in a diffusion-limited process (Figure 1.3). The lithium-intercalated powder is then subjected to sonication in water and the combined effects of cavitation from sonication and the exothermic reaction between lithium and water exfoliates the TMDC into nanosheets accompanied by the evolution of lithium hydroxide, butane and lithium sulfide salts. This reaction is favorable as the basal planes of TMDCs are negatively charged which stabilizes the metal cation once intercalated with the TMDC structure. The chemical exfoliation process affords nanosheets in high yield and induces a phase change in the TMDC going from semiconducting 2H phase to the metallic 1T phase. Due to the highly exothermic nature of the exfoliation process, the nanosheets usually contain a high density of defects in the form of edge and basal plane chalcogen vacancies providing a high surface area catalyst for water splitting producing hydrogen and oxygen gases.<sup>30</sup>



In a more facile process, monolayer to few layer suspensions of TMDCs are prepared by solution-assisted exfoliation.<sup>31</sup> A polar solvent such as dimethylformamide (DMF) or n-methylpyrrolidone (NMP) are introduced to a TMDC powder to form a heterogeneous suspension. Using ultrasonication under ambient conditions, these solvents form hydroperoxides that generate negative charges on the basal plane of the TMDC and, with a combination of electrostatic repulsion and cavitation, yield exfoliated sheets. Unlike chemical exfoliation, solution exfoliation gives TMDC nanosheets that have fewer defects which do not undergo a phase change to the metallic 1T state and produce semiconducting 2H TMDCs useful for semiconducting inks or polymer composites.

### **1.1.2: Electronic Behavior of TMDCs**

TMDCs have been implemented as materials to improve tribological performance of lubricants and polymer composites for more than 30 years. They have only recently found utility as high-performance semiconductors and prospective candidates for quantum electronics. Radisavljevic and coworkers described the first electronic application of TMDC semiconductors by fabricating field-effect transistors from mechanically exfoliated MoS<sub>2</sub>.<sup>32</sup> These transistors displayed remarkably high electron mobilities ( $\sim 200 \text{ cm}^2/\text{V}\cdot\text{s}$ ) and on/off current ratios ( $I_{\text{on/off}} \sim 10^8$ ) outperforming the best FETs using single crystal organic semiconductors ( $1\text{-}10 \text{ cm}^2/\text{V}\cdot\text{s}$ ) and approach the performance metrics of silicon-based transistors ( $\sim 500 \text{ cm}^2/\text{V}\cdot\text{s}$ ). Soon after, a myriad of examples emerged demonstrating the high performance of single layer MoS<sub>2</sub> as well as other TMDCs, elucidating the intrinsic properties of TMDCs with different compositions. While MoS<sub>2</sub> is intrinsically an n-type semiconductor (*i.e.*, conducts negative charge), TMDCs such as tungsten diselenide (WSe<sub>2</sub>) is p-type<sup>33</sup> (*i.e.*, conducts positive charge) and others such as black phosphorus

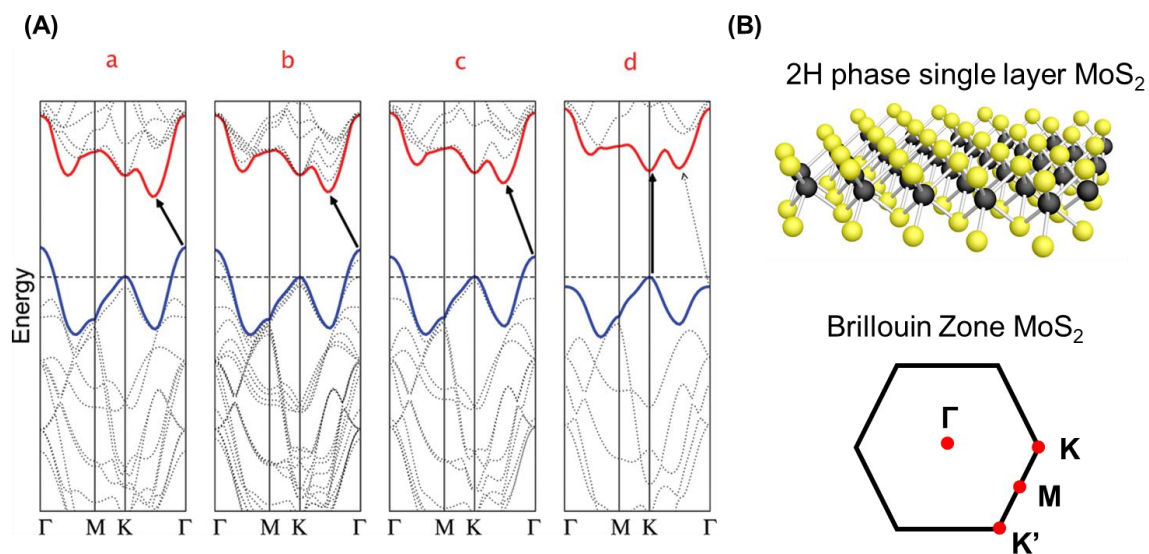


**Figure 1.4.** (A) Energy band diagram showing the evolution of the band gap of MoS<sub>2</sub> moving from an indirect gap of 1.2 eV at bulk thicknesses (a) to a direct gap of 1.8 eV at monolayer thickness (d). (B) Depiction of the real space lattice of MoS<sub>2</sub> and the first Brillouin zone highlighting the symmetry points in momentum space ( $\Gamma$ , M, and K) Figure 1.4a was reprinted with permission from Nano Letters, ref. 43, copyright 2010 American Chemical Society.

(BP) display ambipolar (*i.e.*, conducts both positive and negative charges) charge conduction characteristics.<sup>34</sup>

Along with advantageous conduction behavior, TMDCs show a layer-dependent band structure.<sup>35</sup> The origin of such thickness behavior stems largely from interlayer interactions, with band energies influenced by the position of atomic orbitals and their environment. For example, MoS<sub>2</sub> displays an indirect bandgap of  $\sim 1.2$  eV at multilayer ( $\geq 10$  layers) thicknesses and a direct gap of  $\sim 1.8$  eV at a single layer.<sup>19</sup> Figure 1.4A shows the evolution of the band structure of MoS<sub>2</sub> as a function of thickness plotted as the band energy vs. location in momentum space.<sup>35</sup> To visualize the band energy locations in relation to points in momentum space both the real space and primitive reciprocal lattice (first Brillouin zone) of MoS<sub>2</sub> is shown in Figure 1.4B. Shown in the multilayer case, the conduction band minimum is centered between the  $\Gamma$  and K points (high symmetry points

in the Brillouin zone) while the valance maximum is located at the  $\Gamma$  point, providing the lowest energy indirect bandgap. The energies at these points in momentum space reflect inter- and intra-molecular orbital interactions with energies at the K point associated with d-orbitals of the transition metal and the energies around the  $\Gamma$  point reflecting energies associated with p-orbitals of the chalcogens.<sup>36</sup> In going from multilayer to single layer MoS<sub>2</sub>, the conduction band minimum shifts nominally to the K point with an accompanying larger shift of the valance band maximum to the K point, now signifying a direct gap semiconductor at monolayer thickness and larger bandgap of  $\sim 1.8$  eV. This indirect to direct gap transition is physically manifested as photoluminescence, with almost no photoluminescence intensity showing at bulk thicknesses and relatively high

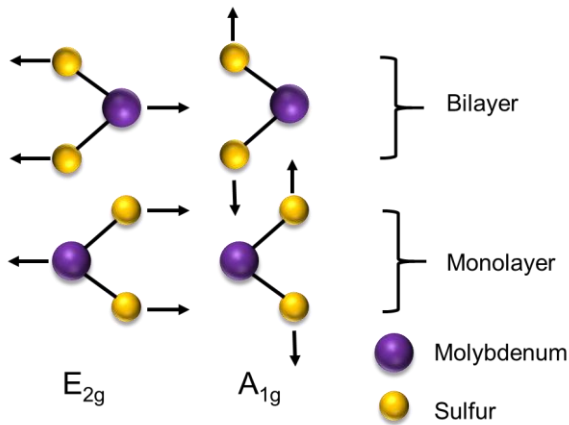
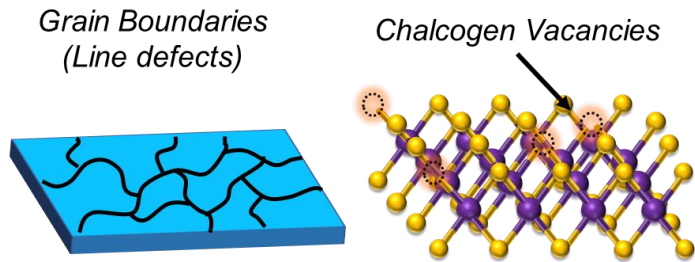


**Figure 1.5.** Diagram of the active Raman signatures ( $E_{2g}$  and  $A_{1g}$ ) stemming from in-plane and out-of-plane vibrations.

photoluminescence taking place at few to monolayer thickness.<sup>37</sup> In the photoluminescence spectrum of MoS<sub>2</sub>, the direct gap transition appears at 670 nm and a shoulder at roughly 630 nm with the two excitonic bands observed due to the spin-orbit coupling of electrons which appears as a splitting of the valance band.

Similarly, the Raman spectra of TMDCs are highly influenced by layer number; for MoS<sub>2</sub>, there exist four Raman modes ( $E_{1g}$ ,  $E_{2g}^1$ ,  $A_{1g}$ ,  $E_{2g}^2$ ) with the  $E_{2g}^1$  (in-plane vibration) and  $A_{1g}$  (out of plane vibration) being the most sensitive to layer effects and surface adsorbates (Figure 1.5).<sup>38</sup> With both PL and Raman spectroscopies, quality, layer number, and effects of adsorbates on TMDC are accessed and their inherent electronic properties can be

**Figure 1.6.** Depiction of the two types of defects found in TMDCs (left) line defects in the form of grain boundaries and (right) point defects in the form of chalcogen vacancies.



observed due to their layer-dependent behavior. Contributions to both the electronics and optical properties of TMDCs is not limited to layer thickness, but significant effort has been put forth to understand the role of structure at a single layer by exploring defects and their influence on the macroscopic behavior of TMDCs.

### 1.1.3: Defect and Interfacial Engineering

Defects in TMDCs primarily occur in the form of line defects (grain boundaries),<sup>39</sup> point defects, and edges established as chalcogen vacancies at the edge and basal plane (Figure 1.6).<sup>2</sup> Defects are created inherently during the growth process or during exfoliation and give rise to local band structure fluctuations centered at the defect site.<sup>40</sup> Using density functional theory (DFT) calculations, Wang and coworkers showed that sulfur vacancies in  $WS_2$  give rise to donor states near the valance band and middle of the bandgap with the defect state near the valance band representing contributions from unsaturated tungsten d-orbitals.<sup>41</sup> This concentrates electron density near the vacancy site and leads to electron donation from the unsaturated tungsten atoms resulting in n-doping of the TMDC. Further work has shown the opposite effect with  $WSe_2$  where selenium vacancies ultimately result in p-doping, significantly altering the local electronics.<sup>42</sup> Defects are also responsible for charge trapping and impurity scattering which have deleterious effects on charge mobility in FETs.<sup>2</sup> These trap states are typically located near

the band edges and in a device context, the localization of trap states at TMDC band edges cause Fermi-level pinning at the interface between a metal electrode and TMDC.<sup>19</sup>

Defects also influence the phase behavior of TMDCs depending on the density and composition of the material.<sup>2</sup> For example, the metallic 1T phase of MoS<sub>2</sub> and MoSe<sub>2</sub> have been produced by reaction with lithium or laser irradiation.<sup>23,22</sup> These methods react or ionize basal plane chalcogens and yield vacancy defects that cause a change in the local geometry of the TMDC to accommodate the lost chalcogen. Spatial control over the phase of TMDCs can be advantageous for devices to create contact layers with a reduced Schottky barrier using metallic TMDCs. Yang and coworkers used laser irradiation to pattern 1T MoSe<sub>2</sub> homojunctions, with the 1T phase acting as the contact layer between the semiconducting 2H phase and metal contact.<sup>23</sup> Using the 1T phase contact layer, MoSe<sub>2</sub> FETs showed an increase in conductivity and electron mobility, with the room temperature mobility increasing by two orders of magnitude compared to MoSe<sub>2</sub> transistors using only the 2H phase. While defects can be used to advantage in contact layers, the active layer or channel must retain a pristine quality to increase electronic performance. Therefore, methods to passivate defects remove impurity scattering sites have been developed and used to further modulate the inherent electronic behavior of TMDCs.

#### **1.1.4: Doping of Semiconducting TMDCs**

The implementation of TMDCs in devices requires relatively pure materials with a low density of defects or impurities as they significantly alter the electronic behavior of the semiconductors. For the fabrication of more sophisticated device architectures, such as p-n junctions, precise spatial control over electronics along the axis of the TMDC is needed. Methods to both passivate defects and alter the electronics of TMDCs have been introduced

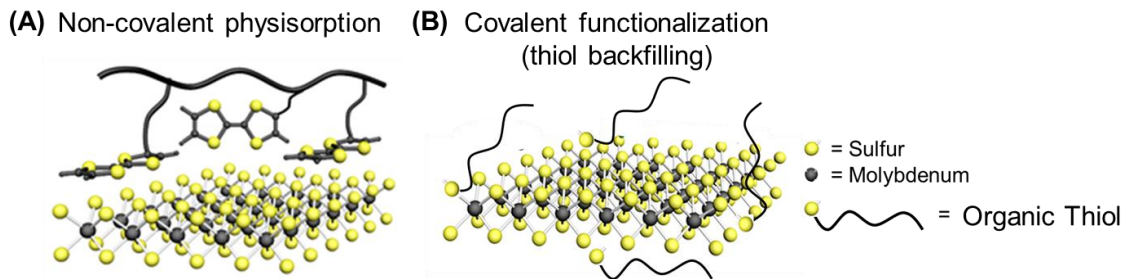


**Figure 1.7.** (A) Cartoon showing non-covalent functionalization of TMDC through physisorption of organic molecules and polymers. (B) Covalent functionalization of TMDCs by backfilling chalcogen vacancies with organic thiols.

to overcome these challenges. These methods include substitutional backfilling or doping,<sup>43</sup> ion beam implantation,<sup>44</sup> alloying,<sup>45</sup> and covalent<sup>46</sup> or non-covalent<sup>47</sup> backfilling with organic dopants. Methods like ion implantation with phosphorus or transition metals have enabled complete inversion of MoS<sub>2</sub> electronics, from n-type to p-type conduction and represent a scalable method to fabricate TMDC junction devices. Introducing selenium vapor during the growth of WS<sub>2</sub> allowed for systematic incorporations of selenium into WS<sub>x</sub>Se<sub>y</sub> alloys that effectively altered the optoelectronic behavior as a function of selenium concentration in the alloy.<sup>48</sup> While these methods (*i.e.*, substitutional doping, ion beam implantation, and alloying) afford TMDCs with fewer defects and enhanced electronic qualities, they require high vacuum techniques that irreversibly alter the structure or composition. Alternatively, modification with organic small molecules or polymers both passivate defects and, depending on the accompanying functionality, dope the TMDC while being reversible and patternable through common lithographic techniques. There are two primary methods to functionalize and/or dope TMDCs: covalent modification using organic thiols to backfill sulfur vacancies (Figure 1.7A) and non-covalent doping entailing the physisorption of organic molecules to the basal plane of TMDCs enabling redistribution of charges at the TMDC/dopant interface (Figure 1.7B). Jung and coworkers showed that

immersing single layer MoS<sub>2</sub> in a solution of either mercaptoethylamine or perfluorodecanethiol resulted in n- or p-doping respectively by monitoring shifts in the PL spectra or carrier density curves gathered from FETs.<sup>49</sup> Furthermore, Huang and Dravid showed that using thiol terminated oligoethylene glycol with charged end groups leads to stable homogeneous suspensions of MoS<sub>2</sub> nanosheets and were used for selective complexation of biomolecules *via* electrostatic interactions.<sup>50</sup> Thiol backfilling is an expedient path to altered TMDCs but suffers from irreversibility and lacks spatial control over carrier concentration needed for advanced TMDC electronics. Alternatively, non-covalent doping with small molecules and polymers such as benzyl viologen,<sup>51</sup> polyethyleneimine (PEI),<sup>52</sup> and poly[[4,8-bis[(2-ethylhexyl)oxy]benzo[1,2-b:4,5-b']dithiophene-2,6-diyl][3-fluoro-2-[(2-ethylhexyl)carbonyl]thieno[3,4-b]thiophenediyl]] (PTB7) have resulted in n- or p-doped TMDCs with broader composite absorption and emission behavior and reduced contact resistance in FETs.<sup>53</sup>

## 1.2: Thesis Outline

While numerous examples of doping TMDCs exist, reports on p-doping TMDCs are relatively scarce and demonstrations of all-in-one polymer/TMDC systems that can simultaneously modify the work function and solution behavior are lacking. Therefore, using functional polymer scaffolds *this dissertation examines the modification of 2D materials to alter the inherent electronic and solution properties and highlights the utility of such methods in both solution and device contexts.*

Chapter 2 describes the synthesis of polymers incorporating tetrathiafulvalene (TTF) to both n-dope and stabilize suspensions of MoS<sub>2</sub> nanosheets (Chemical Science, 2016).<sup>54</sup> Two polymerization methodologies were used to afford TTF-containing polymers: ring-

opening metathesis polymerization (ROMP) and post-polymerization ‘click’ chemistry on polymers synthesized by RAFT polymerization. ROMP of a TTF-functionalized norbornene monomer showed rapid conversion to high molecular weight polymer with narrow dispersity as a result of the living behavior of the polymerization at low reaction times. RAFT copolymerization of methyl methacrylate with 2-chloroethyl methacrylate afforded high molecular weight polymers with narrow molecular weight distributions. The chloride is easily substituted by an azide functionality and concurrent azide-alkyne cycloaddition with TTF-alkyne afforded polymers bearing TTF. In both cases, the content of TTF was dictated by the feed ratio of the monomers (TTF norbornene and 2-chloroethyl methacrylate) and gave polymers soluble in a wide range of organic solvents. Dispersing MoS<sub>2</sub> nanosheets in a solution of TTF polymers resulted in extended colloidal stability with polymers having 30 mol% or more of TTF showing months of shelf stability while polymers without TTF reaggregated within days. KPFM of mechanically exfoliated MoS<sub>2</sub> showed an increase in the surface potential contrast, representing a decrease in the overall work function of the TMDC. This effect results from the redox behavior of TTF which oxidizes in the presence of MoS<sub>2</sub> thereby donating electrons to the semiconducting nanosheets. Chapter 2 continues by examination of the redox behavior of TTF polymers in film and solution by cyclic voltammetry and spectroelectrochemistry which reveal that several TTF species (radical cation, radical cation dimers and dications) are responsible for the ground state charge transfer to MoS<sub>2</sub>.

Chapter 3 builds upon findings from Chapter 2 utilizing a sulfur-rich electron acceptor bithiazolidinylidene (BT) (Chemical Science, 2018).<sup>55</sup> Novel BT monomers were synthesized and used to fabricate polymers by polycondensation of BT-diol with



hexamethylene diisocyanate to form BT-functionalized polyurethanes. These polymers exhibit typical step-growth polymerization characteristics (*i.e.*, high molecular weight at high conversions, and molecular weight distributions approaching 2.0) and BT incorporations match that of the initial feed ratio of monomers. The thermal and solution stability of the resulting polymers was examined using UV-Vis, PL, and NMR spectroscopies and proposed chemical transformations are discussed. KPFM experiments on CVD grown monolayer MoS<sub>2</sub> revealed a work function increase by 0.22 eV for polymers with 50 mol% of BT, signifying scarcely reported p-doping of MoS<sub>2</sub>.

Chapter 4 uses small molecules TTF and BT on monolayer CVD grown MoS<sub>2</sub> to demonstrate bidirectional tuning of MoS<sub>2</sub> work function (Journal of Physical Chemistry C, 2019).<sup>56</sup> With all other parameters the same (*i.e.*, TMDC growth method, solvent, temperature, and flake thickness), we investigated the role of the substrate in the doping efficacy of TTF and BT on MoS<sub>2</sub>. Through concurrent KPFM experiments, the work function of MoS<sub>2</sub> was measured before and after coating with a dopant solution and experiments were performed with MoS<sub>2</sub> grown on either Si/SiO<sub>2</sub> or Al<sub>2</sub>O<sub>3</sub>. For TTF doping a 0.25 eV decrease in work function was observed using MoS<sub>2</sub> on Si/SiO<sub>2</sub>, confirming our previous experiments. However, when doping MoS<sub>2</sub> with TTF on Al<sub>2</sub>O<sub>3</sub>, a consistent 1.23 eV decrease in the work function was observed, approaching the theoretical limit calculated by density functional theory. Moreover, BT doping yielded a 0.20 eV increase in work function with MoS<sub>2</sub> on Si/SiO<sub>2</sub>, but a significant increase in the work function of 0.82 eV was observed using MoS<sub>2</sub> on Al<sub>2</sub>O<sub>3</sub>. We rationalize the increase in doping efficacy as an effect of polarized static charge at the semiconductor/dielectric interface. A high dielectric incurring a larger polarization of charges at the substrate leading to a measured work

function that is effectively less screened and more representative of the true magnitude of doping.

Finally, Chapter 5 switches the focus from doping TMDCs to graphene utilizing zwitterionic polymers as functional photoresists (ACS Nano, 2018)<sup>57</sup>. Polymer zwitterions were synthesized by conventional free radical copolymerization of sulfobetaine methacrylate and methyl methacrylate and afforded materials with high molecular weights and monomodal molecular weight distributions approaching a dispersity of 2.0. Electron beam lithography on 70 nm films of PSBMA-co-PMMA effectively degraded polymer that was exposed to the high energy beam and patterns were obtained with resolutions approaching that of conventional methacrylate-based photoresists, confirmed by atomic force microscopy (AFM). The presence of the zwitterion allowed for the use of a range of polar solvents to be used for development and could even be extended to salt water solutions. FETs were fabricated on CVD grown graphene and PSBMA-co-PMMA was deposited, exposed, and developed on top of the devices such that three types of devices were produced: bare graphene, graphene fully coated with PSBMA-co-PMMA, and graphene that is only half-coated with PSBMA-co-PMMA. Current *vs.* voltage characteristics of the three devices showed a large shift in the charge neutrality point of graphene, representing n-doping on the polymer coated portion of the device. Interestingly, the half-coated device exhibited rectifying characteristics and high currents at positive and negative gate voltages signifying p-n junction behavior. Thus, a robust and solution processible functional photoresist was demonstrated marking a large leap in photoresist technology and greatly expediting the process of TMDC p-n junction fabrication.

### 1.3 References

1. Xia, F., Farmer, D. B., Lin, Y. M. & Avouris, P. Graphene field-effect transistors with high on/off current ratio and large transport band gap at room temperature. *Nano Lett.* **10**, 715–718 (2010).
2. Zou, X. & Yakobson, B. I. An open canvas - 2D materials with defects, disorder, and functionality. *Acc. Chem. Res.* **48**, 73–80 (2015).
3. Choi, J., Zhang, H. & Choi, J. H. Modulating optoelectronic properties of two-dimensional transition metal dichalcogenide semiconductors by photoinduced charge transfer. *ACS Nano* **10**, 1671–1680 (2016).
4. Cheng, R. *et al.* Electroluminescence and Photocurrent Generation from Atomically Sharp WSe<sub>2</sub>/MoS<sub>2</sub> Heterojunction *p-n* Diodes. *Nano Lett.* **14**, 5590–5597 (2014).
5. Park, I. J. *et al.* Stretchable thin-film transistors with molybdenum disulfide channels and graphene electrodes. *Nanoscale* **10**, 16069–16078 (2018).
6. Elder, R. M., Neupane, M. R. & Chantawansri, T. L. Stacking order dependent mechanical properties of graphene/MoS<sub>2</sub> bilayer and trilayer heterostructures. *Appl. Phys. Lett.* **107**, (2015).
7. Novoselov, K. S. *et al.* Electric Field Effect in Atomically Thin Carbon Films. *Science (80)*. **306**, 666–669 (2004).
8. Kim, B. J. *et al.* High-performance flexible graphene field effect transistors with ion gel gate dielectrics. *Nano Lett.* **10**, 3464–3466 (2010).
9. Gu, T. *et al.* Regenerative oscillation and four-wave mixing in graphene optoelectronics. *Nat. Photonics* **6**, 554–559 (2012).
10. Chung, C. *et al.* Biomedical applications of graphene and graphene oxide. *Acc. Chem. Res.* **46**, 2211–2224 (2013).
11. Ishihara, S. *et al.* Metallic versus Semiconducting SWCNT Chemiresistors: A Case for Separated SWCNTs Wrapped by a Metallosupramolecular Polymer. *ACS Appl. Mater. Interfaces* **9**, 38062–38067 (2017).
12. Kim, Hyunwoo; Abdala, Ahmed; Macosco, C. Graphene/Polymer Nanocomposites. *Macromolecules* **43**, 6515–6530 (2010).
13. Ballesteros-Garrido, R., Rodriguez, R., Álvaro, M. & Garcia, H. Photochemistry of covalently functionalized graphene oxide with phenothiazinyl units. *Carbon N. Y.* **74**, 113–119 (2014).

14. Roy, T. *et al.* Dual-Gated MoS<sub>2</sub>/WSe<sub>2</sub> van der Waals Tunnel Diodes and Transistors. *ACS Nano* **9**, 2071–2079 (2015).
15. Ren, X. *et al.* A Se-doped MoS<sub>2</sub> nanosheet for improved hydrogen evolution reaction. *Chem. Commun.* **51**, 15997–16000 (2015).
16. Rapoport, L. *et al.* Tribological properties of WS<sub>2</sub> nanoparticles under mixed lubrication. *Wear* **255**, 785–793 (2003).
17. Rosentsveig, R. *et al.* Fullerene-like MoS<sub>2</sub> nanoparticles and their tribological behavior. *Tribol. Lett.* **36**, 175–182 (2009).
18. Rigato, V. *et al.* Properties of sputter-deposited MoS<sub>2</sub>/metal composite coatings deposited by closed field unbalanced magnetron sputter ion plating. *Surf. Coatings Technol.* **131**, 206–210 (2000).
19. Ganatra, R. & Zhang, Q. Few-layer MoS<sub>2</sub>: A promising layered semiconductor. *ACS Nano* **8**, 4074–4099 (2014).
20. Li, X. *et al.* One-step hydrothermal synthesis of high-percentage 1T-phase MoS<sub>2</sub> quantum dots for remarkably enhanced visible-light-driven photocatalytic H<sub>2</sub> evolution. *Appl. Catal. B Environ.* **243**, 76–85 (2019).
21. Tan, S. J. R. *et al.* Temperature- and Phase-Dependent Phonon Renormalization in 1T'-MoS<sub>2</sub>. *ACS Nano* **12**, 5051–5058 (2018).
22. Yu, Y. *et al.* High phase-purity 1T'-MoS<sub>2</sub>- and 1T'-MoSe<sub>2</sub>-layered crystals. *Nat. Chem.* **10**, 638–643 (2018).
23. Koppera, R. *et al.* Phase-engineered low-resistance contacts for ultrathin MoS<sub>2</sub> transistors. *Nat. Mater.* **13**, 1128–1134 (2014).
24. Wu, S. *et al.* Vapor-Solid Growth of High Optical Near-Unity Valley Polarization Quality MoS<sub>2</sub> Monolayers with. *ACS Nano* **7**, 2768–2772 (2013).
25. El Kazzi, S. *et al.* MoS<sub>2</sub> synthesis by gas source MBE for transition metal dichalcogenides integration on large scale substrates. *J. Appl. Phys.* **123**, 1–6 (2018).
26. Hu, Z. *et al.* Two-dimensional transition metal dichalcogenides: Interface and defect engineering. *Chem. Soc. Rev.* **47**, 3100–3128 (2018).
27. Bhimanapati, G. R. *et al.* Recent advances in two-dimensional materials beyond graphene. *ACS Nano* **9**, 11509–11539 (2015).
28. Yoon, Y., Ganapathi, K. & Salahuddin, S. How good can monolayer MoS<sub>2</sub> transistors be? *Nano Lett.* **11**, 3768–3773 (2011).

29. Eda, G. *et al.* Photoluminescence from Chemically Exfoliated MoS<sub>2</sub>. 5111–5116 (2011). doi:10.1021/nl201874w
30. Li, Y. *et al.* MoS<sub>2</sub> nanoparticles grown on graphene: An advanced catalyst for the hydrogen evolution reaction. *J. Am. Chem. Soc.* **133**, 7296–7299 (2011).
31. Coleman, J. N. *et al.* Two-Dimensional Nanosheets Produced by Liquid Exfoliation of Layered Materials. *Science (80-. )*. **331**, 568–572 (2011).
32. Radisavljevic, B., Radenovic, A., Brivio, J., Giacometti, V. & Kis, A. Single-layer MoS<sub>2</sub> transistors. *Nat. Nanotechnol.* **6**, 147–150 (2011).
33. Kang, D. *et al.* Controllable Nondegenerate p-Type Doping of Tungsten Diselenide by Octadecyltrichlorosilane. *ACS Nano* **9**, 1099–1107 (2015).
34. Yue, D. *et al.* Passivated ambipolar black phosphorus transistors. *Nanoscale* **8**, 12773–12779 (2016).
35. Venkata Subbaiah, Y. P., Saji, K. J. & Tiwari, A. Atomically Thin MoS<sub>2</sub>: A Versatile Nongraphene 2D Material. *Adv. Funct. Mater.* **26**, 2046–2069 (2016).
36. Cao, T. *et al.* Valley-selective circular dichroism of monolayer molybdenum disulphide. *Nat. Commun.* **3**, (2012).
37. Splendiani, A. *et al.* Emerging photoluminescence in monolayer MoS<sub>2</sub>. *Nano Lett.* **10**, 1271–1275 (2010).
38. Lee, C. *et al.* Anomalous Lattice Vibrations of Single- and Few-Layer MoS<sub>2</sub>. *ACS Nano* **4**, 2695–2700 (2010).
39. Ly, T. H. *et al.* Observing grain boundaries in CVD-grown monolayer transition metal dichalcogenides. *ACS Nano* **8**, 11401–11408 (2014).
40. Yore, A. E. *et al.* Visualization of Defect-Induced Excitonic Properties of the Edges and Grain Boundaries in Synthesized Monolayer Molybdenum Disulfide. *J. Phys. Chem. C* **120**, 24080–24087 (2016).
41. Carozo, V. *et al.* Optical identification of sulfur vacancies: Bound excitons at the edges of monolayer tungsten disulfide. *Sci. Adv.* **3**, 1–9 (2017).
42. Stanford, M. G. *et al.* High Conduction Hopping Behavior Induced in Transition Metal Dichalcogenides by Percolating Defect Networks: Toward Atomically Thin Circuits. *Adv. Funct. Mater.* **27**, 1–9 (2017).
43. Kim, E. *et al.* Site Selective Doping of Ultrathin Metal Dichalcogenides by Laser-Assisted Reaction. *Adv. Mater.* **28**, 341–346 (2016).

44. Bangert, U. *et al.* Ion-beam modification of 2-D materials - single implant atom analysis via annular dark-field electron microscopy. *Ultramicroscopy* **176**, 31–36 (2017).
45. Feng, Q. *et al.* Growth of MoS<sub>2</sub>(1- x)Se<sub>2</sub>(x = 0.41-1.00) Monolayer Alloys with Controlled Morphology by Physical Vapor Deposition. *ACS Nano* **9**, 7450–7455 (2015).
46. Liu, T. *et al.* Drug delivery with PEGylated MoS<sub>2</sub> nano-sheets for combined photothermal and chemotherapy of cancer. *Adv. Mater.* **26**, 3433–3440 (2014).
47. Hsu, C.-L. *et al.* Layer-by-Layer Graphene/TCNQ Stacked Films as Conducting Anodes for Organic Solar Cells. *ACS Nano* **6**, 5031–5039 (2012).
48. Duan, X. *et al.* Synthesis of WS<sub>2</sub>xSe<sub>2-2x</sub>Alloy Nanosheets with Composition-Tunable Electronic Properties. *Nano Lett.* **16**, 264–269 (2016).
49. Sim, D. M. *et al.* Controlled Doping of Vacancy-Containing Few-Layer MoS<sub>2</sub> via Highly Stable Thiol-Based Molecular Chemisorption. *ACS Nano* **9**, 12115–12123 (2015).
50. Chou, S. *et al.* Ligand Conjugation of Chemically Exfoliated MoS<sub>2</sub>. *J. Am. Chem. Soc.* **135**, 4584–4587 (2013).
51. Kiriya, D., Tosun, M., Zhao, P., Kang, J. S. & Javey, A. Air-stable surface charge transfer doping of MoS<sub>2</sub> by benzyl viologen. *J. Am. Chem. Soc.* **136**, 7853–7856 (2014).
52. Du, Y., Liu, H., Neal, A. T., Si, M. & Ye, P. D. Molecular Doping of Multilayer MoS<sub>2</sub> Field-Effect Transistors: Reduction in Sheet and Contact Resistances. *IEEE Electron Device Lett.* **34**, 1328–1330 (2013).
53. Shastry, T. A. *et al.* Mutual Photoluminescence Quenching and Photovoltaic Effect in Large-Area Single-Layer MoS<sub>2</sub>-Polymer Heterojunctions. *ACS Nano* (2016). doi:10.1021/acsnano.6b06592
54. Selhorst, R. C. *et al.* Tetrathiafulvalene-containing polymers for simultaneous non-covalent modification and electronic modulation of MoS<sub>2</sub> nanomaterials. *Chem. Sci.* **7**, 4698–4705 (2016).
55. Selhorst, R., Wang, P., Barnes, M. & Emrick, T. Bithiazolidinylidene polymers: Synthesis and electronic interactions with transition metal dichalcogenides. *Chem. Sci.* **9**, 5047–5051 (2018).
56. Selhorst, R., Wang, Ramasubramaniam, A., Emrick, T., Barnes, M.D. Bidirectional Electronic Tuning of Single-Layer MoS<sub>2</sub> with Conjugated Organochalcogens. *J. Phys. Chem. C.* **123**, 1506-1511 (2019).

57. Alon, H. *et al.* Lithographically Patterned Functional Polymer-Graphene Hybrids for Nanoscale Electronics. *ACS Nano* **12**, 1928–1933 (2018).

## CHAPTER 2

# TETRATHIAFULVALENE-CONTAINING POLYMERS FOR THE MODIFICATION OF MoS<sub>2</sub>

### 2.1 Introduction

Future integration of 2D materials into electronic materials requires modulating its processibility and electronic properties through surface functionalization. The ability to process 2D nanomaterials from conventional solvents would advance applications in sensing, electroactive inks, and would ease the device fabrication process.<sup>1</sup> For graphene, numerous examples of covalent and non-covalent modification exist and more work is needed to extend these material preparations to TMDCs.<sup>2-4</sup> There are examples of TMDC functionalization using primarily covalent functionalization of the edge and basal plane of TMDCs. For example, Ding *et al.* described the functionalization of 2H phase MoS<sub>2</sub> nanosheets with functional thiols enabling modulation of the optoelectronic behavior of the pristine nanosheets.<sup>5</sup> This method involves the insertion of thiols at the Mo-rich TMDC edges and surface defects (S vacancies). Conversely, non-covalent approaches to MoS<sub>2</sub> (basal plane) functionalization are lacking, and the expansion of such methods would preserve the structure of the nanoparticles, conceptually in parallel to pyrene or tetracyanoquinonodimethane modification of graphene and carbon nanotubes.<sup>6,7</sup> Additionally non-covalent modification,<sup>8</sup> which can be desirable since tailored semiconductor electronics have utility in sensing, catalysis and spintronics/valleytronics that requires dopants (*i.e.*, inorganic ions, tertiary amines, ionic



liquids and small molecule electron donors).<sup>9-12</sup> Despite recent progress, the need remains for simple routes to novel TMDC dopants that afford solution processible and robust TMDC-based hybrid architectures.

The work of Chapter 2 describes the preparation of TTF-substituted polymers to solubilize MoS<sub>2</sub> nanosheets and alter the inherent electronic structure of pristine MoS<sub>2</sub>. TTF is a sulfur-rich electron donor that forms stable charge transfer salts with acceptors, with oxidation potentials at 0.37 and 0.70 V (*vs.* Ag/AgCl Standard Reference Electrode), offering n-doping when in contact with 2D materials.<sup>13</sup> The sulfur and electron-rich structure of TTF is prime for inducing non-covalent interactions with MoS<sub>2</sub>, including S-S, S-Mo, and S- $\pi$  coordination, with these interactions envisaged to facilitate charge transfer at the TTF/MoS<sub>2</sub> interface.<sup>13,14</sup> It is anticipated that polymers featuring pendent TTF moieties will function in multi-point basal plane coordinative interactions with MoS<sub>2</sub>. However, the preparation of such polymers is synthetically challenging due to reactivity of TTF itself for free radical and ionic polymerization techniques, affording low yields and ill-characterized products.<sup>15-17</sup>

The synthetic approaches to TTF-containing polymers shown in this chapter alleviate the common difficulties encountered with free-radical polymerization. Furthermore, the polymerization methods afford polymers with a tunable content of TTF and polymer backbones that enable nanomaterial dispersions in a range of organic solvents. Two polymerization methods are presented, one in which a TTF-substituted polynorbornene was prepared by ROMP and a second consisting of TTF-substituted

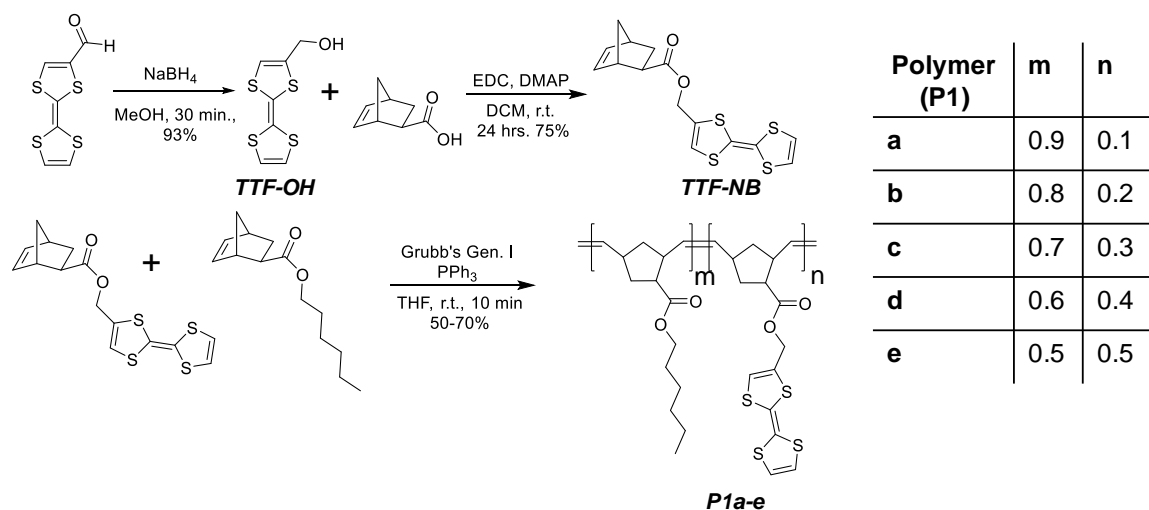


**Figure 2.1.** Synthesis of TTF-containing polymers by ROMP copolymerization of TTF-NB and hexyl-NB.

methacrylate polymers prepared by RAFT polymerization and post-polymerization cycloaddition. These polymers are endowed with redox behavior dictated by TTF-density and comonomer selection, and yield solution stability to chemically exfoliated MoS<sub>2</sub> nanosheets. The experiments are complemented with an insight from DFT calculations that probe MoS<sub>2</sub> surface interactions and their impact on electronic properties.

## 2.2: Synthesis of TTF-Containing Polymers

Figure 2.1 shows the synthesis of TTF-NB prepared first by sodium borohydride reduction of commercially available 2-formyl TTF followed by carbodiimide coupling of 2-hydroxymethyl TTF (TTF-OH) with exo-5-norbornene carboxylate. Attempted ROMP of monomer TTF-NB using Grubb's generation III ruthenium benzylidene catalyst produced insoluble material nearly instantaneously.<sup>18</sup> However, copolymerization of TTF-NB with n-hexyl-substituted norbornene (hexyl-NB) gave soluble polymers with broad, multi-modal molecular weight distributions shown from the gel permeation

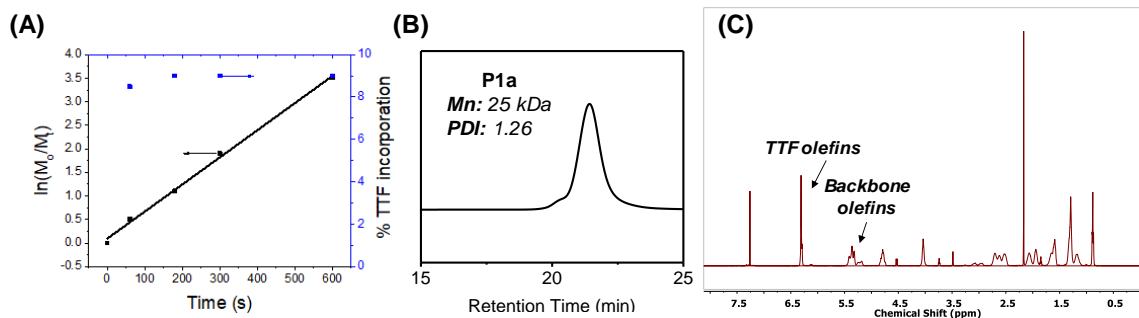


**Figure 2.2.** (A) Kinetics of ROMP copolymerization showing linear monomer consumption with time and low PDIs, indicative of controlled polymerization. (B) Gel permeation chromatograph of polymer **P1a** displaying a monomodal molecular weight distribution. (C)  $^1\text{H}$  NMR spectroscopy of polymer **P1e** showing the TTF and norbornene backbone olefin resonances.

chromatography (GPC) chromatograms. The multimodal distribution may have been incurred from sulfur-metal interactions that interrupt olefin metathesis that is known for other sulfur-containing cyclic olefins.<sup>19</sup> However, polymerizations using Grubbs ‘Generation I catalyst produced polymers with monomodal distributions indicating a suppression of side reactions or cross metathesis. Triphenylphosphine ( $\text{PPh}_3$ ) resulted in controlled, and living, polymerization with linear polymerization kinetics and polymers that possessed low molecular weight distributions (Figure 2.2A). The use of  $\text{PPh}_3$  as an auxiliary ligand for ROMP has been demonstrated by Grubbs with the added ligand intended to increase the relative rates of initiation and propagation  $k_i/k_p$  and, in the current case, suppress catalyst/TTF interactions.<sup>20</sup> Copolymerization of TTF-NB with hexyl-TTF proceeded smoothly, affording poly(TTF-norbornene)s **P1a-e** with estimated molecular weights in the 20-60 kDa range and PDI values of 1.1-1.3 (Figure 2.2B). The successful incorporation of TTF into the polymers was confirmed by  $^1\text{H}$  NMR spectroscopy, with



**Table 2.1** Summary of polymer characterizations for the TTF methacrylate series

Compound	Target TTF incorporation	Actual TTF incorporation	M <sub>n</sub> (GPC)	PDI	Yield
PolyTTFMMA-1 (P1a)	1%	1%	36 kDa	1.14	63
PolyTTFMMA-10 (P1b)	10%	12%	37 kDa	1.23	66
PolyTTFMMA-25 (P1c)	25%	29%	31 kDa	1.28	79
PolyTTFMMA-50 (P1d)	50%	55%	43 kDa	1.26	60
PolyTTF-b-MMA-35 (P1e)	20%	30%	19 kDa	1.14	57
PolyTTFBMA-10 (P1f)	10%	10%	47 kDa	1.17	51
PolyTTFBMA-25 (P1g)	25%	27%	50 kDa	1.23	75
polyTTFBMA-50 (P1h)	50%	52%	42 kDa	1.27	86

kDa and dispersities (PDI) of 1.1-1.3 in high yield. Azide-to-triazole conversion proceeded smoothly as indicated by <sup>1</sup>H NMR spectroscopy noting the loss of  $\text{CH}_2\text{N}_3$  resonance at  $\delta 3.51$  ppm and appearance of triazole proton at  $\delta 7.75$  ppm. Efficient TTF incorporation was additionally confirmed by the presence of TTF olefin resonances at  $\delta 6.31$  and  $\delta 6.33$  ppm, and the methylene groups of the linker at  $\delta 4.33$  and  $\delta 4.69$  ppm. This polymerization methodology is amenable to the synthesis of block copolymers which were prepared with ~35 mole percent of pendent TTF groups. The characteristics of polymerization are summarized in Table 2.1.

### 2.3: Electrochemistry of TTF compounds

Electrochemical features of these TTF-containing polymers were examined using cyclic voltammetry in 0.1 M  $[\text{Bu}_4\text{N}]^+[\text{PF}_6]^-$  solution in N-methylpyrrolidone (NMP), using a Pt button, Pt wire, and non-aqueous Ag/Ag<sup>+</sup> electrode (calibrated vs. the ferrocene/ferrocenium redox couple) as working, counter, and reference electrodes, respectively. Two reversible one-electron oxidation transitions at 0.21 and 0.53 V were observed for TTF itself (Figure 2.4A), attributed to its low lying HOMO and subsequent

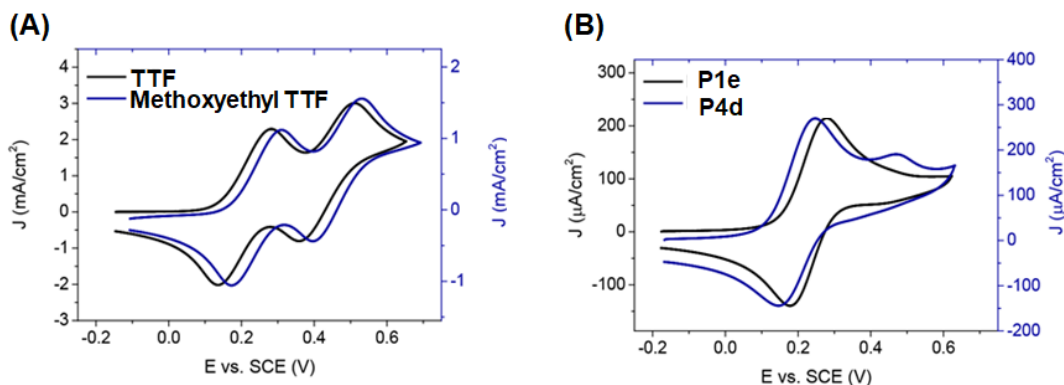


**Figure 2.4.** (A) Cyclic voltammograms of small molecules TTF (black) and a model compound methoxyethyl TTF (blue) showing two reversible oxidation potentials. (B) Cyclic voltammograms of polymers **P1e** (norbornene) and **P4d** (methacrylate) depicting the absence of a second oxidation for the norbornene backbone and suppression of the second oxidation for the methacrylate backbone.

aromatization following electron removal. A TTF model compound (methoxyethyl TTF) exhibited similar redox behavior, with oxidation at 0.24 and 0.55 V showing slightly increased values for oxidation potentials due to the sigma donating behavior of the methyl group. The TTF-substituted polymers displayed different redox properties that hinged on TTF density and backbone selection (Figure 2.4B). Poly(TTF norbornene)s, **P1a-e**, exhibited one reversible oxidation band at  $E_{1/2} = 0.25$  V that did not change based on TTF incorporation. With TTF near the backbone of a polymer, oxidation to the TTF dication would require high local concentrations of the doubly charged species which would destabilize this transition due to the close proximity of the positively charged moieties. Other reactive TTF species are known to occur during oxidation, for example, the TTF radical cation is known to interact with a neutral TTF to afford mixed valence dimers, which then oxidize to dimer dications ( $\pi$ -dimers).<sup>21,22</sup> These  $\pi$ -dimers exist over a wide electrochemical window with initial oxidation occurring at potentials similar to those required for the TTF/TTF<sup>++</sup> redox couple. The absence of a second oxidation peak for the

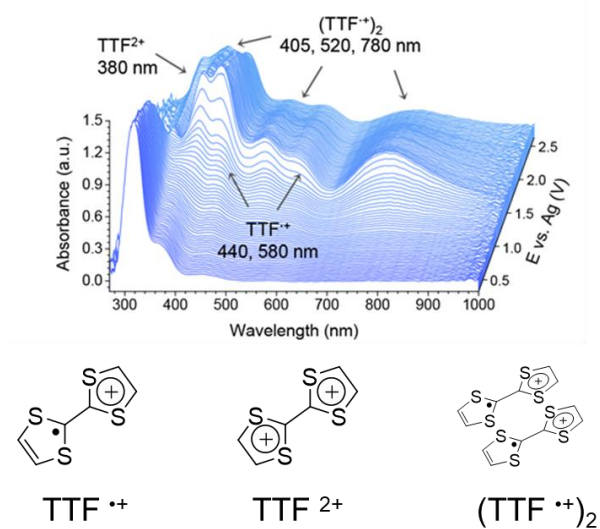


**Figure 2.5.** Spectroelectrochemistry traces of TTF showing the evolution of the UV-Vis spectrum over time. At low potentials, the TTF radical cation and dimer dication absorbances appear and at high potentials the dication species appears.

TTF<sup>2+</sup> and aggregated species. Generally, the TTF-based methacrylate polymers had slightly lower oxidation potentials ( $E_{1/2} = 0.20$  V) than the norbornenes, possibly due to a greater steric accessibility of the redox active sites.

The electrochemically-induced redox species were examined further by *in situ* spectroelectrochemistry in 0.1 M [Bu<sub>4</sub>N]<sup>+</sup>[PF<sub>6</sub>]<sup>-</sup>/acetonitrile solutions. Polymer **P1e** was dropcast on a transparent indium tin oxide (ITO)/glass working electrode, and silver and platinum wires were used as the reference and counter electrodes, respectively. Figure 2.5 show the optical signatures of the oxidized species displaying multiple redox species: the radical cation (440 and 580 nm), dimer dication (405, 520, 780 nm) and dication (380 nm). Notably, minimal temporal separation was observed between the formation of these species, and no evidence for the sole existence of TTF<sup>2+</sup> was found even at high

TTF-NB series could be due to the formation of these dimers, suppressing further oxidation to the dicationic species. For the TTF-containing methacrylates and butyl acrylates **P4a-h**, a second oxidation wave was evident, though attenuated in current density. However, the decrease in peak definition at lower scan rates and quasireversibility of this transition indicates a possible competition between the formation of

electrochemical potentials. This suggest a concerted redox transition and significant destabilization of the second electron oxidation event. While the redox behavior of TTF is complex and dependent on its local environment, all of the TTF-containing polymer systems evaluated oxidize at low electrochemical potential, and thus are suitable for n-doping of TMDC nanosheets.

## 2.4: Solution Behavior of Polymer/MoS<sub>2</sub> suspensions

The ability of TTF-substituted polymers to disperse MoS<sub>2</sub> nanoparticles was probed using chemically exfoliated MoS<sub>2</sub> nanosheets, prepared using *n*-butyl lithium

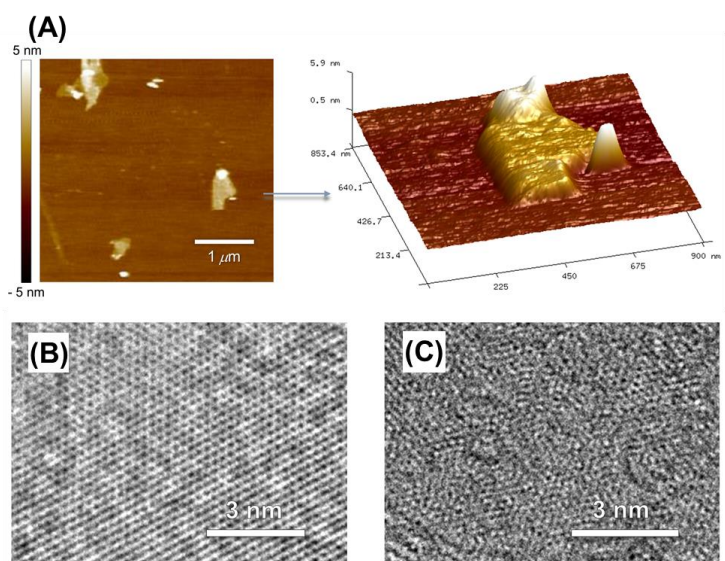


**Figure 2.6.** (A) AFM scan and 3D rendition of MoS<sub>2</sub> nanosheets prepared by liquid exfoliation in NMP. (B) High resolution transmission electron microscopy of MoS<sub>2</sub> nanosheets prepared by liquid exfoliation and (C) chemically exfoliated MoS<sub>2</sub> prepared by lithium intercalation showing distinct differences in the pristine 2H and the defective 1T phases.

(HRTEM, Figure 2.6 B and C). The resulting MoS<sub>2</sub> nanosheets were isolated by centrifuging 1 mL of the 1 mg/mL aqueous suspension (10k rpm for 30 min) followed by

as the intercalating agent.<sup>23</sup>

Atomic force microscopy (AFM) characterization indicated an average thickness of 0.8-1.5 nm, consistent with 1-2 MoS<sub>2</sub> layers (Figure 2.6a).<sup>24,25</sup> The presence of a

disordered 1T lattice in the chemically exfoliated MoS<sub>2</sub> nanosheets was confirmed by high-resolution transmission electron microscopy



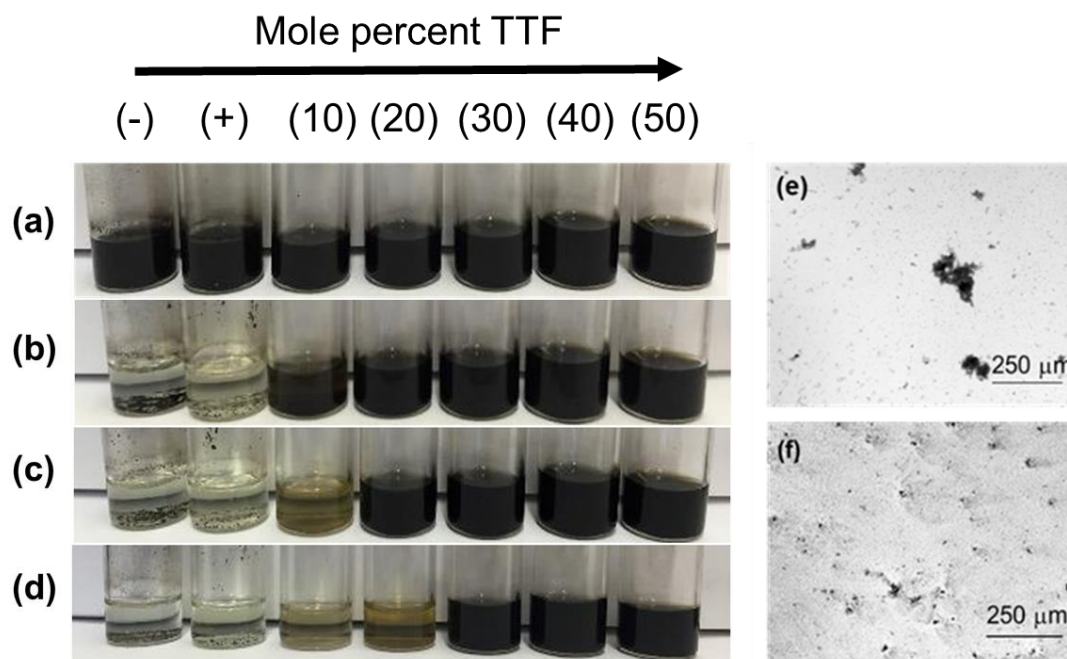


**Figure 2.7.** Photographs of suspensions containing chemically exfoliated MoS<sub>2</sub> nanosheets with polymers **P1a-e** and a negative control (-) containing no polymer and positive control (+) containing poly(norbornene) with no TTF). The photos were taken at different times (A) immediately after redispersion in THF (B) 2 days, (C) 4 days, and (D) 8 days. Optical micrographs showing (E) aggregated nanosheets from control suspensions and (F) dispersed nanosheets from suspensions containing TTF polymers.

redispersion in 1.5 mL THF containing the TTF polymers (1 mg/mL). Control experiments employed 1 mg/mL THF solutions of PMMA, PBMA, and poly(n-hexyl norbornene) to ensure stabilization did not occur simply from the existence of the polymer. Figure 2.7A-D confirm the presence of TTF moieties in the polymers to be crucial for suspension stability. The MoS<sub>2</sub> nanosheets in the control experiments exhibited poor stability, with precipitation occurring within hours representing the aggregation of the nanosheets due to van der Waals interactions. Conversely, TTF polymer-MoS<sub>2</sub> suspensions containing a threshold concentration of TTF in the polymer maintained colloidal stability over several weeks, with greater mole percent TTF inclusion affording greater stability. Optical microscopy confirmed such stability, showing large (hundreds of microns) aggregates for

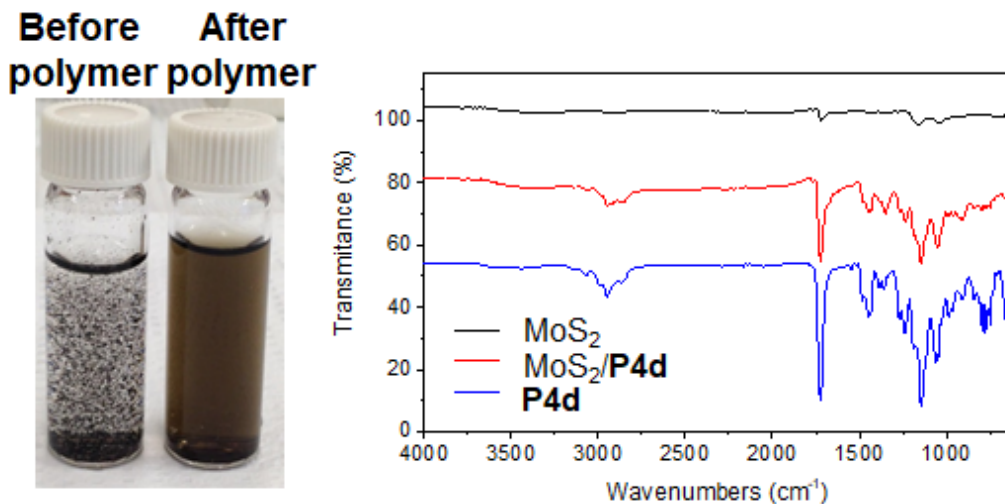


**Figure 2.8.** (Left) Photographs of MoS<sub>2</sub> nanosheets before and after redispersion in THF with and without TTF polymers. (Right): FT-IR of MoS<sub>2</sub>, Polymer **P4d**, and (MoS<sub>2</sub> nanosheets with TTF polymer **P4d** showing the persistence of polymer on the nanosheets after rinsing the nanosheets several times.

the control systems (Figure 2.7E) and dispersed MoS<sub>2</sub> nanostructures from the TTF-polymer solutions (Figure 2.7F). The polymer-TTF/MoS<sub>2</sub> nanocomposites were probed by FT-IR spectroscopy to confirm the presence of polymer on the MoS<sub>2</sub> nanosheets. The polymer-TTF/MoS<sub>2</sub> suspensions were subjected to three centrifugation and redispersion cycles to remove excess polymer, and the resultant nanocomposites used for analysis (Figure 2.8). Signals due to polymer adsorption at 2800-3000cm<sup>-1</sup> (alkyl C-H stretch), and 1723 cm<sup>-1</sup> (carbonyl C=O stretch) were retained for these hybrid systems, demonstrating that the presence of sulfur-rich moieties enable significant interaction of the polymer with the nanosheets. The poly(TTF methacrylate) series proved optimal, with even a low TTF incorporation of 1 mole percent maintaining nanosheet stability for several days. A further experiment demonstrated that block copolymers containing TTF also stabilize MoS<sub>2</sub> nanosheets, however, a study with a series of block compositions must be carried out to understand the influence of polymer architecture on solution stability of TMDCs. As a

control experiment and to reaffirm the notion that sulfur-rich molecules provide significant interactions to MoS<sub>2</sub> nanosheets, a pyrene-containing methacrylate copolymer, with 12 mole percent pyrene-substituted methacrylate and the rest of the composition was poly(sulfobetaine methacrylate) (PSBMA) did not enable nanosheet suspension in solution, suggesting that S-S and S-Mo interactions are more influential than S- $\pi$  interactions for stabilizing chemically exfoliated MoS<sub>2</sub>.<sup>26,27</sup>

## 2.5 Theoretical Considerations

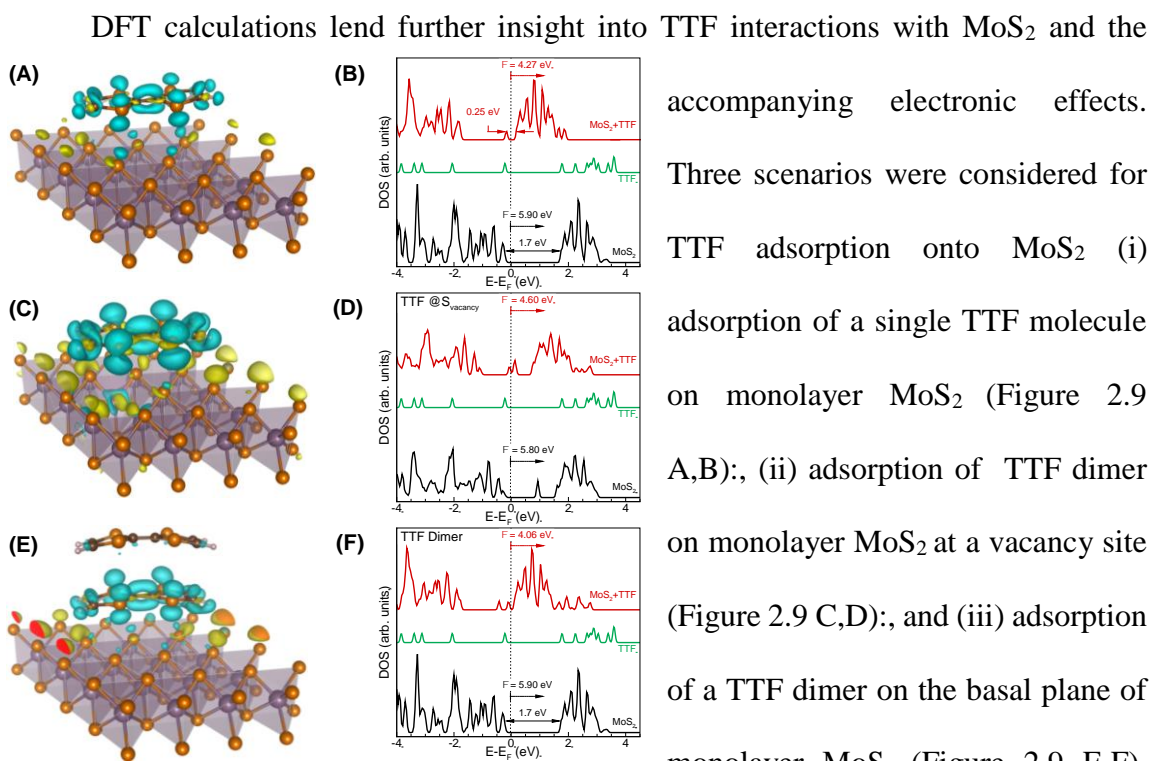


**Figure 2.9:** Results of DFT calculations for TTF on MoS<sub>2</sub> in three scenarios: TTF on pristine MoS<sub>2</sub> (A,B), TTF on MoS<sub>2</sub> with a sulfur vacancy (C,D) and TTF dimer on pristine MoS<sub>2</sub>. Figures A,C, and E are isosurfaces with the cyan representing charge depletion and yellow representing charge accumulation. Figures B,D, and F are density of states plots shown before and after adsorption of TTF to MoS<sub>2</sub>.

Table 2.2 displays the adsorption energies, charge transfer, and work function shifts for each of these cases. The large (negative) adsorption

Table 2.2: Summary of results from DFT calculations

<b><i>Pristine MoS<sub>2</sub> + TTF</i></b>	<b>optB86b-vdW</b>		<b>HSE</b>
	<b><i>4 × 4 MoS<sub>2</sub></i></b>	<b><i>8 × 8 MoS<sub>2</sub></i></b>	<b><i>4 × 4 MoS<sub>2</sub></i></b>
Adsorption Energy	-1.04 eV	-1.13 eV	--
Work function shift	-1.63 eV	-1.53 eV	-1.65 eV
Electrons transferred to MoS <sub>2</sub>	$8.0 \times 10^{12}/\text{cm}^{-2}$	$2.7 \times 10^{12}/\text{cm}^{-2}$	$3.3 \times 10^{12}/\text{cm}^{-2}$
<b><i>MoS<sub>2</sub> with sulfur vacancy + TTF</i></b>	<b><i>4 × 4 MoS<sub>2</sub></i></b>		
Adsorption Energy	-1.20 eV		
Work function shift	-1.20 eV		
Electrons transferred to MoS <sub>2</sub>	$1.8 \times 10^{13}/\text{cm}^{-2}$		
<b><i>Pristine MoS<sub>2</sub> + TTF dimer</i></b>	<b><i>4 × 4 MoS<sub>2</sub></i></b>		
Adsorption Energy	-1.08 eV		
Work function shift	-2.33 eV		
Electrons transferred to MoS <sub>2</sub>	$1.1 \times 10^{13}/\text{cm}^{-2}$		

energy of approximately 1 eV indicates strong TTF interactions with the MoS<sub>2</sub> basal plane, even in the absence of surface defects. The small difference (~70 meV) in TTF adsorption on the 4×4 and 8×8 MoS<sub>2</sub> surfaces (4×4 and 8×8 denoting the number of Mo atoms in the surface lattice) suggests a sufficiently dilute coverage to neglect inter-adsorbate interactions. A basal-plane sulfur vacancy introduced in the MoS<sub>2</sub> lattice increases TTF binding by ~0.2 eV leading to a potential mechanism for suspension stabilization of chemically-exfoliated MoS<sub>2</sub> sheets which tend to have a high density of point defects. As seen in the electrochemical experiments, the other reactive TTF species are also present and most likely contribute to the overall stabilization. It was found that a TTF dimer also binds strongly (~1 eV) in the absence of basal plane defects, with calculations supporting TTF-MoS<sub>2</sub> thermodynamics to be sufficiently robust for surface wetting.

Both binding and electronic interactions of TTF with MoS<sub>2</sub> were considered due to the interest in using these polymers for simultaneous solution and electronic tailoring. For

all adsorption scenarios considered, TTF donates electrons ( $\sim 10^{13}/\text{cm}^2$ ) to the MoS<sub>2</sub> monolayer (*n*-doping), seen in the charge-density difference plots of Figure (2.9 A, C, E), with yellow and cyan indicating charge accumulation and depletion, respectively. The extent of charge transfer is enhanced appreciably by the presence of basal-plane sulfur vacancy defects (*i.e.* larger charge accumulation regions for defect MoS<sub>2</sub>) that presumably act as TTF absorption sites. An examination of the density of states of the TTF-MoS<sub>2</sub> composites (red traces in Figures 2.9 B, D, F) reveals the introduction of flat, dispersionless TTF levels close to the conduction band edge of the pristine MoS<sub>2</sub> monolayer, with the Fermi level lying near the MoS<sub>2</sub> conduction band edge consistent with *n*-doping. However, for an MoS<sub>2</sub> monolayer with a sulfur vacancy, the TTF level merges with the vacancy defect level within the band gap of MoS<sub>2</sub>, the Fermi level now being pinned at this energy. While the extent of charge transfer is greater in this case, the vacancy defect may function as a deep trap affecting charge conduction through MoS<sub>2</sub>. As expected for *n*-doping, we find a considerable decrease in the work-function of MoS<sub>2</sub> ranging from 1.2 eV for the defective monolayer to 1.8 eV for TTF dimer adsorption. The magnitude of these shifts reflect an idealized situation of a freestanding MoS<sub>2</sub> monolayer and should be interpreted as an upper bound – variations in MoS<sub>2</sub> layer thickness, adsorbate coverage, and substrate-doping effects will impact experimental findings. Nevertheless qualitative trends observed in work function and charge transfer are consistent with experiments.

While the optB86b-vdW functional provides a better description of van der Waals interactions,<sup>28</sup> this semi-local DFT functional is prone to excessive electron delocalization due to self-interaction errors.<sup>29-31</sup> This leads to errors in electronic structure with deleterious

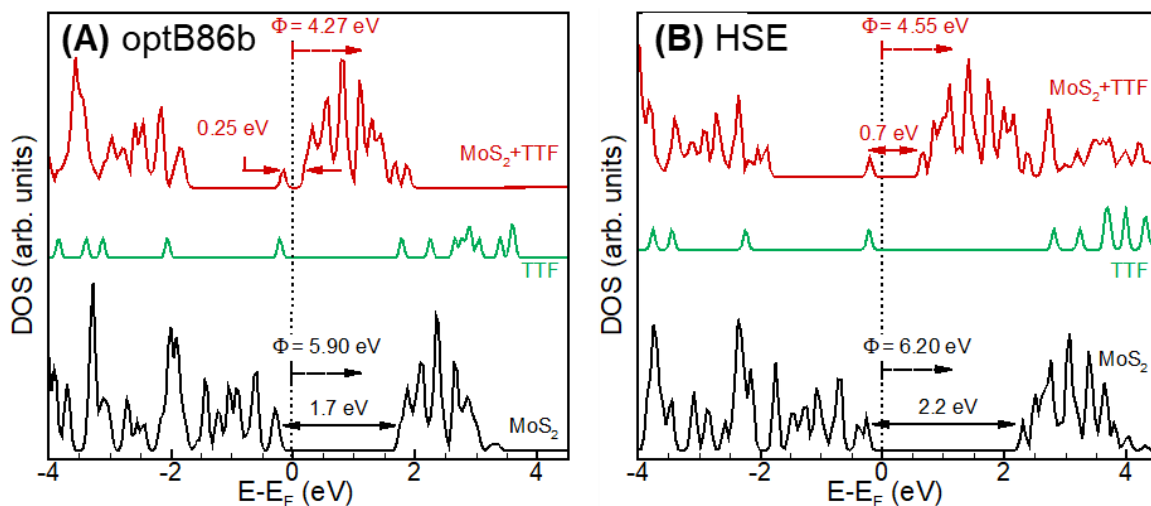


**Figure 2.10.** Comparison of the two methods used for DFT calculations (A) optB86b and (B) Heyd-Scuseria-Ernzerhof (HSE) hybrid-DFT functional

consequences for predicting observables such as charge transfer and work function shifts.

The inclusion of a fraction of exact exchange within DFT (hybrid DFT) provides a computationally tractable means of decreasing the self-interaction error. Thus, the Heyd-Scuseria-Ernzerhof (HSE) hybrid-DFT functional was employed, which is more accurate than standard DFT across a range of gapped and molecular systems. Due to its computational expense, the HSE functional was employed solely to study TTF on a  $4 \times 4$  MoS<sub>2</sub> monolayer, and the trends identified were consistent with the optB86b studies. Figure 2.10 displays the density of states obtained from the optB86b-vdW and the HSE functional for a TTF molecule adsorbed on a  $4 \times 4$  MoS<sub>2</sub> monolayer. The optB86b-vdW functional predicts about double the charge transfer from TTF to MoS<sub>2</sub> as compared to the HSE functional (see Table 2.2), which is likely due to excessive electron delocalization for the former method. Note that the TTF adsorbate introduces a defect level within the MoS<sub>2</sub> band gap at 0.25 and 0.7 eV from the conduction band edge of pristine MoS<sub>2</sub> as calculated using the optB86b-vdW and HSE functional, respectively. As expected, with *n*-doping of the

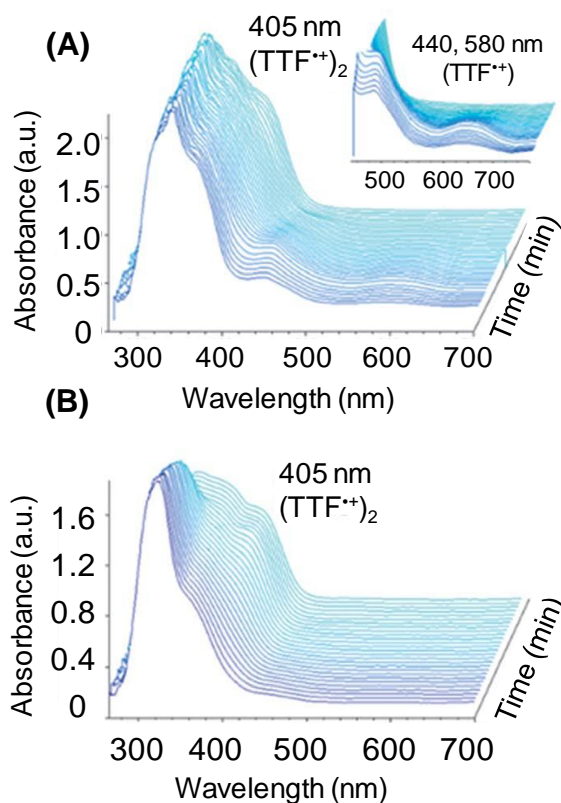


**Figure 2.11.** Time-resolved UV-Vis spectroscopy of MoS<sub>2</sub> nanosheets in the presence of (A) small molecule TTF and (B) polymer **P4a**.

components, indicating no ground state electronic interactions. This is likely due to the large difference in the band energies imposed by defects. Employing a mild MoS<sub>2</sub> exfoliation by sonicating MoS<sub>2</sub> powder in NMP produces few layer nanosheets with much lower defect density thereby retaining the electronic structure of semiconducting 2H MoS<sub>2</sub>. The 2H symmetry and sulfur-rich basal plane, characteristic of the semiconducting allotrope, were confirmed by high resolution TEM. The resulting suspensions were subjected to *in situ* UV-VIS experiments upon addition of TTF in NMP. As shown in Figure 2.11a, TTF radical cation absorption peaks evolved at 440 and 580 nm, indicating ground state electron transfer from TTF to MoS<sub>2</sub>. At later times, the relative intensities of

MoS<sub>2</sub> monolayer, we find a decrease in the overall work-function of the TTF-MoS<sub>2</sub> composite the optB86b-vdW and HSE results being nearly similar (~1.6 eV work function shift).

## 2.6 Electronic Interactions of TTF polymers with MoS<sub>2</sub>

The UV-Vis absorption signatures of the chemically exfoliated MoS<sub>2</sub> suspensions with the TTF polymers resembled the superimposition of the two

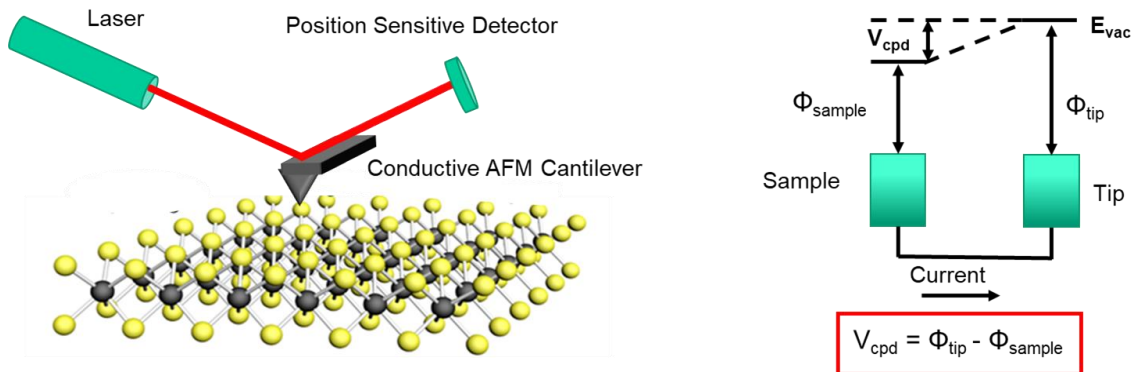


**Figure 2.12.** (Left) Physical representation of KPFM as a scan probe technique and (Right) a simple band diagram showing the equalization of work functions of the sample and the tip with the voltage required to maintain this balance recorded as surface potential contrast (SPC).

the peaks decreased, and a strong signal evolved at 405 nm, characteristic of an intramolecular transition of the TTF  $\pi$ -dimer. These signals are similar to the electrochemistry results on TTF polymers, demonstrating TTF<sup>+</sup>-TTF dimerization followed by a second electron transfer event occurring at an identical electrochemical potential. Treating MoS<sub>2</sub> suspensions with the TTF-polymers (Figure 2.11b) resulted in no radical cation features, and instead a replacement of the neutral TTF absorption at 450 nm by a dimer signal at 405 nm. These spectral characteristics likely result from the proximity of the TTF moieties on the polymer backbone. Such findings suggest robust electronic interactions between TTF and MoS<sub>2</sub>, with the extent of doping amplified by employing the macromolecular versions of TTF. Additionally, the affinity between MoS<sub>2</sub> and TTF platforms is supported further by the short-range interaction inherent to ground state charge transfer shown in the spectroscopic experiments.

Kelvin probe force microscopy (KPFM) was coupled with photoluminescence (PL) spectral imaging to investigate the effect of electron doping by TTF polymer **P1e** on MoS<sub>2</sub> work function. KPFM is an electric force scanning probe technique that exploits a



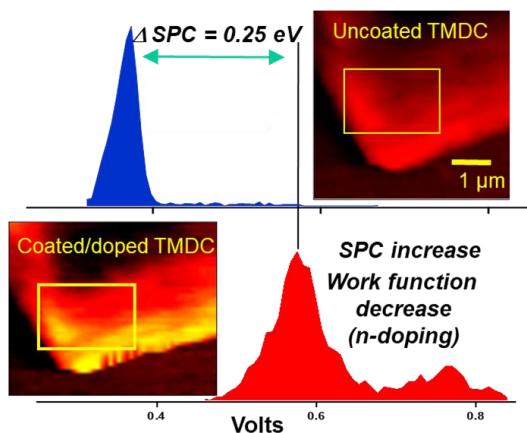


**Figure 2.13:** KPFM SPC images before and after addition of TTF polymers and their corresponding histograms showing an increase in the SPC and representing n-doping of MoS<sub>2</sub>.

shown in Figure 2.12). In the experiments described here, mechanically exfoliated MoS<sub>2</sub> flakes were located on a clean glass slide and the PL spectra recorded at different locations on the flake along with surface heights and SPC measurements on these areas of interest. Electronic interactions of TTF on MoS<sub>2</sub> were quantified by drop-casting TTF polymer **P1e** on an MoS<sub>2</sub> flake: the coated flake was dried, and the AFM and KPFM measurements were repeated to reveal the effect of polymer doping on the MoS<sub>2</sub> work function from the same flake.

Figure 2.13 shows the SPC image of the (undoped) MoS<sub>2</sub> flake on glass with SPC values measured before and after polymer doping. Also shown are the normalized histograms of SPC values in the labeled regions of interest before and after polymer doping. After doping, a reproducible upshift in SPC of about 240 mV was observed. The upshift in SPC is consistent with a decrease in the ionization potential (and work function) of MoS<sub>2</sub>. As a control experiment, the glass substrate was scanned, without MoS<sub>2</sub>, before and after

capacitive interaction between a metallized cantilever probe and the underlying material. This interaction is either attractive or repulsive, depending on the sign of the work function of the probe and sample, thus measuring the local contact or surface potential contrast (SPC) between a Pt-coated atomic force probe and the underlying substrate (Working principle

polymer doping to understand the contribution of the polymer to the SPC. After polymer coating, there was only a shift in the SPC by  $\sim 80$  meV suggesting very little contribution to the overall work function change seen with MoS<sub>2</sub> as the underlying substrate. We additionally note a positive dependence on SPC upshift with increasing PL intensity (decreasing layer thickness) of MoS<sub>2</sub>, consistent with a ‘dilution’ of the effect of carrier doping by the polymer in multi-layer MoS<sub>2</sub>.

## **2.7: Conclusions**

The work presented in this chapter described the synthesis and utilization of novel TTF-containing polymers that afford an opportunity for non-covalent surface functionalization, band structure modulation and work-function engineering of MoS<sub>2</sub> nanosheets. These polymers impart solution stability of chemically exfoliated MoS<sub>2</sub> nanosheets, while coordinative binding and ground state electron transfer are observed for MoS<sub>2</sub> with the pristine, sulfur-rich basal plane. The TTF-substituted polymers behave differently from TTF itself, readily forming TTF dimers at the polymer-MoS<sub>2</sub> interface that amplify surface binding and electronic interactions. TTF-based polymers afford robust, non-covalent interactions regardless of the MoS<sub>2</sub> lattice structure, conceptually in parallel with graphene-pyrene coordination. Tandem photoluminescence spectroscopy/Kelvin probe microscopy experiments reveal a decrease in work function for MoS<sub>2</sub> coated with the TTF-containing polymer. The trends elucidated experimentally are consistent with those predicted using first-principles DFT calculations providing a robust theory/experiment feedback loop that can be used to identify synthetic structures to significantly impact the properties of TMDCs.

## 2.8 References

1. Secor, E. B., Ahn, B. Y., Gao, T. Z., Lewis, J. A. & Hersam, M. C. Rapid and Versatile Photonic Annealing of Graphene Inks for Flexible Printed Electronics. *Adv. Mater.* **27**, 6683–6688 (2015).
2. Ballesteros-Garrido, R., Rodriguez, R., Álvaro, M. & Garcia, H. Photochemistry of covalently functionalized graphene oxide with phenothiazinyl units. *Carbon N. Y.* **74**, 113–119 (2014).
3. Kim, Hyunwoo; Abdala, Ahmed; Macosco, C. Graphene/Polymer Nanocomposites. *Macromolecules* **43**, 6515–6530 (2010).
4. Alon, H. *et al.* Lithographically Patterned Functional Polymer-Graphene Hybrids for Nanoscale Electronics. *ACS Nano* **12**, 1928–1933 (2018).
5. Ding, Q. *et al.* Basal-Plane Ligand Functionalization on Semiconducting 2H-MoS<sub>2</sub> Monolayers. *ACS Appl. Mater. Interfaces* **9**, 12734–12742 (2017).
6. Liu, Z. *et al.* Preparation of graphene/polymer composites by direct exfoliation of graphite in functionalised block copolymer matrix. *Carbon* **51**, 148–155 (2013).
7. Hsu, C.-L. *et al.* Layer-by-Layer Graphene/TCNQ Stacked Films as Conducting Anodes for Organic Solar Cells. *ACS Nano* **6**, 5031–5039 (2012).
8. Dey, S., Matte, H. S. S. R., Shirodkar, S. N., Waghmare, U. V. & Rao, C. N. R. Charge-transfer interaction between few-layer MoS<sub>2</sub> and tetrathiafulvalene. *Chem. - An Asian J.* **8**, 1780–1784 (2013).
9. Tian, X. *et al.* Effects of 3d transition-metal doping on electronic and magnetic properties of MoS<sub>2</sub> nanoribbons. *Phys. Chem. Chem. Phys.* **17**, 1831–1836 (2015).
10. Lin, X. & Ni, J. Charge and magnetic states of Mn-, Fe-, and Co-doped monolayer MoS<sub>2</sub>. *J. Appl. Phys.* **116**, (2014).
11. Sánchez, V., Benavente, E., Ana, M. A. S. & González, G. High electronic conductivity molybdenum disulfide-dialkylamine nanocomposites. *Chem. Mater.* **11**, 2296–2298 (1999).
12. Osim, W., Stojanovic, A., Akbarzadeh, J., Peterlik, H. & Binder, W. H. Surface modification of MoS<sub>2</sub> nanoparticles with ionic liquid-ligands: Towards highly dispersed nanoparticles. *Chem. Commun.* **49**, 9311–9313 (2013).
13. Jing, Y., Tan, X., Zhou, Z. & Shen, P. Tuning electronic and optical properties of MoS<sub>2</sub> monolayer via molecular charge transfer. *J. Mater. Chem. A* **2**, 16892–16897 (2014).

14. Canevet, D., Salle, M., Zhang, G., Zhang, D. & Zhu, D. Tetrathiafulvalene (TTF) derivatives: key building-blocks for switchable processes. *Chem. Commun.* 2245–2269 (2009). doi:10.1039/b818607n
15. Kaplan, M. L., Haddon, R. C., Wudl, F. & Feit, E. D. Preparation of Some Monophenyltetrathiafulvalenes and (p-Vinylphenyl)tetrathiafulvalene and Its Polymerization. *J. Org. Chem.* **43**, 4642–4646 (1978).
16. Shimizu, T. & Yamamoto, T. Preparation of a new poly(arylacetylene) with a tetrathiafulvalene (TTF) unit in the side chain. *Chem. Commun.* 515–516 (1999). doi:10.1039/a900300b
17. Pittman, C. U., Mitsuru, U. & Liang, Y. F. Synthesis and Polymerization of p-(2-Tetrathiafulvalenyl)phenyl Methacrylate. *J. Org. Chem.* **44**, 3639–3642 (1979).
18. Love, J *et al.* A Practical and Highly Active Ruthenium-Based Catalyst that Effects the Cross Metathesis of Acrylonitrile. *Angew. Chemie Int. Ed.* **41**, 4035–4037 (2002).
19. Shon, Y. S. & Lee, T. R. Catalytic ring-closing olefin metathesis of sulfur-containing species: Heteroatom and other effects. *Tetrahedron Lett.* **38**, 1283–1286 (1997).
20. Bielawski, C. W. & Grubbs, R. H. Increasing the initiation efficiency of Ruthenium-based ring-opening metathesis initiators: Effect of excess phosphine. *Macromolecules* **34**, 8838–8840 (2001).
21. Chiang, P. T., Chen, N. C., Lai, C. C. & Chiu, S. H. Direct observation of mixed-valence and radical cation dimer states of tetrathiafulvalene in solution at room temperature: association and dissociation of molecular clip dimers under oxidative control. *Chem. - A Eur. J.* **14**, 6546–6552 (2008).
22. Huchet, L. *et al.* Spectroelectrochemistry of Electrogenerated Tetrathiafulvalene-Derivatized Poly(thiophenes): Toward a Rational Design of Organic Conductors with Mixed Conduction. *J. Phys. Chem. B* **102**, 7776–7781 (1998).
23. Joenson, P., Frindt, R. & Morrison, S. Single Layer MoS<sub>2</sub>. *MRS Bull.* **21**, 457–461 (1986).
24. Splendiani, A. *et al.* Emerging photoluminescence in monolayer MoS<sub>2</sub>. *Nano Lett.* **10**, 1271–1275 (2010).
25. Wieting, T. J. & Verble, J. L. Infrared and Raman Studies of Long-Wavelength Optical Phonons in Hexagonal MoS<sub>2</sub>. *Phys. Rev. B* **3**, 4286–4292 (1971).
26. Yoshizawa, M., Kumazawa, K. & Fujita, M. Room-temperature and solution-state observation of the mixed-valence cation radical dimer of tetrathiafulvalene,

- [(TTF)<sub>2</sub>]<sup>+</sup>., within a self-assembled cage. *J. Am. Chem. Soc.* **127**, 13456–13457 (2005).
27. Spruell, J. M. *et al.* Highly stable tetrathiafulvalene radical dimers in [3]catenanes. *Nat. Chem.* **2**, 870–879 (2010).
  28. Klimeš, J., Bowler, D. R. & Michaelides, A. Chemical accuracy for the van der Waals density functional. *J. Phys. Condens. Matter* **22**, (2010).
  29. Heyd, J., Scuseria, G. & Ernzerhof, M. Hybrid functionals based on a screened Coulomb potential. *J. Chem. Phys.* **118**, 8207–8215 (2003).
  30. Janesko, B. G., Henderson, T. M. & Scuseria, G. E. Screened hybrid density functionals for solid-state chemistry and physics. *Phys. Chem. Chem. Phys.* **11**, 443–454 (2009).
  31. Kümmel, S. & Kronik, L. Orbital-dependent density functionals: Theory and applications. *Rev. Mod. Phys.* **80**, 3–60 (2008).

## CHAPTER 3

### BITHIAZOLIDINYLIDENE POLYMERS AS P-DOPANTS FOR MoS<sub>2</sub>

#### 3.1: Introduction

This chapter focuses on work function modulation of MoS<sub>2</sub> using polymers bearing sulfur-rich electron acceptor. Building upon previous insight from Chapter 2, the application of polymers with electroactive functionalities alter the intrinsic conduction properties of TMDCs and with sufficient interaction with the basal plane, endows the TMDC with solution properties of the polymer.<sup>1</sup> While Chapter 2 highlighted electron donating TTF, this chapter details the synthesis of novel functional derivatives of electron accepting bithiazolidinylidene (BT) and their incorporation into polymers. These polymers are used as work function modifiers for single layer CVD grown MoS<sub>2</sub> and are anticipated to *increase* the work function which is the complementary situation seen for TTF. Examples of electron donating materials that decrease the work function of TMDCs (n-doping) are more prevalent than organic moieties that increase the work function (p-doping) of TMDCs. Fabricating systems that include both types of dopants are advantageous as complementary doping is necessary to access p-n junction devices. While TTF was shown to n-dope, the focus in this chapter is on p-doping by non-covalent physisorption without disturbing the inherent TMDC structure.

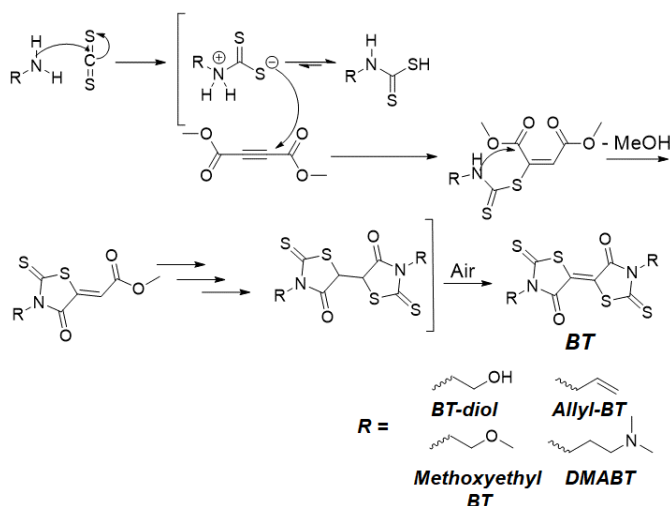
BTs are sulfur-rich electron acceptors composed of two rhodanine rings linked together through an alkene bridge. Complementary to TTF, BT undergoes two reversible redox potentials positioned at -0.20 V and -0.61 V, with potentials comparable to the

known electron accepting tetracyanoquinonedimethane (TCNQ).<sup>2</sup> As with TTF, the sulfur-rich structure and electron accepting behavior of BTs are anticipated to be effective p-dopants with the sulfur adding surface interactions through sulfur-sulfur van der Waals forces. Knott and Jeffreys first reported the synthesis of BTs as an unwanted biproduct during the synthesis of sulfur-containing merocyanine dyes via condensation with functional rhodanines.<sup>3</sup> Nagase detailed the first intentional synthesis of BT through the reaction of dithiocarbamates and dimethylacetylene dicarboxylate (DMAD) and later on discovered an alternative synthesis by treating bis(alkylthio)malonitrile with dithiocarbamic acids.<sup>4,5</sup> However, all of the above reactions required multiple steps and only low yields were obtained. Recently, a one-pot synthesis of BT-diones was reported by Nasiri, *et al.* in which aliphatic primary amines were reacted with carbon disulfide to quickly generate the dithiocarbamic acid *in situ* and then further reacted with dimethylacetylene dicarboxylate in a 2:1 molar ratio to form aliphatic BT derivatives.<sup>6</sup> This methodology is advantageous because it produces multigram quantities of BT derivatives without the need for rigorous chromatographic purification. This report only demonstrated a few functional BT derivatives<sup>7,8</sup> and the literature completely lacks reports of BT-containing polymers. Therefore, functional BT derivatives, capable of integration into polymers were synthesized, with the aim of using these materials as p-dopants for MoS<sub>2</sub>.

### **3.2: Synthesis of Functional BT Monomers and Polymers**

Reacting functional primary amines with carbon disulfide formed the corresponding dithiocarbamic acid as indicated by a color change to bright yellow solutions. Slow addition of DMAD at 0 °C, yielded functional BT monomers including

Scheme 3.1: Mechanism of BT Formation

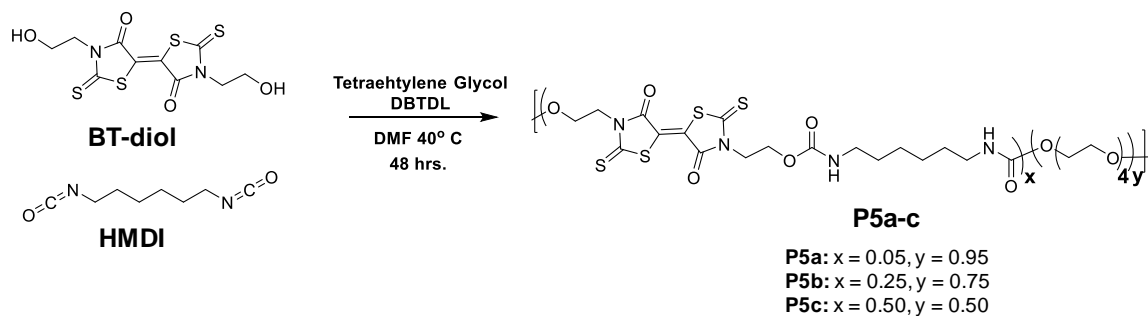


(BT-diol, allyl BT, methoxyethyl BT, and dimethylaminopropyl BT (DMABT) in yields approaching 50%. The mechanism of BT formation is shown in Scheme 3.1; after the formation of the dithiocarbamic acid, the carboxylate anion under addition across the

alkyne, followed by cyclization and elimination of methanol, affording the desired rhodanine. Acting on both sides of the alkyne, the non-conjugated birhodanine adduct is formed which is oxidized to BT upon exposure to air. Attempts to use aniline as the primary amine were unsuccessful, likely due to its lower nucleophilicity in the cyclization step. DMABT and allyl BT are amenable to a range of polymerizations including olefin metathesis<sup>9</sup>, thiol-ene<sup>10</sup>, and Menshutkin-type polymerization.<sup>11</sup> However, all of these polymerization conditions yielded no polymer and either starting material or degraded monomer. The synthetic accessibility of BT-diol afforded multi-gram quantities and prompted polycondensation reactions with diisocyanates to form polyurethanes. Attempted homopolymerization of BT-diol with hexamethylene diisocyanate (HMDI) in DMF led to insoluble product, with precipitation occurring before high conversion was achieved. Fortunately, copolymerization of BT-diol with HMDI and tetraethyleneglycol performed at 40 °C, using dibutyltin dilaurate (DBTDL) as catalyst, produced soluble BT-



Scheme 3.2: Synthesis of BT-containing polymers **P5a-c**



polyurethanes in high yields (~80-90%) (Scheme 3.2). Polymers **P5a-c** with varied BT incorporations were synthesized, with experimentally determined BT content corresponding closely to the monomer feed ratio. Polymer formation was monitored by  $^1\text{H}$  NMR spectroscopy, noting loss of the hydroxyl resonances at  $\delta 4.9$  ppm and appearance of urethane -NH signals at  $\delta 7.0$ - $7.1$  ppm. The presence of BT groups in the polymers was further confirmed by  $^{13}\text{C}$  NMR spectroscopy, specifically noting the dithiocarbamate ( $\delta 195$  ppm), BT carbamate ( $\delta 167$  ppm), and BT alkene ( $\delta 124$  ppm) resonances (Figure 3.1A). Polymer molecular weight distributions, measured by gel permeation chromatography

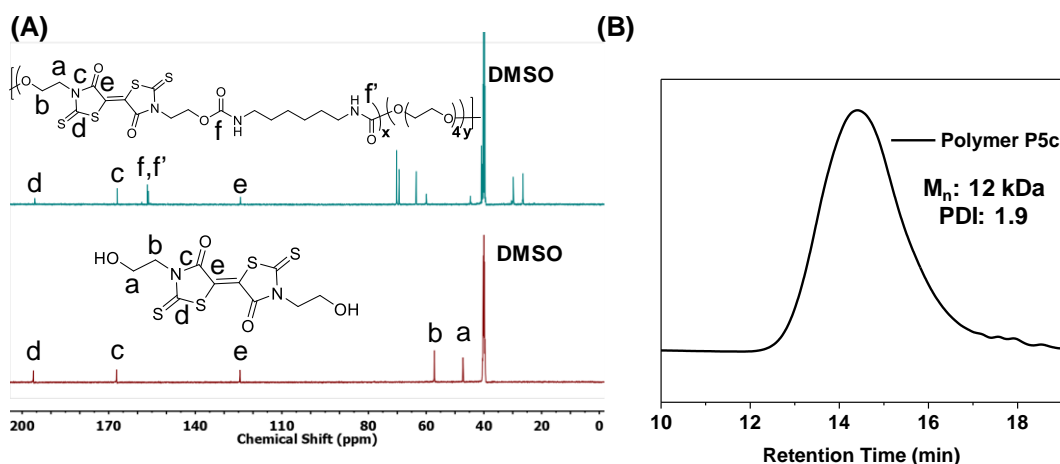


**Figure 3.1.** (A)  $^{13}\text{C}$  NMR of BT-diol and Polymer **P5b** showing the BT ( $\delta 195$ ,  $\delta 167$ , and  $\delta 124$  ppm) and urethane ( $\delta 157$  ppm) resonances. (B) Gel permeation chromatograph showing the monomodal molecular weight distribution from polymer **P5c**.

(GPC), were monomodal with molecular weights ranging from 12-30 kDa and dispersity values of  $\sim 2.0$  (Figure 3.1B), typical of step-growth polymerization.

### 3.3: BT Stability

The UV-Vis spectrum of BT-diol in DMF at room temperature showed absorption maxima at 440 and 425 nm for the 0-0 and 0-1 ground state transitions, respectively, with the onset of absorption yielding an optical bandgap of  $\sim 2.5$  eV. It was noted during previous experiments that a color change takes place at elevated temperatures going from yellow to colorless in a few hours. Temperature-dependent UV-Vis spectroscopy showed

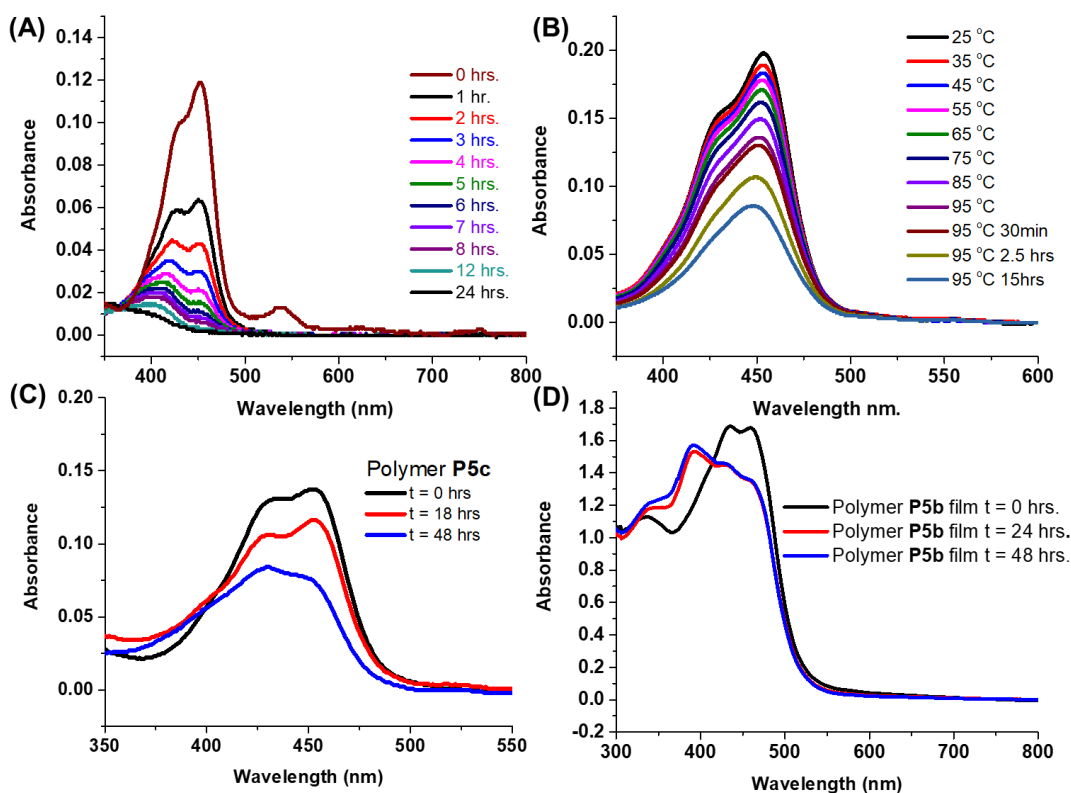


**Figure 3.2.** (A) UV-Vis spectrum of BT-diol showing degradation after heating at 100 °C for 24 hrs. (B) UV-Vis spectrum of BT-diol after heating in 10 °C increments up to 95 °C showing that degradation begins at 65-75 °C. (C) UV-Vis spectrum of Polymer P5c showing degradation after heating at 100 °C for 48 hrs. (D) Thin film UV-Vis of polymer P5b showing no degradation after 48 hrs. and the appearance of a new peak at 380 nm.

that upon heating at 100 °C in DMF, the absorbance intensity for BT at 440 nm decreased, and no new signals appeared (Figure 3.2A). Furthermore, the onset of the signal decrease does not occur until roughly 55-65 °C (Figure 3.2B). UV-Vis spectroscopy of polymer **P5b** in DMF showed similar quenching behavior to that of BT-diol, with signatures fully diminishing after 24 hours (Figure 3.2C). Interestingly, UV-Vis spectra of thin films of polymer **P5b** displayed no decrease in absorbance after 2 days at 100 °C on a quartz slide and a new peak appeared at 380 nm (Figure 3.2D) which is attributed to morphological changes in the thin film. NMR spectra recorded on the thin film, after heating, confirmed the absence of chemical degradation to suggest that the BT moiety is stable in the solid state, suggesting a concentration-dependent stability and the ability to use thin films of BT polymers as thin film dopants for MoS<sub>2</sub>.

The differing stability observed in dilute solution and thin films led us to further investigate the solution stability of BT-based structures by NMR spectroscopy. A 0.01 M solution of monomer allyl-BT in DMSO-*d*<sub>6</sub> heated at 100 °C for two days, yielded multiple

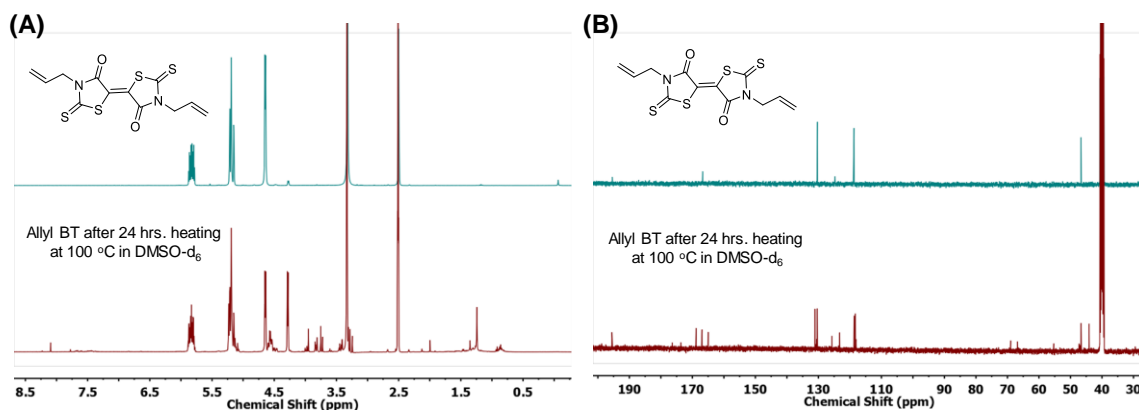


**Figure 3.3.** (A) <sup>1</sup>H NMR spectra of allyl-BT before and after heating a 100 °C in DMSO-*d*<sub>6</sub> showing the appearance of a new methylene resonance. (B) <sup>13</sup>C NMR spectra of allyl-BT before and after heating a 100 °C in DMSO-*d*<sub>6</sub> showing the appearance of a new carbamate and olefin resonances suggesting breaking of molecular symmetry.

degradation products, indicated by thin layer chromatography (TLC).  $^1\text{H}$  NMR spectroscopy of the crude reaction mixture confirmed retention of the allylic protons and showed new methylene resonances at 4.47 ppm.  $^{13}\text{C}$  NMR spectroscopy displayed the expected thiocarbonyl peak (195 ppm), and new carbonyl, allyl, and olefinic carbons suggesting a break in symmetry of the BT moiety (Figure 3.3A,B). Further studies would be needed to identify the degradation products and is beyond the scope of the current studies; however, the thin film thermal stability is encouraging for proceeding with these studies.

Polyurethane copolymers consisting of hard and soft segments undergo phase separation upon thermal or solvent annealing.<sup>12-14</sup> In the current polymer system, BT is the hard segment and tetraethylene glycol is the soft segment. To understand morphological changes in the BT polymers that may alter spectroscopic signatures, small angle x-ray

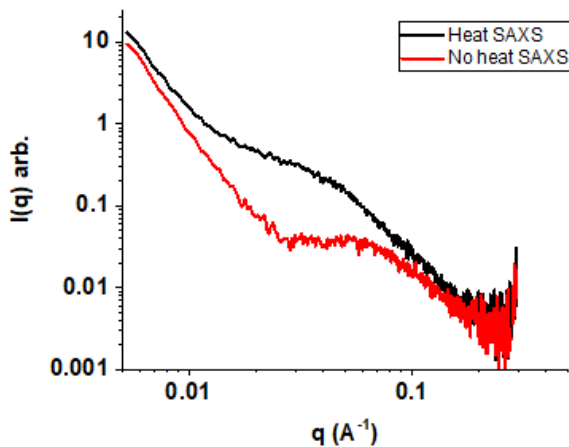


**Figure 3.4.** Small angle x-ray scattering (SAXS) diffractogram of polymer **P5b** showing the evolution of the domain size from 5 nm to 10 nm after annealing at 100 °C for 24 hrs.

scattering (SAXS) was performed on a thin film of polymer **P5b** before and after heating at 100 °C for 24 hours (Figure 3.4). A broad peak, indicative of microphase separation in polyurethanes, showed a domain size of 5 nm for the BT rich phase.

After heating, the peak shifted to lower  $q$  values, resulting in a domain size of 10 nm for the BT-rich phase.

The increase in domain size can have many implications for the optical behavior of BT due to the obtained molecular degrees of freedom the BT moiety has upon phase ripening. The shifts observed in the absorbance spectra of these polymers could be due to different molecular orientations and/or changes in the crystalline domain sizes or stacking. However, even with these morphological changes, there is no degradation or significant observable electronic structure alterations BT polymers undergo that would affect the nature of our studies.

### 3.4: Electronic Impacts of BT polymers on MoS<sub>2</sub>

KPFM was performed on single layer CVD grown MoS<sub>2</sub> both before and after the addition of BT polymers to the substrate. The first scans of the substrate showed mainly monolayer and bilayer MoS<sub>2</sub> with a roughly 1 nm step height difference corresponding to a single MoS<sub>2</sub> layer (the height and SPC images also revealed other components on the

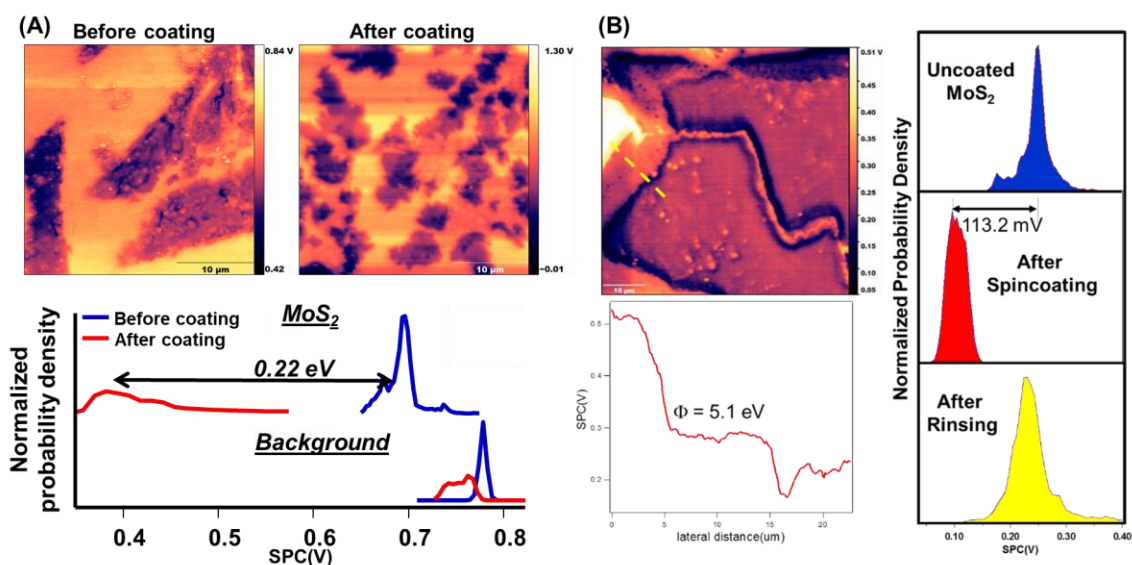


**Figure 3.5.** (A) KPFM of MoS<sub>2</sub> on Si/SiO<sub>2</sub> before and after coating with polymer **P5b** and the corresponding SPC histograms showing a 0.22 eV decrease after coating, indicative of p-doping. (B) SPC image and histograms showing the recovery of the MoS<sub>2</sub> work function after rinsing the polymer from the MoS<sub>2</sub> flake.

surface, potentially dust, but this did not alter the work function of MoS<sub>2</sub>). The SPC image of the uncoated substrate revealed work function values of 5.17 eV for monolayer flakes (Figure 3.5A). Upon drop-casting a very dilute solution (0.001 mg/mL) of polymer **P5b** onto the TMDC monolayer (resulting in roughly a 3 nm polymer coating) and rescanning the surface, a 0.22 V downshift in SPC was observed. This *negative shift* in SPC correlates to a *work function increase* of MoS<sub>2</sub>, pushing the Fermi energy of MoS<sub>2</sub> closer to the valance band edge, indicative of p-doping.<sup>15</sup> Interestingly, after rinsing the substrate with chloroform, and scanning the same area, the work function reverted back to its initial value of 5.2 eV indicating the potential for reversible doping, useful for the development of patternable dopants (Figure 3.5B). Control experiments to understand if residual solvent had any effect on the work function modulation of MoS<sub>2</sub>, showed almost no shift in the SPC of a Si/SiO<sub>2</sub> substrate after dropcasting chloroform and allowing it to dry in air. Furthermore, a control experiment only scanning the polymer revealed that the MoS<sub>2</sub> work function is the only material property being probed and that the scans are probing solely polymer.

### 3.5: Electrochemistry of BT polymers

Cyclic voltammetry (CV) was performed to examine the redox properties and energetics of the functional BT monomers and polymers. Figure 3.6 (left) shows CV data acquired for BT-diol, methoxyethyl BT, and polymer **P5c**, in DMF using tetra-*n*-butylammonium hexafluorophosphate as the electrolyte. The voltammogram of methoxyethyl BT shows reversible redox potentials at -0.05 and -0.89 V, yielding a more negative reduction potential than electron acceptors such as TCNQ ( $E^{1/2} = -0.06$  V). Using

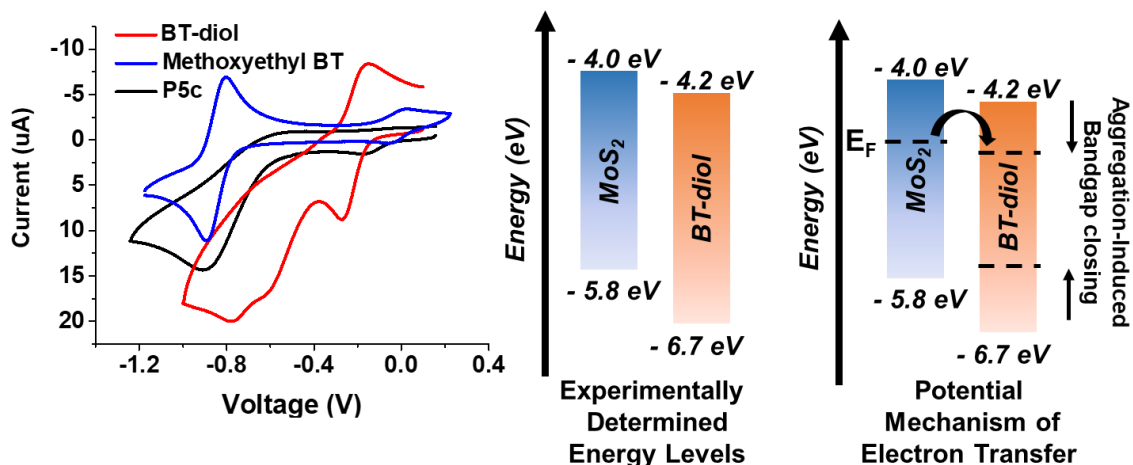


**Figure 3.6.** (Left) Cyclic voltammograms of BT-diol, methoxyethyl BT and polymer **P5c**. (Center) Energy band diagram constructed from the redox potentials and band gap from the UV-Vis traces indicating non-favorable overlap for ground state charge transfer. (Right) Energy band diagram showing the potential mechanism of doping do to aggregation induced bandgap closure and intrinsically n-doped MoS<sub>2</sub>.

methoxyethyl BT as a model compound, the voltammogram of BT-diol exhibited only one reversible reduction event, suggesting that the hydroxyl groups impede reduction to the dianion. Polymer **p5c** showed a quasi-reversible first reduction and irreversible second reduction, similar to allyl BT (Reduction potentials for all BT compounds are reported in

Table 3.1: Summary of reduction potentials for functional BT monomer and polymers

Compound	$E_1^{1/2}$ (V)	$E_2^{1/2}$ (V)
TTF	0.36	0.61
TCNQ	-0.064	-0.61
BT-diol	-0.21	-
Allyl BT	-0.78	-1.4
Methoxyethyl BT	-0.04	-0.85
DMABT	-0.04	-0.58
P5a	-0.53	-
P5b	-0.5	-0.88
P5c	-0.1	-0.53

Table 3.1). From the onset of the reduction peaks observed by CV, and absorptions in the UV-Vis spectra, the energy levels of the BT-containing structures were estimated. Figure 3.6 (center) compares the experimentally determined energy levels of

BT diol with that of monolayer MoS<sub>2</sub>. Interestingly, the MoS<sub>2</sub>/BT, donor/acceptor system is not ideal for ground state charge transfer of electrons from MoS<sub>2</sub> to BT, a requirement for p-doping from a thin film. Many factors may contribute to a plausible doping mechanism including narrowing of the BT bandgap due to aggregation and/or an inherently n-doped MoS<sub>2</sub> substrate, pushing the Fermi level closer to the conduction band of MoS<sub>2</sub> (Figure 3.6 right).<sup>16</sup> This would provide a path for electron transfer to BT, increasing the work function of MoS<sub>2</sub>. However, further studies are required to identify the exact mechanism of charge transfer.

### 3.6 Conclusions

In summary, novel solution processible BT-containing polymers were synthesized, in which the BT-content was controlled by the selected monomer feed ratios. These step-growth polymerizations proceeded to high molecular weights, producing solution processible coatings for TMDCs. KPFM measurements of CVD-grown MoS<sub>2</sub>, after coating with BT-containing polymers, showed a work function increase of 0.16 eV over native MoS<sub>2</sub>, consistent with p-doping of the 2D material. This behavior is striking, as the experimentally determined energy levels of BT and MoS<sub>2</sub> suggest unfavorable energetics for ground state electron transfer. However, the pronounced p-doping indicates a different doping mechanism than initially predicted such as aggregation-induced bandgap reduction and inherently doped substrate contributing to band structure changes in the BT/MoS<sub>2</sub> system, warranting further investigation. While there are numerous examples of work function lowering (n-doping) materials for TMDCs, this work uncovers an unusual case of TMDC *p-doping*, pertinent for broadening the scope 2D material devices. Moreover, these



chalcogen-rich polymers can be used as a synthetic template for molecular design using other TMDCs to expand the scope of non-covalent doping routes.

### 3.7 References

1. Selhorst, R. C. *et al.* Tetrathiafulvalene-containing polymers for simultaneous non-covalent modification and electronic modulation of MoS<sub>2</sub> nanomaterials. *Chem. Sci.* **7**, 4698–4705 (2016).
2. Jaeger, C. D. & Bard, A. J. Electrochemical Behavior of Tetrathiafulvalene-Tetracyanoquinodimethane Electrodes in Aqueous Media. *J. Am. Chem. Soc.* **101**, 1690–1699 (1979).
3. Knott, E. B. & Jeffreys, R. A. Compounds Containing Sulphur Chromophores. Part II. Attempts to Prepare Sulphide Analogues of Merocyanines. *J. Chem. Soc.* 927–933 (1955).
4. Nagase, H. Studies on Fungicides. XXV. Addition Reaction of Dithiocarbamates to Fumaronitrile, Bis(alkylthio)maleonitrile, 2,3,-Dicyano-5,6-dihydro-1,4-dithiin and 4,5-Dicyano-2-oxo-1,4-dithiol. *Chem. Pharm. Bull.* **22**, 505–513 (1973).
5. Nagase, H. Studies on Fungicides. XXII. Reaction of Dimethyl Acetylenedicarboxylate with Dithiocarbamates, Thiocarbamates, Thiosemicarbazides and Thiosemicarbazones. *Chem. Pharm. Bull.* **21**, 279–286 (1972).
6. Nasiri, F., Zolali, A. & Asadbegi, S. Solvent-free One-pot Synthesis of 2,2'-dithioxo-[5,5'] bithiazolidinylidene-4,4'-diones. *J. Heterocycl. Chem.* **53**, 989–992 (2015).
7. Le Gal, Y. *et al.* A sulfur-rich  $\pi$ -electron acceptor derived from 5,5'-bithiazolidinylidene: Charge-transfer complex vs. charge-transfer salt. *CrystEngComm* **18**, 3925–3933 (2016).
8. Filatre-Furcate, A., Higashino, T., Lorcy, D. & Mori, T. Air-stable n-channel organic field-effect transistors based on a sulfur rich  $\pi$ -electron acceptor. *J. Mater. Chem. C* **3**, 3569–3573 (2015).
9. Bielawski, C. W. & Grubbs, R. H. Increasing the initiation efficiency of Ruthenium-based ring-opening metathesis initiators: Effect of excess phosphine. *Macromolecules* **34**, 8838–8840 (2001).
10. Lowe, A. B., Hoyle, C. E. & Bowman, C. N. Thiol-yne click chemistry: A powerful and versatile methodology for materials synthesis. *J. Mater. Chem.* **20**, 4745–4750 (2010).

11. Xue, Y., Xiao, H. & Zhang, Y. Antimicrobial polymeric materials with quaternary ammonium and phosphonium salts. *Int. J. Mol. Sci.* **16**, 3626–3655 (2015).
12. Nachman, M. & Kwiatkowski, K. The effect of thermal annealing on the abrasion resistance of a segmented block copolymer urethane elastomers. *Wear* **306**, 113–118 (2013).
13. Sinturel, C., Vayer, M., Morris, M. & Hillmyer, M. Solvent Vapor Annealing of Block Polymer Thin Films. *Macromolecules* **46**, 5399–5415 (2013).
14. Yingjie, L. *et al.* Multiphase Structure of a Segmented Polyurethane: Effects of Temperature and Annealing. *Macromolecules* **25**, 7365–7372 (1992).
15. Jing, Y., Tan, X., Zhou, Z. & Shen, P. Tuning electronic and optical properties of MoS<sub>2</sub> monolayer via molecular charge transfer. *J. Mater. Chem. A* **2**, 16892–16897 (2014).
16. Refaely-Abramson, S. *et al.* Gap renormalization of molecular crystals from density-functional theory. *Phys. Rev. B - Condens. Matter Mater. Phys.* **88**, 1–5 (2013).

## CHAPTER 4

### BIDIRECTIONAL DOPING OF $\text{MoS}_2$ AND THE ROLE OF THE SUBSTRATE

#### 4.1: Introduction

Controlling the work function, the energy associated with promoting an electron from the Fermi level (electron chemical potential) to the vacuum level, is essential for enabling precise device engineering. For example, the difference in work function between the active layer and the electrode in photovoltaic devices significantly influences the open circuit voltage and charge injection/extraction processes.<sup>1-4</sup> In the context of TMDCs, efforts to modulate the work function have used mechanical strain, heterostructure fabrication, or transition metal substrates.<sup>5-10</sup> These methods typically involve high vacuum deposition or use of transition metal substrates which are cumbersome and not scalable for the fabrication of 2D materials devices. The previous two chapters have introduced chemical doping as an alternative method for modifying TMDCs, providing a solution processible platform that alleviates multi-step processing. Furthermore, non-covalent doping with polymers were shown to be reversible and is an approach that does not alter the inherent structural composition of the TMDC while maintaining mechanical integrity and presents the opportunity for spatially tuning the work function *via* patterning.<sup>11,12</sup> While previous experiments confirmed n-doping of  $\text{MoS}_2$  with TTF, the magnitude of the work function shift differed significantly from theoretical calculations. We hypothesize that this disparity is a result of doping multilayer *vs.* monolayer  $\text{MoS}_2$  – a parameter that was not controlled closely in previous experiments. We also note that our previous theoretical insights include adsorption at defect sites (sulfur vacancies) in  $\text{MoS}_2$ . These high energy vacancies provide different local electronic properties that are hypothesized to

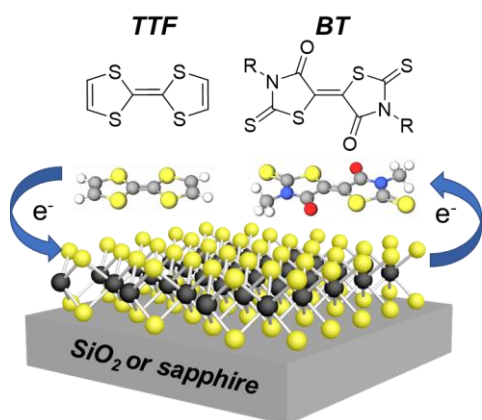


**Figure 4.1.** Cartoon depicting the scope of the experiments in this chapter using TTF and BT as dopants for single layer MoS<sub>2</sub> with control over the dielectric to probe the influence of the substrate on doping efficacy.

influence the doping efficiency at these sites. While defects influence local work function modification, we focus our investigation on the electronic impact of physisorbed dopants. Chapter 4 examines both n- and p-type dopants on the directional shift of the Fermi level of epitaxially grown single layer MoS<sub>2</sub>, highlighted in Figure 4.1. Previous theoretical insights assumed the doping processes occur in vacuum and the substrate was not considered in the overall mechanism of charge injection/extraction.

This chapter highlights the effect of the underlying substrate and a physical picture is proposed to explain this dependence in the context of experimental *vs.* theoretical results associated with the magnitude of electronic modulation arising from doping MoS<sub>2</sub>.

## 4.2: Optical Characterization of MoS<sub>2</sub>

The quality and layer thickness of MoS<sub>2</sub>, grown by chemical vapor deposition on SiO<sub>2</sub>/Si and sapphire (Al<sub>2</sub>O<sub>3</sub>), was assessed by Raman and photoluminescence spectroscopy. The Raman spectrum of MoS<sub>2</sub> contains two characteristic transitions in the low frequency region: an in-plane (E<sub>2g</sub>) and out-of-plane (A<sub>1g</sub>) stretch (refer to page 8 for visualization of these vibrations). The E<sub>2g</sub> mode is primarily affected by interlayer coupling between adjacent layers of transition metals whereas the A<sub>1g</sub> mode is particularly influenced by the presence of surface adsorbates.<sup>13</sup> Decreasing the number of MoS<sub>2</sub> layers causes the E<sub>2g</sub> peak to shift to higher energy and the A<sub>1g</sub> peak to lower energy, thus reducing

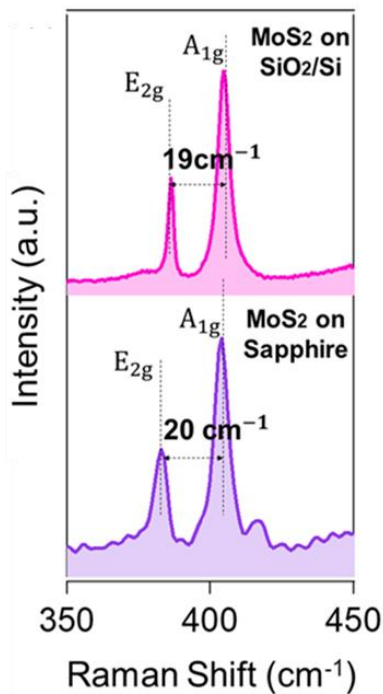


**Figure 4.2.** Raman spectrum of MoS<sub>2</sub> on (Top) SiO<sub>2</sub>/Si and (Bottom) sapphire showing the two active in-plane ( $E_{2g}$ ) and out-of-plane ( $A_{1g}$ ) stretches.

the energy difference between the two peaks. This difference can be used to determine the number of layers with single layer showing a frequency difference of  $\sim 19\text{-}20\text{ cm}^{-1}$  and increasing to  $\sim 25\text{ cm}^{-1}$  as it approaches six layers or bulk thicknesses. Figure 4.2 shows Raman spectra of single layer MoS<sub>2</sub> on SiO<sub>2</sub>/Si and sapphire; the  $E_{2g}$  peak is centered at  $385\text{ cm}^{-1}$  and the  $A_{1g}$  peak at  $405\text{ cm}^{-1}$ , a peak separation of  $\sim 20\text{ cm}^{-1}$  that agrees with literature reports of monolayer MoS<sub>2</sub>.<sup>14</sup>

Along with the Raman signatures, monolayer MoS<sub>2</sub> has characteristic photoluminescence due to quantum confinement effects. The photoluminescence (PL) spectra of MoS<sub>2</sub> on SiO<sub>2</sub>/Si and sapphire displayed a

maximum PL intensity at  $660\text{ nm}$  found in monolayer MoS<sub>2</sub> also consistent with previous reports.<sup>15,16</sup>

### 4.3: Synthesis of BT and KPFM Studies on Doped MoS<sub>2</sub>

To investigate the directional Fermi level tuning on MoS<sub>2</sub>, the organic dopants TTF (n-dopant) and BT (p-dopant) were selected for their known electron donating and accepting properties, respectively. Since only molecular interactions were considered, small molecule TTF and BT were chosen due the commercial availability or synthetic ease of access. Two BT derivatives were synthesized: methyl-BT and butyl-BT allowing additional insights into the effect of substituents. The alkyl BTs were synthesized as

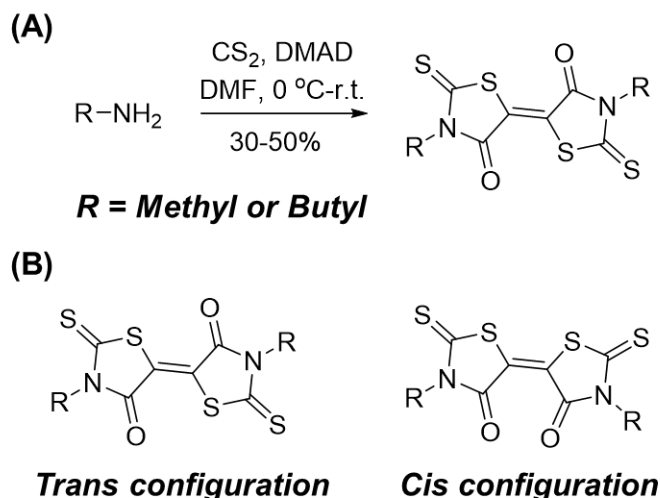


**Figure 4.3.** (A) Synthesis of BT derivative by the addition of DMAD to a stirring solution of a primary amine and carbon disulfide. (B) Two isomers (*cis* and *trans*) hypothesized to result from the reaction of methylamine with carbon disulfide and DMAD.

after crystallization, showed two products as indicated by TLC and NMR spectroscopy, behavior that did not appear when synthesizing the ethyl derivative or other functional BT derivatives. Electrospray-ionization mass spectrometry (ESI-MS) indicated only one molecular ion peak corresponding to the methyl derivative, suggesting chemical purity and, in combination with TLC, a mixture of two isomers (*E* and *Z*, Figure 4.3B). While functional BTs are primarily in the *trans* configuration, the small volume of the methyl group could give alternative nucleophilic cyclization pathways to yield a mixture of *cis* and *trans* BTs.<sup>17-21</sup>

KPFM was employed to probe the shifts in work function of MoS<sub>2</sub> before and after application of a dilute solution of either TTF or BT.<sup>22-26</sup> Each experiment consisted of scanning MoS<sub>2</sub> that was grown either on Si/SiO<sub>2</sub> or sapphire, followed by dropcasting a methanol solution of TTF or BT at a concentration of 0.005 mg/mL and rescanning the

described in Chapter 3 by introducing either methylamine or butyl amine to a solution of carbon disulfide followed by slow addition of dimethylacetylene dicarboxylate (DMAD).<sup>12,17</sup>

Synthesis of butyl-BT proceeded smoothly, affording orange crystals in yields approaching 50% (Figure 4.3A). Methyl-BT

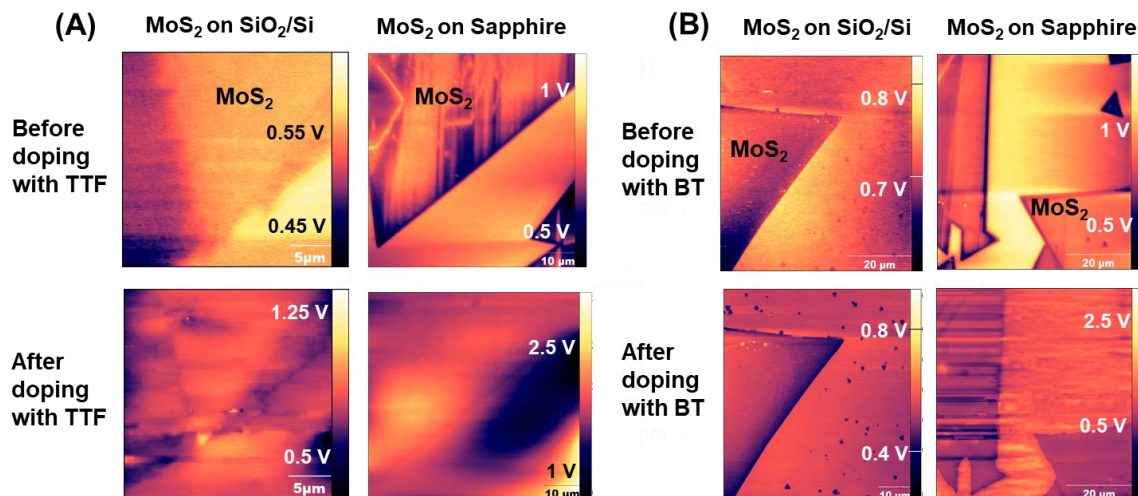


**Figure 4.4.** (A) SPC images of single layer MoS<sub>2</sub> on SiO<sub>2</sub>/Si (left) and sapphire (right) before (top) and after (bottom) coating with TTF showing a SPC increase after coating and a more significant change on sapphire vs. SiO<sub>2</sub>/Si indicating n-doping. (B) SPC images of single layer MoS<sub>2</sub> on SiO<sub>2</sub>/Si (left) and sapphire (right) before (top) and after (bottom) coating with BT showing a SPC decrease after coating and a more significant change on sapphire vs. SiO<sub>2</sub>/Si indicating p-doping.

substrate in the same area. Figure 4.4 shows the SPC images before and after drop-casting TTF and BT on a MoS<sub>2</sub> covered substrate. Figure 4.4A (left) show the surface potential images of a MoS<sub>2</sub> flake, grown on Si/SiO<sub>2</sub>, before and after addition of TTF. Data collected from the height images indicate that the step height of the flake was approximately 0.8-1.0 nm consistent with monolayer thickness. From the SPC images, a work function of 5.1-5.2 eV was measured before addition of the dopants, in accord with work function values for single layer MoS<sub>2</sub> reported in the literature.<sup>7</sup> Upon addition of TTF to MoS<sub>2</sub>, a 9-10 nm height change was observed and the SPC images display a 0.22 eV upshift in SPC, corresponding to n-doping of MoS<sub>2</sub>. Figure 4.4A (right) shows when sapphire was used as the underlying substrate, the magnitude of the SPC shift increased significantly to 1.36 eV, approaching values predicted by theory (1.64 eV).<sup>11</sup> Control experiments showed that methanol, used to cast TTF and BT dopants from solution, had very little effect on the work



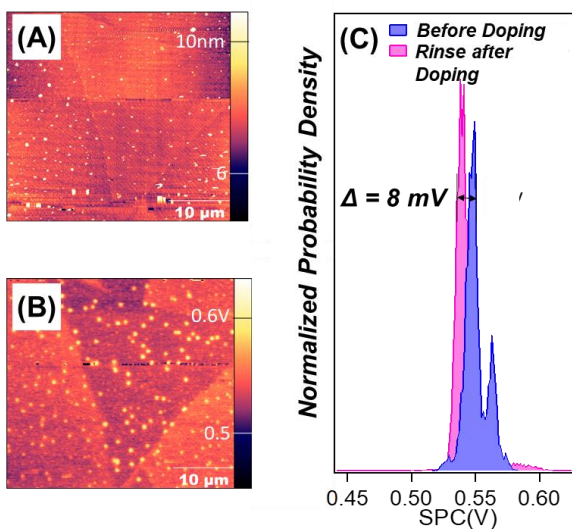


**Figure 4.5.** SPC images of single layer MoS<sub>2</sub> with (A) before doping and (B) after rinsing dopant of the substrate. (C) The resultant SPC histograms before doping and after rinsing the dopant off of the substrate with methanol showing the recovery of the original work function.

function of MoS<sub>2</sub> ensuring that the observed doping is nearly exclusively due to contact of MoS<sub>2</sub> with the organic dopants. MoS<sub>2</sub> substrates coated with BT showed a decrease in the SPC, increasing work function, indicative of p-doping. The height profiles show a clear change between the MoS<sub>2</sub> flake and the substrate before and after addition of methyl-BT to the substrate. After applying a thin coating of m-BT to the surface, MoS<sub>2</sub> on SiO<sub>2</sub>/Si showed a 0.18 eV reduction in SPC while MoS<sub>2</sub> on sapphire displayed a much greater reduction of 0.82 eV (Figure 4.4B). in SPC. Coating MoS<sub>2</sub> with a BT derivative containing *n*-butyl side chains produced lower work function shifts than the methyl derivative. The smaller work function changes from butyl BT could stem from the higher amount of insulting alkyl functionality per molecule, diminishing the electron withdrawing nature of BT or could interfere with BT adsorption onto MoS<sub>2</sub>. On both substrates, the original work function was recovered after rinsing and sonicating the doped MoS<sub>2</sub> substrates in chloroform (Figure 4.5). These KPFM experiments revealed a large dependence of work function shift on the composition of the underlying substrate. Figure 4.6A summarizes the SPC shifts of MoS<sub>2</sub> doped by TTF and BT derivatives by extracting the SPC values from the images of the scanned areas and displaying the SPC shifts as histograms. These large work function shifts

function of MoS<sub>2</sub> ensuring that the observed doping is nearly exclusively due to contact of MoS<sub>2</sub> with the organic dopants. MoS<sub>2</sub> substrates coated with BT showed a decrease in the SPC, increasing work function, indicative of p-doping. The height profiles show a clear change between the MoS<sub>2</sub> flake and the substrate before and after addition of methyl-BT to the substrate. After applying a thin coating of m-BT to the surface, MoS<sub>2</sub> on SiO<sub>2</sub>/Si showed a

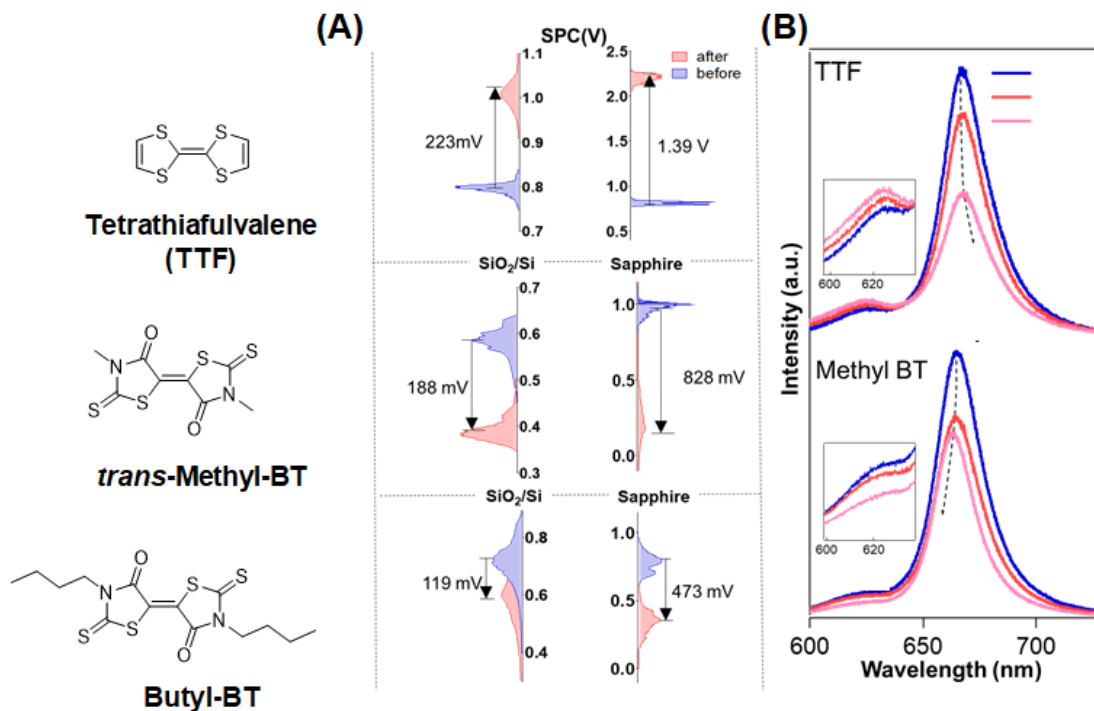


**Figure 4.6.** (A) A summary of the changes in SPC of single layer MoS<sub>2</sub> before and after doping with TTF, methyl BT, and butyl BT. The left portion shows the results of doping with TTF and BTs on SiO<sub>2</sub>/Si and the right portion shows the results from doping MoS<sub>2</sub> with TTF and BTs on sapphire. (B) PL spectra of single layer MoS<sub>2</sub> on SiO<sub>2</sub>/Si before drop-casting dilute solutions of TTF and BT and after one and two additions of TTF and BT showing wavelength shifts corresponding to n- or p-doping, insets show the MoS<sub>2</sub> B peak. The colors of the curves correspond to consecutive additions of dopants: *Blue* is uncoated MoS<sub>2</sub>, *Red* is after a single addition of dopant, and *Pink* is after a second addition of dopants.

are striking and show that the electronic properties of MoS<sub>2</sub> may be tailored directionally, over a wide range, by non-covalent adsorption of TTF and BT and selection of different substrates.

To further confirm TTF and BT doping of MoS<sub>2</sub>, photoluminescence (PL) spectroscopy was performed on monolayer MoS<sub>2</sub> before and after coating with these organic dopants. The two excitonic peaks in the PL spectra are a result from spin-orbit splitting of the valance band, with the primary PL peak being most sensitive to layer number and surface adsorbates. Upon coating with TTF, the intensity of the A-peak (666

nm) decreased and shifted to longer wavelengths (4 nm), indicating n-doping, while the B-peak (623 nm) intensity increased with no shift in wavelength (Figure 4.6B, top).<sup>7,16</sup> For BT doping, the A- and B-peak intensities both decreased and the A peak shifted to shorter wavelengths (5 nm), while the B-peaks did not shift, indicating p-doping (Figure 4.6B, bottom). The PL shifts in the A-peak from doping are caused from the increase or decrease of the trion (bound exciton and electron) component after the addition or depletion of charge, making it sensitive to surface adsorption.<sup>27</sup> The wavelength shift for BT doping is consistent with literature reports on p-doping of MoS<sub>2</sub>; however, the decrease in PL intensity is not. This PL decrease may result from overlapping BT absorption with MoS<sub>2</sub> photoexcitation, thereby not all photons are being absorbed/reemitted by MoS<sub>2</sub> but partitioned between MoS<sub>2</sub> and BT. For these experiments, it is noteworthy that DFT simulations of carrier doping in pristine (defect-free) MoS<sub>2</sub> predict an n-type doping for *both* TTF and BT molecules, contrary to the experimental observations reported here. However, recent unpublished x-ray photoelectron spectroscopy (XPS) measurements by Naveh and co-workers on WSe<sub>2</sub> have shown that pendent groups that are anticipated to be n-dopants may impart a Fermi-level *lowering*, consistent with p-type doping. This counterintuitive effect appears to be correlated with chalcogen vacancy defects in the TMDC, although the mechanism of this effect is yet clear. Nevertheless, our results indicate yet another route to Fermi-level tuning *via* complementary surface functionalization of MoS<sub>2</sub>.

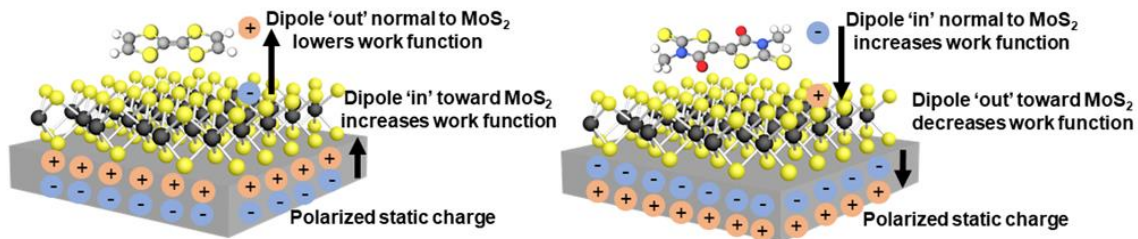


**Figure 4.7.** Physical picture of dipole and induced static polarization for the work function shift in MoS<sub>2</sub> after doping with TTF. Left: TTF donates electrons through charge transfer to MoS<sub>2</sub>. Right: BT accepts electrons from MoS<sub>2</sub>. The transfer of electrons gives rise to dipoles between TTF and MoS<sub>2</sub> and corresponding induced dipoles from static charge at the dielectric/semiconductor interface. This polarized static charge effectively screens the measured work function of MoS<sub>2</sub> and the screening strength will vary with dielectric constant of the underlying substrate.

#### 4.4: Mechanism of Substrate Influence on Doping MoS<sub>2</sub>

Figure 4.7 presents a hypothesis for the observed work function shifts of MoS<sub>2</sub> as it relates to the substrate properties. For the sake of simplicity, only the case for TTF is discussed but the concept is easily extended to explain the effects observed for BT doping. Upon coating MoS<sub>2</sub> with TTF, electron transfer between the TTF and MoS<sub>2</sub> generates a dipole that is directed outward (normal) from MoS<sub>2</sub> (Figure 4.7, left); where the orientation of the dipole reflects a decrease in work function or n-doping for MoS<sub>2</sub>.<sup>28</sup> The dipoles generated by contact of the 2D material and organic dopant induce a polarized static charge, forming opposing dipoles at the substrate/semiconductor interface, effectively screening the measured surface potential. The work function change due to interfacial dipoles (e.g., the magnitude of dipole screening) is given by  $\Delta WF = \frac{\sigma_d}{\epsilon_0 \epsilon}$ , where  $\sigma_d$  is the dipole moment area density,  $\epsilon_0$  is the permittivity of vacuum, and  $\epsilon$  is the relative permittivity of the dielectric. Increasing the dielectric constant reduces the magnitude of this screening effect, leading to a smaller work function offset, that is measured by KPFM, and increasing the work function shift in the 2D material. Since sapphire has a dielectric constant 3 to 4 times

larger than that of SiO<sub>2</sub>, charge screening at the surface is much smaller for sapphire than for SiO<sub>2</sub>, increasing the change in the measured work function.<sup>29,30</sup> This combined effect of dipoles induced by charge transfer and oppositely directed static polarization have a profound impact in a device context. For example, simply by changing the dielectric that the semiconductor is grown on, the effect of dopants on the semiconductor change dramatically and opens up a toolbox of parameters to optimize device architecture to achieve high-performance 2D material devices.

#### **4.5: Conclusions**

In conclusion, a tunable, “bidirectional” work function modulation of MoS<sub>2</sub> by non-covalently doping the semiconductor with the organic dopants TTF and two BT derivatives was shown. Spectroscopic and KPFM measurements provide compelling evidence for n-doping of MoS<sub>2</sub> by TTF and p-doping of MoS<sub>2</sub> by BT moieties. Notably, p-doping of MoS<sub>2</sub> with organic adsorbates while rarely reported, would be useful in the fabrication of p-n junctions on TMDCs. Using substrates with different dielectric properties significantly altered the magnitude of work function change after doping. For TTF doping, work function shifts increased from 0.22 eV to 1.39 eV when changing from SiO<sub>2</sub>/Si to sapphire. These large differences in work function shifts are hypothesized to arise from the formation of induced dipoles and static polarization at the semiconductor/substrate interface. The ability to “bidirectionally” tune MoS<sub>2</sub> work function with different underlying substrates allows for production of electronically tailored TMDCs, which are needed for devices such as FETs and diodes. Moreover, such non-covalent doping by physisorption is scalable,

reversible, and non-damaging to the semiconductor, making its use feasible for the development of next-generation TMDC devices.

## 4.1 References

1. Zhang, R. *et al.* Authigenic buffer layer: Tuning surface work function in all polymer blend solar cells. *Colloids Surfaces A Physicochem. Eng. Asp.* **535**, 149–156 (2017).
2. Melitz, W., Shen, J., Kummel, A. C. & Lee, S. Kelvin probe force microscopy and its application. *Surf. Sci. Rep.* **66**, 1–27 (2011).
3. Zhang, H. *et al.* Ba<sup>2+</sup> Doped CH<sub>3</sub>NH<sub>3</sub>PbI<sub>3</sub> to Tune the Energy State and Improve the Performance of Perovskite Solar Cells. *Electrochem. Acta* **254**, 165–171 (2017).
4. Mei, Y. *et al.* Interface engineering to enhance charge injection and transport in solution-deposited organic transistors. *Org. Electron. physics, Mater. Appl.* **50**, 100–105 (2017).
5. Lanzillo, N. A., Simbeck, A. J. & Nayak, S. K. Strain engineering the work function in monolayer metal dichalcogenides. *J. Phys. Condens. Matter* **27**, (2015).
6. Li, F. *et al.* Layer Dependence and Light Tuning Surface Potential of 2D MoS<sub>2</sub> on Various Substrates. *Small* **13**, 1–8 (2017).
7. Li, Y. *et al.* Photoluminescence of monolayer MoS<sub>2</sub> on LaAlO<sub>3</sub> and SrTiO<sub>3</sub> substrates. *Nanoscale* **6**, 15248–15254 (2014).
8. Zhang, Q. *et al.* Bandgap renormalization and work function tuning in MoSe<sub>2</sub>/hBN/Ru(0001) heterostructures. *Nat. Commun.* **7**, 1–7 (2016).
9. Sandonas, L. M., Gutierrez, R., Pecchia, A., Seifert, G. & Cuniberti, G. Tuning quantum electron and phonon transport in two-dimensional materials by strain engineering: A Green's function based study. *Phys. Chem. Chem. Phys.* **19**, 1487–1495 (2017).
10. Baik, S. S., Im, S. & Choi, H. J. Work Function Tuning in Two-Dimensional MoS<sub>2</sub> Field-Effect-Transistors with Graphene and Titanium Source-Drain Contacts. *Sci. Rep.* **7**, 1–8 (2017).
11. Selhorst, R. C. *et al.* Tetrathiafulvalene-containing polymers for simultaneous non-covalent modification and electronic modulation of MoS<sub>2</sub> nanomaterials. *Chem. Sci.* **7**, 4698–4705 (2016).
12. Selhorst, R., Wang, P., Barnes, M. & Emrick, T. Bithiazolidinylidene polymers: Synthesis and electronic interactions with transition metal dichalcogenides. *Chem. Sci.* **9**, 5047–5051 (2018).

13. Lee, C. *et al.* Anomalous Lattice Vibrations of Single- and Few-Layer MoS<sub>2</sub>. *ACS Nano* **4**, 2695–2700 (2010).
14. Wang, H. *et al.* Integrated circuits based on bilayer MoS<sub>2</sub> transistors. *Nano Lett.* **12**, 4674–4680 (2012).
15. Jariwala, D., Sangwan, V. K., Lauhon, L. J., Marks, T. J. & Hersam, M. C. Emerging device applications for semiconducting two-dimensional transition metal dichalcogenides. *ACS Nano* **8**, 1102–1120 (2014).
16. Mouri, S., Miyauchi, Y. & Matsuda, K. Tunable photoluminescence of monolayer MoS<sub>2</sub> via chemical doping. *Nano Lett.* **13**, 5944–5948 (2013).
17. Nasiri, F., Zolali, A. & Asadbegi, S. Solvent-free One-pot Synthesis of 2,2'-dithioxo-[5,5'] bithiazolidinylidene-4,4'-diones. *J. Heterocycl. Chem.* **53**, 989–992 (2015).
18. Nagase, H. Studies on Fungicides. XXII. Reaction of Dimethyl Acetylenedicarboxylate with Dithiocarbamates, Thiocarbamates, Thiosemicarbazides and Thiosemicarbazones. *Chem. Pharm. Bull.* **21**, 279–286 (1972).
19. Nagase, H. Studies on Fugicides. XXV. Addition Reaction of Dithiocarbamates to Fumaronitrile, Bis(alkylthio)maleonitrile, 2,3,-Dicyano-5,6-dihydro-1,4-dithiin and 4,5-Dicyano-2-oxo-1,4-dithiol. *Chem. Pharm. Bull.* **22**, 505–513 (1973).
20. Le Gal, Y. *et al.* A sulfur-rich  $\pi$ -electron acceptor derived from 5,5'-bithiazolidinylidene: Charge-transfer complex *vs.* charge-transfer salt. *CrystEngComm* **18**, 3925–3933 (2016).
21. Filatre-Furcate, A., Higashino, T., Lorcy, D. & Mori, T. Air-stable n-channel organic field-effect transistors based on a sulfur rich  $\pi$ -electron acceptor. *J. Mater. Chem. C* **3**, 3569–3573 (2015).
22. Baghgar, M. *et al.* Morphology-dependent electronic properties in cross-linked (P3HT- b -P3MT) block copolymer nanostructures. *ACS Nano* **8**, 8344–8349 (2014).
23. Aghgar, M. & Barnes, M. D. Work Function Modification in P3HT H/J Aggregate Nanostructures Revealed by Kelvin Probe Force Microscopy and Photoluminescence Imaging. *ACS Nano* **9**, 7105–7112 (2015).
24. Wang, P. & Barnes, M. D. Disentangling 'bright' and 'dark' Interactions in Ordered Assemblies of Organic Semiconductors. *Nano Lett.* **17**, 6949–6953 (2017).



25. Palermo, V., Palma, M. & Samori, P. Electronic characterization of organic thin films by Kelvin probe force microscopy. *Adv. Mater.* **18**, 145–164 (2006).
26. Liscio, A. *et al.* Local surface potential of  $\pi$ -conjugated nanostructures by Kelvin Probe Force microscopy: Effect of the sampling depth. *Small* **7**, 634–639 (2011).
27. Mak, K. F. *et al.* Observation of tightly bound trions in monolayer MoS<sub>2</sub>. *Nat. Mater.* **12**, 207–211 (2012).
28. Jeong, K. S., Deng, Z., Keuleyan, S., Liu, H. & Guyot-Sionnest, P. Air-stable n-doped colloidal HgS quantum dots. *J. Phys. Chem. Lett.* **5**, 1139–1143 (2014).
29. Krupka, J., Derzakowski, K., Tobar, M., Hartnett, J. & Geyer, R. G. Complex permittivity of some ultra-low loss dielectric crystals at cryogenic temperatures. *Meas. Sci. Technol.* **10**, 387–392 (1999).
30. Rong, L. *et al.* Impact of defects on local optical dielectric properties of Si/SiO<sub>2</sub> interfaces by layered capacitor modeling. *Appl. Phys. A Mater. Sci. Process.* **122**, 1–8 (2016).

## CHAPTER 5

### ZWITTERIONIC PHOTORESISTS FOR SIMULTANEOUS PATTERNING AND DOPING OF GRAPHENE

#### 5.1 Introduction

Chapter 5 builds upon the ideas highlighted in the previous chapters and introduces the concept of spatially tailored electronics on 2D materials. This chapter broadens the scope of 2D materials by utilizing graphene instead of TMDCs due to the ease of access and understanding of single layer graphene. While much progress has been made in the fabrication of 2D-material based devices, the ability to exercise precise spatial control over majority carrier type and concentration remains an outstanding challenge that must be overcome for engineering integrated circuits. Specifically, Chapter 5 details the design a hybrid polymer–graphene platform for carrier doping of graphene *via* noncovalent adsorption of functional polymer thin films. While the previous chapters used conjugated organochalcogens as functionality for non-covalent physisorption, this chapter demonstrates the utility of non-conjugated zwitterionic moieties as the handle for doping graphene. Furthermore, scalable approaches for patterning these polymer films *via* electron-beam lithography are presented, achieving precise spatial control over carrier doping for fabrication of lateral homojunctions. Our approach preserves all of the desirable structural and electronic properties of graphene, while exclusively modifying its surface potential, and offers a facile route toward lithographic doping of graphene-based devices.

Graphene is a special case of a zero-bandgap 2D semiconductor that poses challenges for nanoscale electronics while simultaneously affording scientific and technological opportunities. Numerous modern electronic devices utilize semiconductors as their basic building blocks and cannot be fabricated with gapless graphene because of issues related to the metallic behavior of the material. Nonetheless, the unique electronic properties of graphene allow for emerging device architectures beyond traditional semiconductor electronics.<sup>1</sup> For example, analogous to wave-guiding in optics, p–n junctions in graphene can guide ballistic carrier currents;<sup>2</sup> this functionality exploits the unusual angle-dependent conductance of graphene junctions to achieve phenomena such as electron focusing and collimation.<sup>3–6</sup> Graphene p–n junctions also display unusual light-matter interactions including the photo-thermoelectric effect<sup>7</sup> and self-driven, bias-free photocurrents.<sup>8</sup> Thus, there is significant interest in developing precise and scalable methods for area-selective carrier doping of graphene for realizing novel 2D optoelectronic devices.

*Chapter 5 presents a hybrid graphene–functional polymer (hard–soft materials) platform that simultaneously addresses the dual issues of carrier doping and scalable device processing.* This chapter aims to exploit the extreme sensitivity of graphene to its immediate environment and engineer suitable zwitterionic polymers that induce appreciable surface potential shifts in graphene *via* adsorbed interfacial dipoles. A key feature of these polymers is that the zwitterionic moieties are incorporated as pendent groups attached to poly(methyl methacrylate) (PMMA) backbones, rendering them amenable to patterning by electron-beam lithography as depicted in Figure 5.1. We note

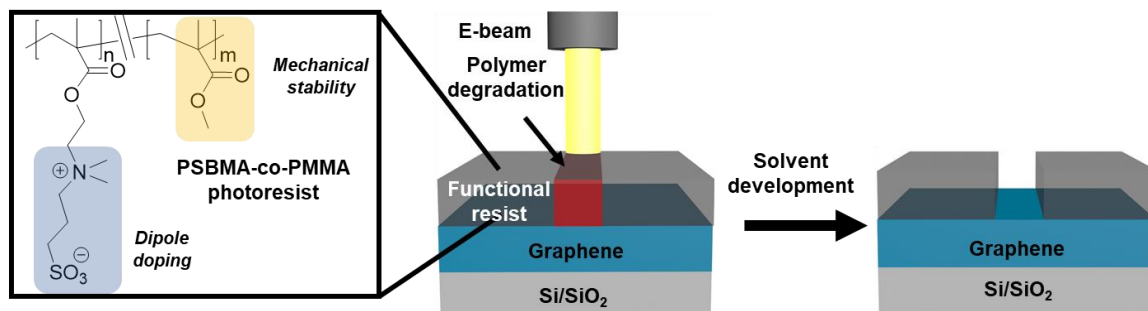


**Figure 5.1.** Outline of the implementation of the polymer zwitterion PSBMA-co-PMMA as a functional photoresist that is used to simultaneously pattern and dope graphene.

that other molecules<sup>9</sup> and polymers (*e.g.*, poly(4-vinylpyridine) and poly(vinyl chloride))<sup>10</sup> have been utilized in the past for doping graphene, with complementary doping achieved using rubber-stamping of bis(trifluoromethanesulfonyl) and poly-(ethyleneimine).<sup>11</sup> The key innovation in this work is the development of lithographically processed polymer dopant that can be directly patterned on the target undoped material for achieving carrier density control at high spatial resolution.

## 5.2 Synthesis of Polymer Zwitterions

Noncovalent adsorption of dopant moieties is an attractive approach for modulating the electronic properties of 2D materials while preserving their overall structural integrity and purity, and therefore provide significant advantages over other destructive doping methods.<sup>12</sup> Instead of chalcogen rich moieties as physisorbing moieties, methacrylate polymers containing zwitterionic sulfobetaine (SB) pendent groups for contact with graphene are employed. Sulfobetaine is composed of a sulfonate anion and ammonium cation separated by an aliphatic chain generating an intrinsic dipole moment of 15.2 D, as estimated from density functional theory calculations. This electrostatic dipole endows polymer zwitterions with aqueous/salt water solubility enabling orthogonal processability,

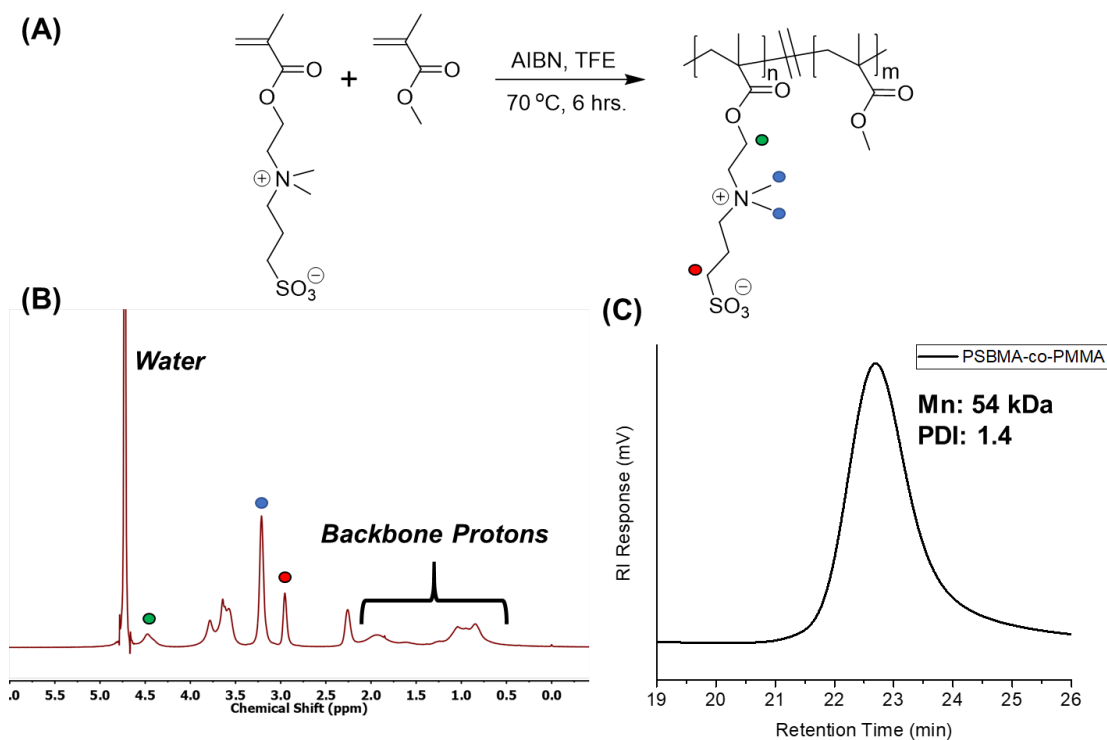


**Figure 5.2.** (A) Scheme showing the synthesis of PSBMA-*co*-PMMA by conventional free-radical polymerization. (B)  $^1\text{H}$  NMR spectra of PSBMA-*co*-PMMA confirming the successful synthesis of the polymer, specifically noting the sulfobetaine resonances indicated by the colored ovals. (C) Gel Permeation Chromatography in trifluoroethanol of PSBMA-*co*-PMMA showing high molecular weight and a monomodal molecular weight distribution.

an important factor in the design of photoresist technology. Prior studies by Emrick and coworkers showed that PSBMA thin films significantly reduced the work function of ITO, Au, Al and graphene (by 1.09, 1.52, 0.36, and 1.64 eV, respectively),<sup>13</sup> which motivates the use of these polymers as efficient dopants for graphene devices. Moreover, the zwitterion concentration is important to control for adjusting the PSBMA-induced work-function shift and therefore is a strong motivator for implementing copolymers rather than homopolymers of PSBMA.

PSBMA-*co*-PMMA was synthesized by conventional free radical polymerization, initiated by 2,2'-azobisisobutyronitrile (AIBN), in trifluoroethanol (TFE), as shown in

Figure 5.2A. Monomer conversion, monitored by  $^1\text{H}$  NMR spectroscopy, after 6 h at 70 °C approached 60–70% and monomer incorporation matched that of the feed ratio (Figure 5.2B). The molecular weight of the polymer was 54 kDa, as estimated by gel permeation chromatography (GPC) in TFE, and the polymer dispersity was  $\sim 1.4$  (Figure 5.2C). The brevity of this polymerization is aided by the strong polar solvent, allowing full conversion and high molecular weights in hours. The solution processability of the polymer is pertinent to the design and implementation of resists for lithographic patterning. Sulfobetaine imparts solubility to the PMMA copolymer in water, salt water, TFE, and polar aprotic solvents such as N-methyl pyrrolidone (NMP). This advantageous solubility, coupled with high molecular weight, makes this polymer an excellent candidate for lithographic processing on substrates.

### 5.3 PSBMA-co-PMMA Photoresists: Optimization and Spectroscopy

The synthesized copolymer with a 1:1 ratio of SBMA/MMA ratio was optimized as a solution-processable positive tone resist with respect to exposure dosage (30 keV e-beam) and development conditions to achieve patterned functional films of 80 nm

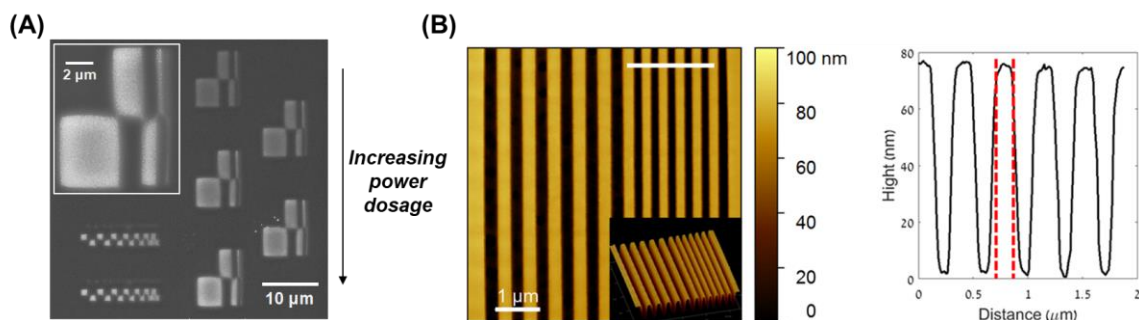


**Figure 5.3.** (A) Scanning Electron Micrograph of a PSBMA-co-PMMA polymer film after e-beam lithography and development showing the dependence of resolution on electron beam power. (B) Atomic Force Micrograph of line patterns after development with the corresponding height profile showing the high fidelity with which these patterns can be fabricated.

thickness and 200 nm line width and pitch (Figure 5.3A). Figure 5.3B displays an atomic force micrograph of a patterned resist showing sharp topography maps of 10  $\mu\text{m}$  long lines of 200–300 nm width and pitch. The level of spatial resolution achieved with our resist is comparable to that of commercial PMMA resists when processed with the same beam

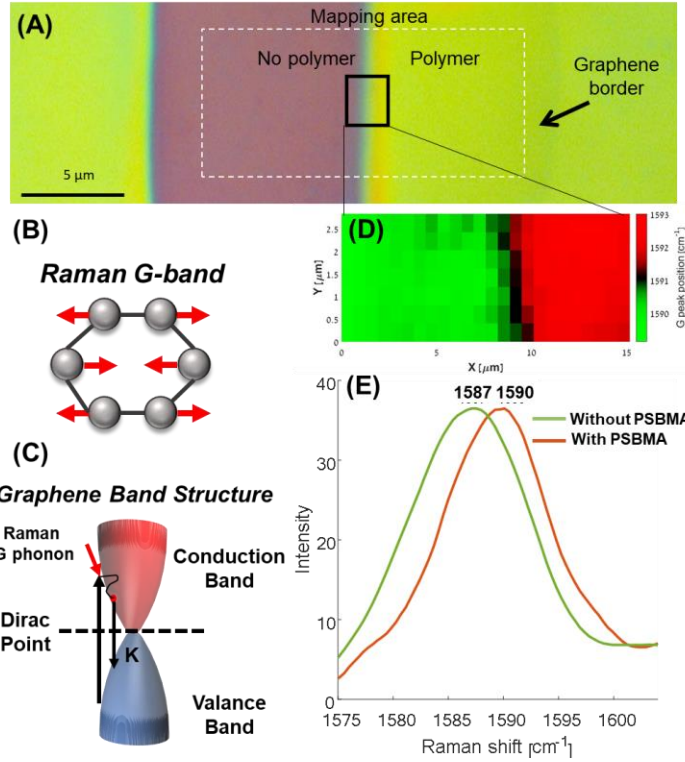


**Figure 5.4.** (A) Optical micrograph of single layer CVD graphene coated with PSBMA-co-PMMA in which half of the polymer film was developed such that the left side is bare graphene and the right side is polymer coated. (B) Visualization of the vibration responsible for the Raman G-band – the probe for molecular doping. (C) Band diagram of graphene showing the appearance of the G-band vibration by a Raman active optical phonon relaxation. (D) Raman mapping of the border between bare and polymer-coated graphene and the corresponding spectra (E) showing the Raman upshift due to PSBMA doping of graphene.

energy and resist thickness; the key difference is that the PSBMA-co-PMMA photoresist is a functional resist that can be used to pattern and dope graphene.

The doping effect of the PSBMA-co-PMMA photoresist on graphene was studied by Raman spectroscopy. Figure 5.4A displays an example of the polymer photoresist applied by spin coating to a 40  $\mu\text{m}$   $\times$  10  $\mu\text{m}$  monolayer of CVD-grown graphene (on Si/SiO<sub>2</sub>), patterned by e-beam writing, then developed with solvent to

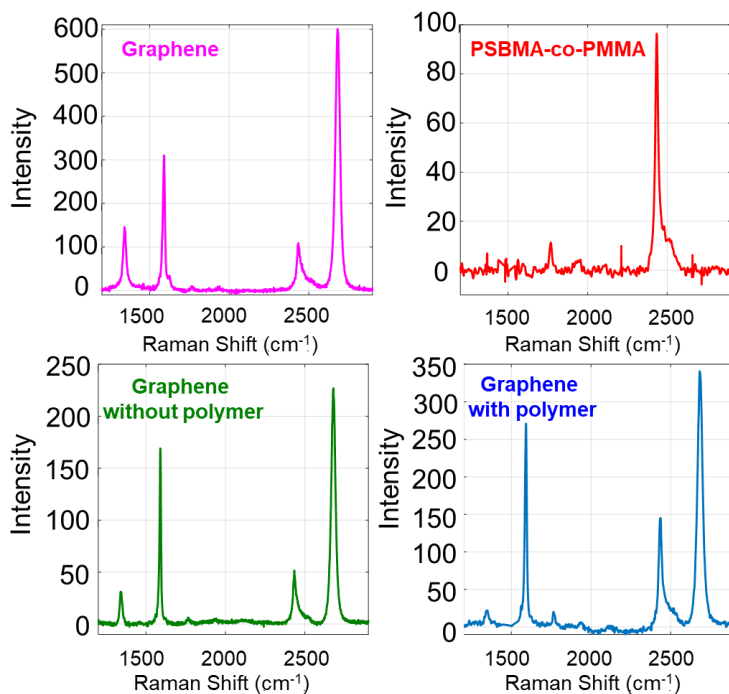


**Figure 5.5.** Raman spectra of bare graphene and PSBMA-co-PMMA before (Top) and after (Bottom) coating the polymer on the graphene bar showing that there is no interference of the polymer with the G-band of graphene and that successful n-doping is taking place after polymer coating.

layers, doping level, and confinement (Visually shown in Figure 5.4B).<sup>14,15</sup> The Raman signature is due to the activity of the optical phonon which lowers the energy of an absorbed photon to a virtual state in the graphene conduction band followed by relaxation to the ground state, shown in Figure 5.4C. Figure 5.4D,E display a Raman map of the entire graphene monolayer as well as individual line scans taken along the length of the monolayer from which we observe a clear shift in the G-peak frequency from  $1589\text{ cm}^{-1}$  in the uncoated region to  $1593\text{ cm}^{-1}$  in the polymer-coated part; the frequency shift clearly results from the resist pattern. To ensure that the Raman signatures were not artifacts from the polymer coating, control Raman experiments on only the polymer film and bare graphene were recorded and are shown in Figure 5.5. The Raman shifts observed for the

coat only the right half of the flake. After coating, local chemical potential shifts of graphene in the polymer-coated and bare regions were revealed by mapping the optical phonon (G-mode) energy *via* Raman spectroscopy. The Raman G peak of graphene arises from

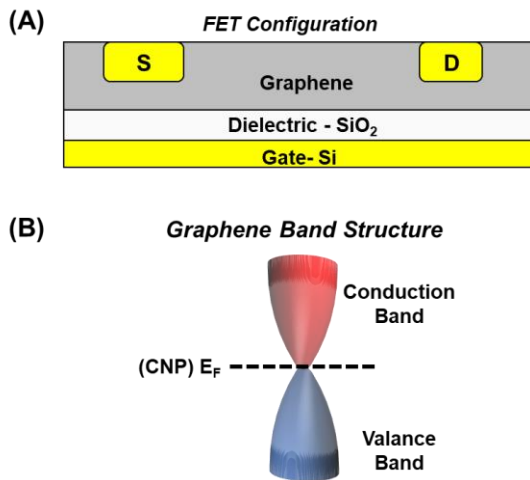
bond stretching of all pairs of  $\text{sp}^2$  atoms and is a signature of the number and quality of



polymer coated graphene correspond to changes in the optical phonon energy which is sensitive to a change in carrier concentration.<sup>16</sup> However, these doping induced shifts do not shed light on the carrier type; to extract information on both charge carrier type and concentration field-effect transistor transport measurements are required.

### 5.4 Graphene Field-Effect Transistors and Doping

To better understand the operation of FETs and the device characteristics pertinent to doped graphene, an introduction with examples is first discussed. Transistors are three electrode devices consisting of a source, drain, and gate electrode, with the source and drain directly measuring the current across the contacting semiconductor and the gate electrode



providing a bias acting through a dielectric to control the flow of charge through the semiconducting channel (Figure 5.6A).<sup>17</sup> Due to the gapless band structure of graphene, there is a seamless transition between n-type conduction, where the Fermi energy lies in the conduction band and p-type conduction,

**Figure 5.6.** (A) Diagram of a field-effect transistor, specifically the setup used for the device studies in the chapter. (B) Graphene band structure showing the charge neutrality point at the Dirac point in pristine undoped graphene, however, the position changes depending on the type of dopants introduced onto graphene.

where the Fermi energy lies in the valance band. These two modes of operation are separated by point of zero conduction where the conduction band and valance band meet,

called the Dirac point (Figure 5.6B). Graphene FETs typically display ambipolar conduction behavior due to this transition and current can be measured at gate voltages

above and below the charge neutrality point (CNP) which is identified as the current minima in a plot of drain current vs. gate voltage.<sup>18</sup> The CNP is also a measure of the Fermi energy and can be used to identify directional doping behavior. If doped, the current will be asymmetric, with higher currents measured below the CNP for p-doping or above the CNP for n-doping. In the case of p-n junction formation, symmetric high currents are observed above and below the CNP as both n-type and p-type conduction characteristics are imparted in the semiconductor.<sup>19</sup> For the PSBMA-co-PMMA/graphene system, metrics such as on/off currents, CNP, and charge carrier concentration are used to characterize the level of doping and conduction behavior of the fabricated FETs.

Measurements of gate-resolved conductivity of graphene FETs provide precise values of the average carrier density induced by the functional polymer in the graphene monolayer. Specifically, the average carrier density,  $\bar{n}$ , is given by  $\bar{n} = C_g[V_g - V_{\text{CNP}}]/e$ , where  $C_g$  is the gate capacitance and  $V_g$  and  $V_{\text{CNP}}$  are the gate and charge neutrality point voltages, respectively. A series of five FETs were prepared on a single-monolayer of CVD graphene (Figure 5.7A).<sup>20</sup> Two devices were unexposed by lithography and therefore remained coated with the functional polymer dopant, two devices were exposed and developed to measure transport in the bare graphene region, and one device spanned the functionalized and bare graphene regions effectively measuring transport across a homojunction. It is noteworthy that the graphene was deposited on p-type Si/SiO<sub>2</sub> therefore, bare graphene devices should intrinsically display p-type conduction characteristics. To confirm the absence of unintentional, process-related doping effects, control experiments were performed on bare and PMMA-coated graphene devices (Figure

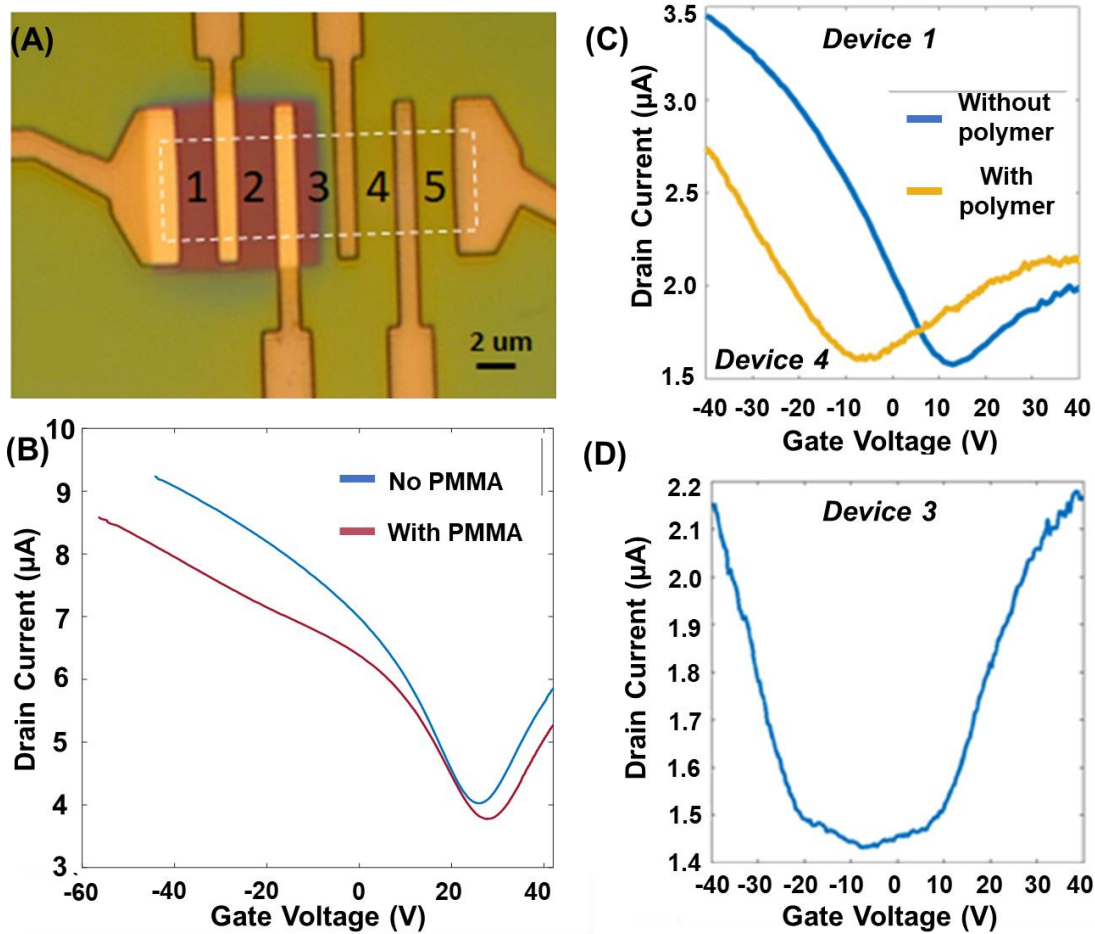


**Figure 5.7.** (A) Optical micrograph of five graphene FETs either bare graphene (1,2), PSBMA-*co*-PMMA coated graphene (3,4) or half-coated (3). (B) Control FET device characteristics showing similar behavior before and after coated with PMMA. (C) Transfer curves for devices 1 and 4 showing a drastic shift in the CNP towards negative gate voltages, indicating n-doping. (D) Transfer curve of device 3 showing high currents above and below the CNP indicative of a p-n junction.

5.7B). In comparing the charge neutrality voltage, we observe a shift of  $\sim 20$  V (over 285 nm of Si/SiO<sub>2</sub>) between the coated and uncoated devices (Figure 5.7C). This shift in the charge neutrality point of graphene induced by the PSBMA-*co*-PMMA resist corresponds to a doping level of  $1.35 \times 10^{12} \text{ cm}^{-2}$  and a Fermi-level shift determined by  $\phi = \sin(V_g - V_{\text{CNP}}) \hbar v_F \pi |\bar{n}|$  where  $v_F = 106 \text{ m/s}$  is the Fermi velocity of carriers in graphene and  $\bar{n}$  is the effective doping level.<sup>21</sup> Furthermore, comparing the device characteristics of the

bare FETs versus the polymer-coated ones reveals two important conclusions: (i) this surface functionalization method produces uniform carrier doping over the polymer-coated regions and (ii) the field-effect mobility of charge carriers is barely affected upon surface functionalization, which indicates negligible introduction of charged impurities from the polymer film.

The ability of PSBMA-*co*-MMA to produce lateral graphene homojunctions is seen in the device characteristics in Figure 5.7D that show the distinct I–V signature of a p–n junction. We attribute the formation of this p–n homojunction to the potential shift induced within the polymer-coated graphene region by the SB molecular dipole moment. From basic electrostatics,<sup>22</sup> the shift in surface potential of polymer coated graphene is  $\Delta\phi = -\epsilon \epsilon_q D_{\text{0eff}}$ , where  $D = \rho \mu_{\perp}$  is the dipole moment per unit area of polymer/graphene interface,  $\rho$  is the area density of dipoles at the polymer/graphene interface,  $\mu_{\perp}$  is the component of the zwitterion molecular dipole moment normal to the graphene sheet, and  $\epsilon_{\text{eff}}$  is the effective dielectric constant of the embedding medium (SiO<sub>2</sub> and polymer) defined by  $\epsilon_{\text{eff}} = [\epsilon_{\text{SiO}_2} + \epsilon_{\text{polymer}}]/2$ . Specific to our case, the functional resist contains 0.16 M units of zwitterions corresponding to an area density of  $\rho \approx 2.1 \times 10^{13} \text{ cm}^{-2}$  at the polymer–graphene interface. With the measured Fermi level shift of  $\Delta\phi \approx 0.2 \text{ eV}$  and an effective dielectric constant of  $\epsilon_{\text{eff}} \approx 4$ , we arrive at an estimate of  $\mu_{\perp} \approx 10D$  for the molecular dipole moment of adsorbed SB moieties.

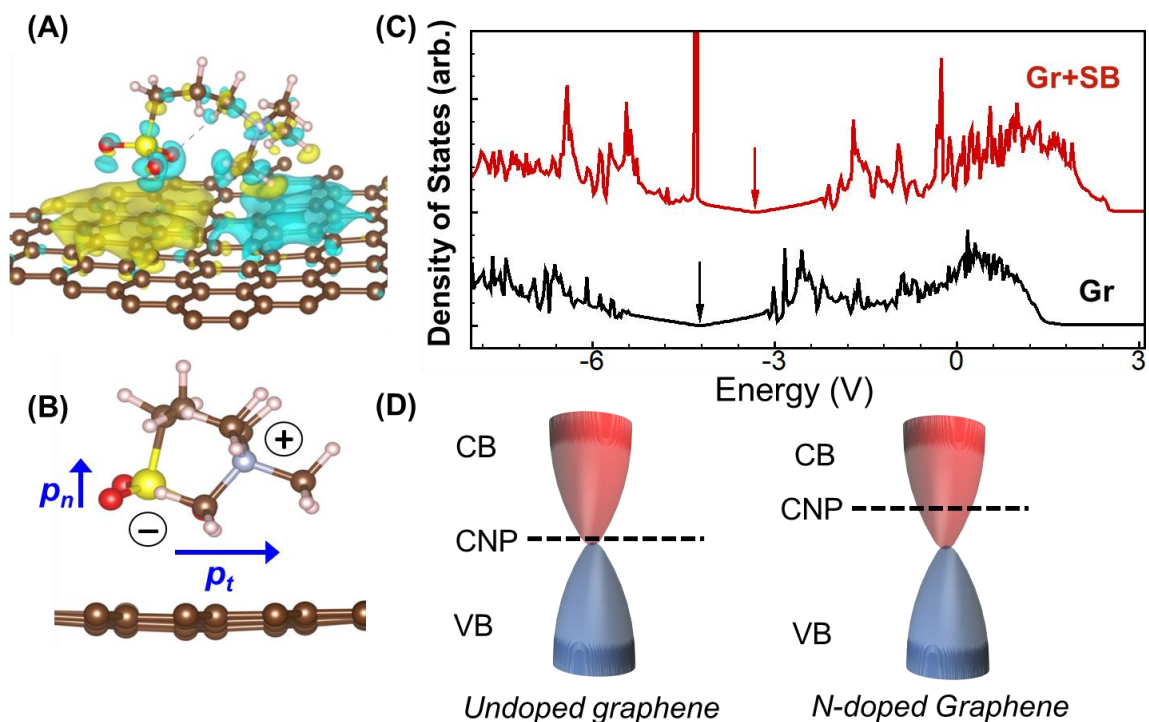


**Figure 5.8.** (A) DFT calculation showing the equilibrium geometry of a sulfobetaine moiety physisorbed to a graphene lattice showing charge accumulation/depletion due to the charged atoms in the zwitterion. (B) side profile of a sulfobetaine moiety showing the in-plane and out-of-plane components of the dipole moment. (C) Density of states plot indicating an upshift in the Fermi energy after doping toward the conduction band of graphene, visually depicted in (D).

### 5.5 Theoretical Insights on the Zwitterion/Graphene Interface

To further understand the physical and electronic interactions between the polymer thin film and graphene, first-principles DFT calculations using the Vienna *Ab Initio* Simulation Package (VASP) were employed.<sup>23,24</sup> While it is impractical to model the adsorbed polymer chains in their entirety, important insights can be gained by considering the key components of the system, namely, the SB pendent group and the graphene sheet. The computational model consists of a  $6 \times 6$  graphene supercell on which SB pendent groups are adsorbed. As seen from Figure 5.8A,B, the SB moiety adsorbs in a flat configuration-interacting with the graphene sheet *via* the terminal sulfate and methyl

groups-with a calculated binding energy of 0.92 eV, indicative of a stable polymer/graphene interface. Figure 5.8A displays the transfer of charge between the SB pendent group and the graphene sheet; as expected, the oppositely charged ends of the zwitterionic moiety induce corresponding regions of electron accumulation and depletion within the graphene monolayer. The charge redistribution within the graphene monolayer is fairly localized, extending a few unit cells beyond the adsorbed SB group, and is not long-range. On average though, the induced positive and negative charges within the graphene sheet cancel each other, and unlike our previous work on TTF pendent groups adsorbed on MoS<sub>2</sub>,<sup>25</sup> there is no net charge transfer between graphene and SB. The bonding mechanism between the SB pendent group and the graphene sheet is thus primarily by noncovalent and localized charge-transfer interactions.

Figure 5.8B also shows that the sulfur and nitrogen atoms are at slightly different heights from the graphene sheet in the adsorbed configuration. This surface dipole may be further decomposed into components transverse and normal to the graphene sheet. The transverse components of the dipoles of randomly adsorbed SB pendent groups will, on average, cancel out and contribute only to short-range scattering mechanisms; the normal components are, however, additive leading to a net dipole moment normal to the graphene sheet ( $\mu_{\perp} = 4.7D$ ). This surface dipole induces a shift in the charge-neutrality point of the graphene sheet toward the vacuum level as seen from the density of states plot in Figure 5.8C. Correspondingly, the planar averaged DFT local potential shows a reduced work function of the graphene sheet on the side with the adsorbed SB moiety ( $\phi = 3.32$  eV) relative to the side without the surface dipole (equivalently, the bare graphene sheet;  $\phi =$

4.24 eV). While the DFT calculation does not take into account dielectric screening from the substrate and polymer film, as a first approximation the work function shift,  $\Delta\phi_{\text{DFT}} = 0.92$  eV, may be renormalized simply by the effective dielectric constant of the embedding medium,  $\epsilon_{\text{eff}} \approx 4$ , which leads to a predicted work function shift of  $\Delta\phi_{\text{predicted}} = 0.23$  eV. This excellent quantitative agreement between theory and experiment bolsters the view of purely noncovalent electrostatic interactions between the functional polymer and graphene. An immediate consequence of this electrostatic picture of polymer–graphene interactions is that the zwitterion concentration can be tuned *a priori* to induce desired Fermi level shifts in graphene, which will be studied elsewhere.

## 5.6 Conclusions

In conclusion, a scalable and precise approach for fabricating hybrid polymer–graphene nanoscale devices has been demonstrated. Beyond graphene, the ability to dope other 2D materials - including semiconductors such as transition-metal dichalcogenides and phosphorene, among others - in a controlled manner can be pivotal for the development of nanoscale optoelectronic devices. The patterning and synthetic methods developed in this work can be extended more generally to other 2D materials and, in conjunction with polymer dielectric substrates, could offer a path towards low power, flexible 2D-materials-based electronics.

## 5.7 References

1. Tanachutiwat, S., Lee, J., Wang, W. & Sung, C. Reconfigurable Multi-Function Logic Based on Graphene pn Junctions. *Proc. 47th Des. Autom. Conf. ACM* 883–888 (2010).
2. Williams, J. R., Low, T., Lundstrom, M. S. & Marcus, C. M. Gate-controlled guiding of electrons in graphene. *Nat. Nanotechnol.* **6**, 222–225 (2011).
3. Cheianov, V. V., Fal, V. & Altshuler, B. L. The Focusing of Electron Flow and a Veselago Lens in Graphene p-n Junctions. **315**, 1252–1255 (2007).
4. Park, C., Son, Y., Yang, L., Cohen, M. L. & Louie, S. G. Electron Beam Supercollimation in Graphene Superlattices. *Nano Lett.* **8**, 2920–2924 (2008).
5. Barnard, A. W. *et al.* Absorptive pinhole collimators for ballistic Dirac fermions in graphene. *Nat. Commun.* **8**, 15418–15424 (2017).
6. Chen, S. *et al.* Electron optics with ballistic graphene junctions. *Science.* **353**, 1522–1525 (2016).
7. Gabor, N. *et al.* Hot Carrier-Assisted Intrinsic Photoresponse in Graphene. *Science* **334**, 648–652 (2011).
8. Lemme, M. C. *et al.* Gate-activated photoresponse in a graphene p-n junction. *Nano Lett.* **11**, 4134–4137 (2011).
9. Georgakilas, V. *et al.* Functionalization of graphene: Covalent and non-covalent approaches, derivatives and applications. *Chem. Rev.* **112**, 6156–6214 (2012).
10. Lee, S. K. *et al.* Inverse transfer method using polymers with various functional groups for controllable graphene doping. *ACS Nano* **8**, 7968–7975 (2014).
11. Choi, Y. *et al.* On-demand doping of graphene by stamping with a chemically functionalized rubber lens. *ACS Nano* **9**, 4354–4361 (2015).
12. Shlimak, I. *et al.* Raman scattering and electrical resistance of highly disordered graphene. *Phys. Rev. B - Condens. Matter Mater. Phys.* **91**, 3–6 (2015).
13. Lee, H. *et al.* Poly(sulfobetaine methacrylate)s as electrode modifiers for inverted organic electronics. *J. Am. Chem. Soc.* **137**, 540–549 (2015).
14. Ferrari, A. C. Raman spectroscopy of graphene and graphite: Disorder, electron-phonon coupling, doping and nonadiabatic effects. *Solid State Commun.* **143**, 47–57 (2007).



15. Das, A. *et al.* Monitoring dopants by Raman scattering in an electrochemically top-gated graphene transistor. *Nat. Nanotechnol.* **3**, 210–215 (2008).
16. Yan, J., Zhang, Y., Kim, P. & Pinczuk, A. Electric field effect tuning of electron-phonon coupling in graphene. *Phys. Rev. Lett.* **98**, 1–4 (2007).
17. Xia, F., Farmer, D. B., Lin, Y. M. & Avouris, P. Graphene field-effect transistors with high on/off current ratio and large transport band gap at room temperature. *Nano Lett.* **10**, 715–718 (2010).
18. Herring, P. K. *et al.* Photoresponse of an electrically tunable ambipolar graphene infrared thermocouple. *Nano Lett.* **14**, 901–907 (2014).
19. Guo, B. *et al.* Controllable N-doping of graphene. *Nano Lett.* **10**, 4975–4980 (2010).
20. Yu, Q. *et al.* Control and characterization of individual grains and grain boundaries in graphene grown by chemical vapour deposition. *Nat. Mater.* **10**, 443–449 (2011).
21. Yu, Y.-J. J. *et al.* Tuning the graphene work function by electric field effect. *Nano Lett.* **9**, 3430–3434 (2009).
22. Cahen, D., Naaman, R. & Vager, Z. The cooperative molecular field effect. *Adv. Funct. Mater.* **15**, 1571–1578 (2005).
23. Kresse, G. & Furthmüller, J. Efficient iterative schemes for ab initio total-energy calculations using a plane-wave basis set. *Phys. Rev. B* **54**, 11169–11186 (1996).
24. Kresse, G. & Joubert, D. From ultrasoft pseudopotentials to the projector augmented-wave method G. *Phys. Rev. B* **59**, 1758–1775 (2013).
25. Selhorst, R. C. *et al.* Tetrathiafulvalene-containing polymers for simultaneous non-covalent modification and electronic modulation of MoS<sub>2</sub> nanomaterials. *Chem. Sci.* **7**, 4698–4705 (2016).

## CHAPTER 6

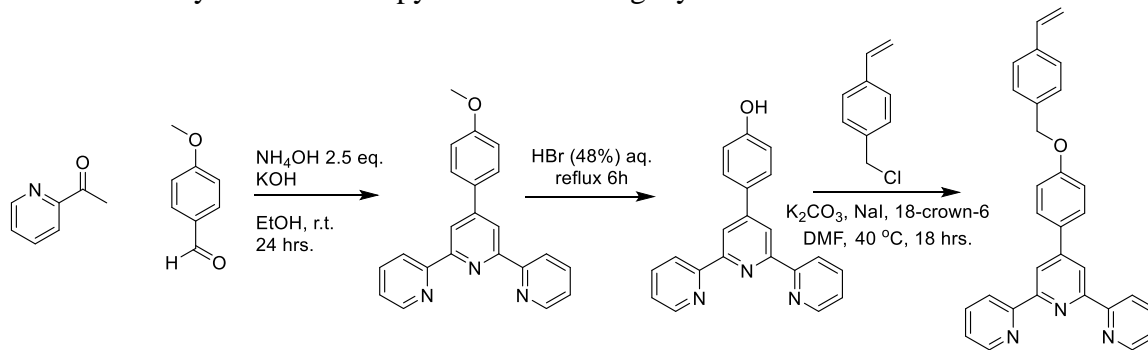
### OUTLOOK

#### 6.1 Doping *via* Polymer Coordination Complexes

This dissertation has highlighted the use of organochalcogens and polymer zwitterions as physisorbing functionalities to alter the intrinsic electronic properties of 2D materials including TMDCs and graphene. For TMDCs, there are numerous examples of organic molecules as adsorbates that interact with basal plane chalcogen atoms, and few examples of metals as the doping species.<sup>1-3</sup> Treating MoS<sub>2</sub> transistors with a dilute solution of gold (III) chloride showed complete inversion of charge conduction characteristics from n-type to p-type conduction.<sup>4</sup> Carrier inversion occurs due to the redox potentials of MoS<sub>2</sub> and gold (III), with MoS<sub>2</sub> acting as a good reducing agent for gold. The reduction is confirmed by electron microscopy of monolayer MoS<sub>2</sub> with gold (III) chloride, showing the formation of gold nanoparticles covering the substrate. Higher concentrations of the metal species leads to metallic behavior in MoS<sub>2</sub> transistors as a high density of gold nanoparticles crowd the surface and render the semiconductor metallic. This behavior has also been shown for carbon nanotubes, with gold nanoparticles decorating the surface of the nanotubes after treatment with gold (III) chloride.<sup>5</sup> While the use of small molecules lead to advantageous charge conduction characteristics, dropcasting small molecules suffers from the fouling of the surface with large nanoparticles and leads to irreversible and uncontrolled doping.

Polymers containing ligands favorable for metal coordination could alleviate issues associated with nanoparticle formation and afford polymers with a tunable content of dopant metals that is patternable and reversible. Initial experiments attempted to

**Scheme 6.1.** Synthesis of a terpyridine containing styrene monomer



synthesize a series of polymers containing terpyridine as a tridentate ligand to coordinate different metals to be used as dopants on 2D materials. The synthesis of a terpyridine functionalized styrenic monomer is outlined in Scheme 6.1. Methoxyterpyridine was synthesized by the Kronkhe method by treatment of 2-acetylpyridine with 4-methoxybenzaldehyde in the presence of aqueous ammonia.<sup>6</sup> Demethylation of methoxyterpyridine was accomplished by refluxing in 48% hydrobromic acid and a polymerizable monomer was then synthesized by the substitution of 4-vinylbenzylchloride with the hydroxyterpyridine derivative. Two approaches were taken to introduce coordination complexes in polymers: pre- and post-polymerization coordination. Ruthenium was the first metal chosen to demonstrate coordination to polymer ligands as ruthenium terpyridine complexes are widely studied and known to form stable complexes.<sup>7</sup> Styrene terpyridine was subjected to reaction with  $\text{RuCl}_3$  to afford the coordinated monomer in yields approaching 80% (Figure 6.1A). However, upon copolymerization of the coordination complex with styrene, only starting material was recovered, suggesting

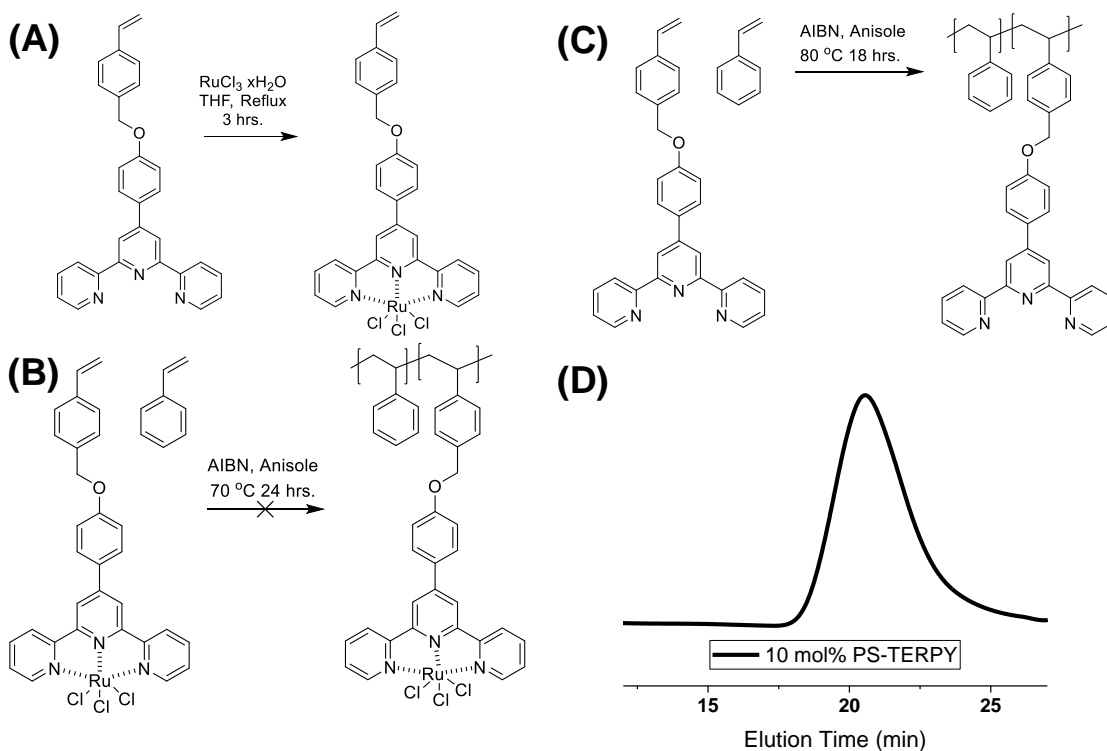


**Figure 6.1:** (A) Pre-polymerization coordination of ruthenium(III) chloride to a terpyridine-containing styrene monomer. (B) Attempted free-radical copolymerization of the ruthenium coordinated styrene monomer with styrene that resulted in only starting material after reaction. (C) Copolymerization of styrene-terpyridine with styrene with successful polymer formation confirmed by gel permeation chromatography (D).

the metal inhibits radical propagation, therefore, post-polymerization coordination was employed (Figure 6.1B). Upon conventional free-radical copolymerization of styrene terpyridine with styrene, high molecular weight polymer ( $\sim 50$  kDa) was obtained with monomodal molecular weight distribution and dispersity of 1.6 (Figure 6.1C,D). The terpyridine-containing polymers were then coordinated to metals, starting with ruthenium. Refluxing excess  $\text{RuCl}_3$  with the polymer resulted in metal coordinated polymer as indicated by UV-Vis, PL, and NMR spectroscopies. As gold is known to induce carrier inversion in  $\text{MoS}_2$  devices, terpyridine polymers were then subjected to coordination to  $\text{AuCl}_3$ . However, upon adding  $\text{AuCl}_3$  to the polymer solution at various temperatures and

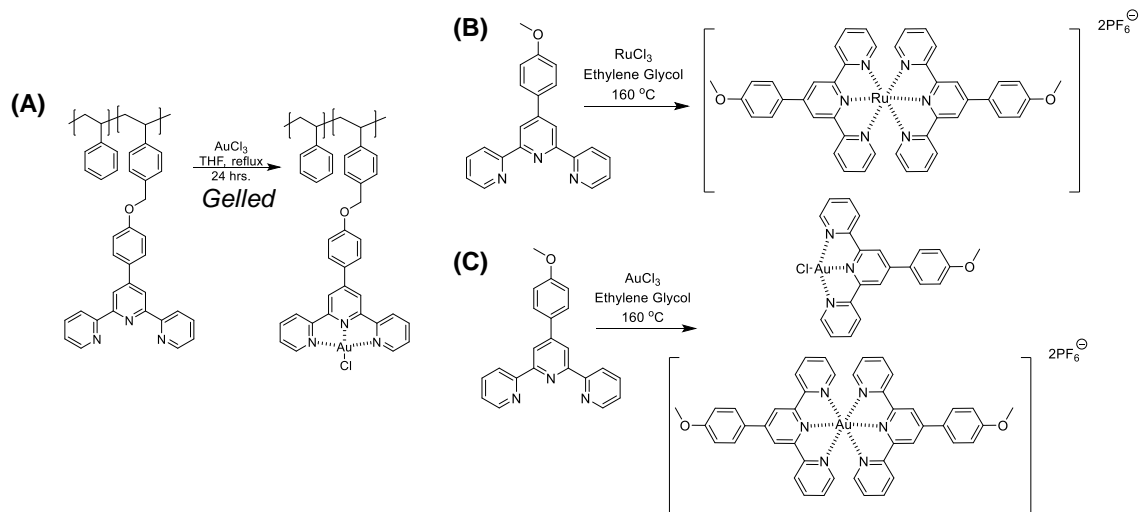


**Figure 6.2.** (A) Attempted post-polymerization coordination of ruthenium (III) chloride with a terpyridine-containing polymer that resulted in crosslinking. (B) Model small molecule complex formed by the reaction of 1 equiv. of ruthenium (III) chloride with 2 equiv. of methoxy terpyridine. (C) Model small molecule complex formed by the reaction of 1 equiv. of gold (III) chloride with 2 equiv. of methoxy terpyridine with the reaction producing both mono- and bis-complexes.

concentrations, immediate formation of insoluble product was observed. The insoluble product is the result of polymer crosslinking with the metal salt acting as the crosslinking moiety (Figure 6.2A). While ruthenium forms a stable monocoordinated complex, gold does not as it is in equilibrium with the bis-coordinated complex and therefore enables inter-polymer crosslinking. For future experiments on 2D materials, rather than undergoing multi-step polymer syntheses, model complexes with ruthenium and gold were synthesized with the ruthenium derivative forming exclusively the bis-complex and the gold forming a mixture of mono- and bis-complexes (Figure 6.2B,C). These model complexes will be monitored spectroscopically in the presence of 2D materials and specifically on 2D material devices. The interest being whether, or not, the complexes dope the 2D materials, form nanoparticles, and is reversible.

## 6.2 Covalent Organoselenium

### Doping of TMDCs

The primary method of 2D material functionalization outlined in the previous chapters has been non-covalent physisorption. However, covalent functionalization is an alternative to non-covalent physisorption that utilizes organic thiols to backfill chalcogen vacancies on the basal plane and edges of

TMDCs.<sup>8,9</sup> To date, only thiols have been used as the active chalcogen to backfill vacancies and no examples of organoselenium functionalization are present in the literature. Ready access to organoselenides will expand the range of TMDCs used for solution and electronic modification including p-type tungsten diselenide (WSe<sub>2</sub>). 1,2,3-selenadiazoles (SDZs) present an opportunity to functionalize selenium-based TMDCs with small molecules and polymers enabled by its unique degradation pathway.<sup>10-13</sup> Figure 6.3A shows the multiple degradation pathways of SDZs with stimuli such as heat, irradiation, and the use of a base to liberate diatomic nitrogen, resulting in the generation of alkyne selenide anions or radicals. Each of these species could be used to backfill selenium vacancies in TMDCs

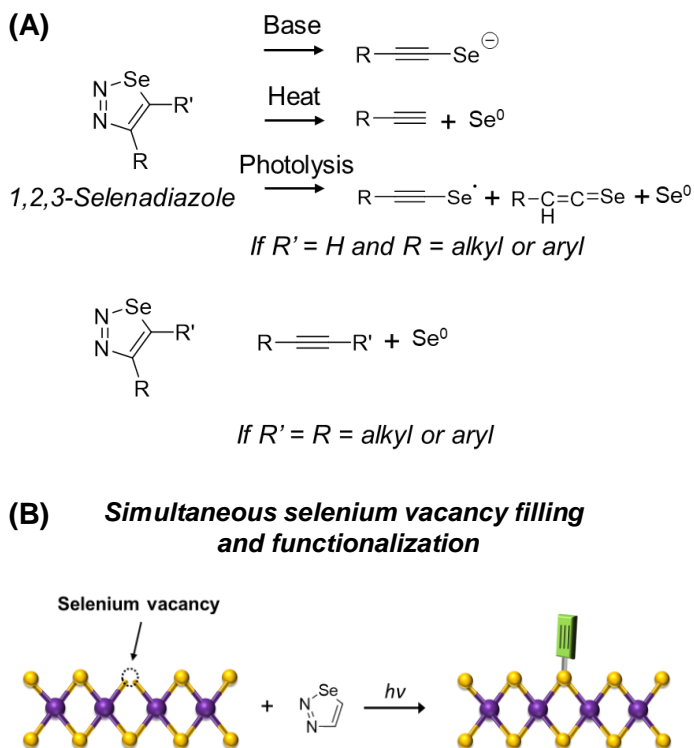


**Figure 6.3.** (A) Degradation pathways of SDZ using heat, light, and base to produce active alkyne selenide anions or radicals. (B) *In situ* functionalization of selenium-based TMDCs with the products of SDZ degradation.

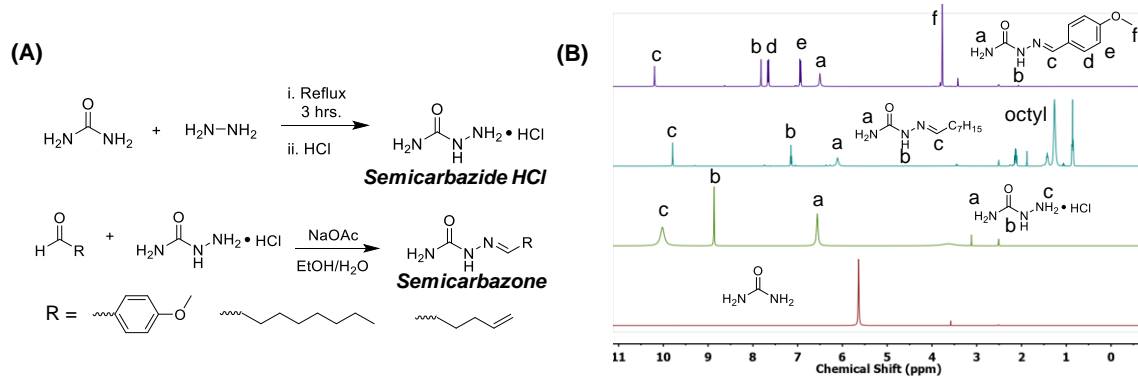


**Figure 6.4.** (A) Synthesis of semicarbazide HCl and functional semicarbazones as precursors to SDZs. (B)  $^1\text{H}$  NMR spectra showing the successful synthesis of precursors while providing a post-functionalization alkyne handle that can be used in azide-alkyne cycloaddition “click” chemistry to afford functional TMDC nanosheets (Figure 6.3B). Furthermore, the use of light as stimuli for degradation opens up doors for precise spatial patterning of monolayer TMDCs that could lead to spatially tailored electronics.

The synthesis of SDZ precursors, semicarbazones, are outlined in figure 6.4A. Briefly, refluxing hydrazine in the presence of urea yields the condensation product,

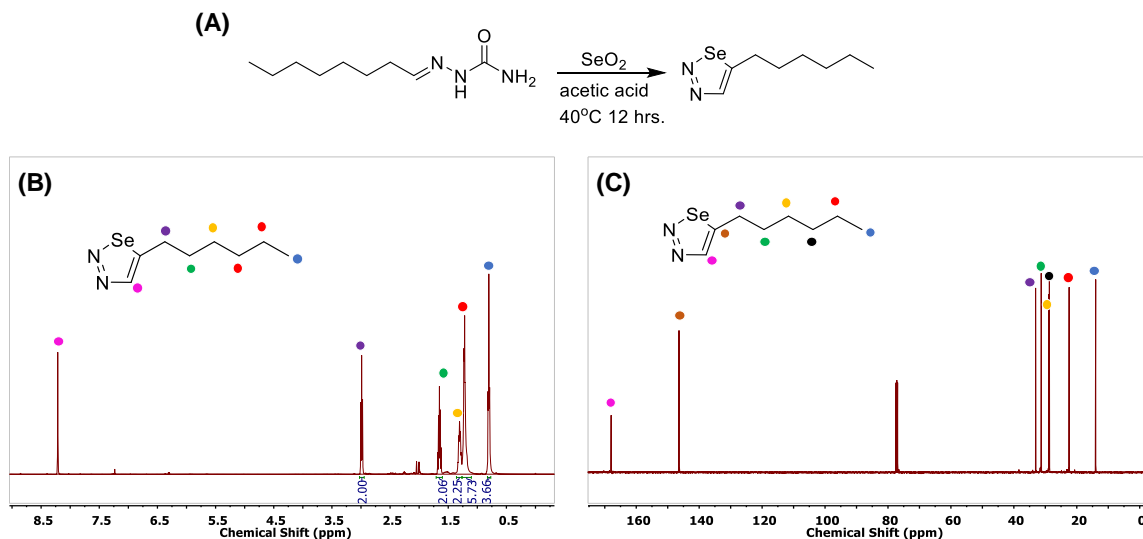


**Figure 6.5.** (A) Synthesis of heptyl SDZ from octyl semicarbazone. (B)  $^1\text{H}$  NMR spectrum of heptyl SDZ noting the aromatic SDZ resonance at 8.25ppm. (C)  $^{13}\text{C}$  NMR spectrum of heptyl SDZ displaying the two aromatic SDZ resonances at 145 ppm and 168 ppm.

semicarbazide hydrochloride, which undergoes imination in the presence of a primary amine to form the semicarbazone. The  $^1\text{H}$  NMRs of the precursors and some selected semicarbazones are shown in figure 6.4b. Functional semicarbazones are then converted to their corresponding SDZs *via* oxidation with selenium dioxide, with NMR spectroscopy confirming successful conversion (Figure 6.5). The synthesis of the precursors gave high yields approaching 90% but the oxidation to SDZ results in low yields of ~15%. The oxidation produces solid elemental selenium and the low yields could be the result of inefficient cyclization or selenium oligomerization. Future work in SDZs would require more insight into the synthesis of functional SDZs and their degradation pathways. Subjecting suspensions of TMDCs to SDZ under degradation conditions will result in *in situ* functionalized nanosheets with the prospect of controlling solution and electronic properties dictated by the functionality on the SDZs.

### **6.3 Polymer Zwitterion for Bidirectional Doping of 2D Materials**

Chapter 5 discussed the application of a zwitterionic copolymer (PSBMA-*co*-PMMA) as a functional photoresist that can simultaneously pattern and dope graphene. Rather than doping by charge transfer, the strong inherent dipole of the zwitterion acts to dope graphene *via* electrostatic dipolar interactions. The continuation of this project would consist of using different polymer zwitterions as photoresists for 2D materials. While results of the DFT calculations show that PSBMA is angled such that there is a net out-of-plane dipole,<sup>14</sup> other zwitterions, such as methacryloyloxyethyl phosphorylcholine (MPC), could be used to achieve an opposite orientation of the dipole resulting in complementary doping. However, different zwitterions endow the resulting polymer with differing



solubility and therefore, work on the synthesis of zwitterionic copolymers with solution properties amenable to lithographic processes must be investigated. Similar experiments outlined in chapter 5 will verify if the polymer is appropriate for photoresists and device experiments will show if the polymers dope 2D materials in a manner that is complementary to PSBMA-*co*-PMMA. The fabrication of such a polymer scaffold will advance the technology of spatially doped semiconductors using polymers that have advantageous solution properties and could be used to design next generation 2D material p-n junctions or diode-based devices.

## 6.4 References

1. Jing, Y., Tan, X., Zhou, Z. & Shen, P. Tuning electronic and optical properties of MoS<sub>2</sub> monolayer *via* molecular charge transfer. *J. Mater. Chem. A* **2**, 16892–16897 (2014).
2. Kiriya, D., Tosun, M., Zhao, P., Kang, J. S. & Javey, A. Air-stable surface charge transfer doping of MoS<sub>2</sub> by benzyl viologen. *J. Am. Chem. Soc.* **136**, 7853–7856 (2014).
3. Du, Y., Liu, H., Neal, A. T., Si, M. & Ye, P. D. Molecular Doping of Multilayer MoS<sub>2</sub> Field-Effect Transistors: Reduction in Sheet and Contact Resistances. *IEEE Electron Device Lett.* **34**, 1328–1330 (2013).
4. Liu, X. *et al.* P-Type Polar Transition of Chemically Doped Multilayer MoS<sub>2</sub> Transistor. *Adv. Mater.* **28**, 2345–2351 (2016).
5. Kim, S. M. *et al.* Role of Anions in the AuCl<sub>3</sub> Doping of Carbon Nanotubes. *ACS Nano* **5**, 1236–1242 (2011).
6. Banjoko, V., Xu, Y., Mintz, E. & Pang, Y. Synthesis of terpyridine-functionalized poly(phenylenevinylene)s: The role of meta -phenylene linkage on the Cu<sup>2+</sup> and Zn<sup>2+</sup> chemosensors. *Polymer.* **50**, 2001–2009 (2009).
7. Cheng, K. W. *et al.* Synthesis of Conjugated Polymers with Pendant Ruthenium Terpyridine Trithiocyanato Complexes and Their Applications in Heterojunction Photovoltaic Cells. *J. Polym. Sci. Part A Polym. Chem.* **46**, 1305–1317 (2008).
8. Ding, Q. *et al.* Basal-Plane Ligand Functionalization on Semiconducting 2H-MoS<sub>2</sub> Monolayers. *ACS Appl. Mater. Interfaces* **9**, 12734–12742 (2017).
9. Chou, S. *et al.* Ligand Conjugation of Chemically Exfoliated MoS<sub>2</sub>. *J. Am. Chem. Soc.* **135**, 4584–4587 (2013).
10. Lalezari, I. & Shafiee, A. 1,2,3-Selenadiazole and Its Derivatives. *J. Org. Chem.* **36**, 2836–2838 (1971).
11. Meier, H. & Menzel, I. Formation of Cyclo-octyne by Pyrolysis of Cyclo-octeno-1,2,3-selenadiazole. *J. Chem. Soc. D Chem. Commun.* 1059 (1971).
12. Maryanoff, B. E. & Rebarchak, M. C. Unusual Medium Effect on the Distribution of 1,2,3-Selenadiazole Regioisomers in the Reaction of N-Benzyl-4-homopiperidinone Semicarbazone with Selenium Dioxide. *J. Org. Chem.* **56**, 5203–5207 (1991).

13. Lalezari, I., Shafiee, A., Khorrami, J. & Soltani, A. Selenium Heterocycles XXII: Synthesis and Antibacterial and Antifungal Activities of Arylsulfonyl-1,2,3-selenadiazoles. *J. Pharm. Sci.* **67**, 1336–1338 (1978).
14. Alon, H. *et al.* Lithographically Patterned Functional Polymer-Graphene Hybrids for Nanoscale Electronics. *ACS Nano* **12**, 1928–1933 (2018).

## CHAPTER 7

### EXPERIMENTAL SECTION

#### 7.1 Materials

Sodium borohydride (98%), Grubbs generation I catalyst (97%), *exo*-5-norbornene carboxylate (97%), triphenylphosphine (99%), dimethylaminopyridine (DMAP) (98%), sodium hydride (60% suspension in mineral oil), sodium azide (99.5%), copper(I) bromide (99.99%), N,N,N',N',N''-pentamethyldiethylenetriamine (PMDETA) (99%), ethyl-2-bromoisobutyrate (98%), 4-Cyano-4-(thiobenzoylthio)pentanoic acid (97%), ethyl vinyl ether (99%), tetrabutylammoniumhexafluoro phosphate (TBAPF<sub>6</sub>) (98%), Molybdenum (IV) sulfide (99%), n-butyl lithium (1.6M in hexanes), hexanol (98%), ethanolamine (95%), allyl amine (98%), 2-methoxyethylamine (95%), N,N-dimethylaminopropylamine (95%), 2-methoxyethylamine (95%), tetraethyleneglycol (99%), hexamethylene diisocyanate (HMDI) (98%), carbon disulfide (98%), dibutyltin dilaurate (DBTDL) (95%), methylamine (2.0M in toluene), 1-hexylamine (98%), sulfobetaine methacrylate (98%), chloroform (99%), dimethylsulfoxide (DMSO) (99.98%), anhydrous anisole (99.7%), and anhydrous N,N-dimethylformamide (99.8%) were purchased from Aldrich. Methyl methacrylate (99%), n-butyl methacrylate (99%), 2-formyltetrathiafulvalene (98%), 1-ethyl-3-(3-dimethylaminopropyl)carbodiimide (EDC) (98%), Dimethylacetylene dicarboxylate (DMAD) (96%) were purchase from TCI. Trishydroxymethyl phosphine (95%) was purchased from Strem Chemicals. Propargyl bromide (95%), 18-crown-6 (98%) and 2-chloroethyl methacrylate (97%) were purchased from Alfa Aesar. MoS<sub>2</sub>, CVD grown on Si/SiO<sub>2</sub> and sapphire (Al<sub>2</sub>O<sub>3</sub>) substrates, was purchased from SixCarbon

Technologies and used as received. Deuterated solvents were purchased from Cambridge Isotope Laboratories, Inc., and Sigma-Aldrich. Azobisisobutyronitrile (AIBN) was recrystallized from methanol prior to use. Methyl methacrylate, n-butyl methacrylate and 2-chloroethyl methacrylate were run through a plug of alumina prior to use to remove inhibitors present in the commercial source. All other chemicals were used as received. Dichloromethane was distilled over calcium hydride and tetrahydrofuran was distilled over sodium/benzophenone prior to use.

## 7.2 Instrumentation

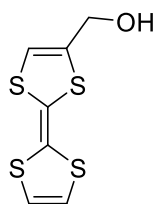
$^1\text{H}$  NMR (500 MHz) and  $^{13}\text{C}$  NMR (125 MHz), spectra were obtained using a Bruker Ascend<sup>TM</sup> 500 spectrometer equipped with a Prodigy cryoprobe. High resolution fast atom bombardment (FAB) mass spectrometry was performed on a double focusing magnetic sector mass-spectrometer JEOL-700 MS station and Electrospray ionization (ESI) mass spectrometry data were obtained using a Bruker MicroTOF II mass spectrometer. ESI-MS employed chloroform solutions of 1 mg/mL. All mass spectrometry was performed at the UMass Amherst Mass Spectrometry Center. The FTIR spectra were obtained with a Perkin-Elmer Spectrum One FT-IR spectrometer. Gel permeation chromatography (GPC) was carried out in THF at 40 °C using a flow rate of 1.0 mL/min on an Agilent 1260 infinity system with a G1362A refractive index detector and G1310B isocratic pump, equipped with a PLgel 5  $\mu\text{m}$  mixed-c (7.5  $\times$  300 mm), a PLgel 5  $\mu\text{m}$  mixed-d (7.5  $\times$  300 mm), and a 5  $\mu\text{m}$  guard column (7.5  $\times$  50 mm) calibrated against poly(methyl methacrylate) (PMMA) and polystyrene (PS) standards. GPC in DMF was carried out in 0.01 M LiCl at 50 °C against PEO calibration standards. Samples were run using a flow

rate of 1.0 mL/min with a Sonntek K-501 pump, one 50 × 7.5 mm PL gel mixed guard column, one 300 × 7.5 mm PL gel 5 μm mixed C column, one 300 × 7.5 mm PL gel 5 μm mixed D column and using a Knauer refractive index detector (K-2301) and an Alltech model 3000 solvent recycler. GPC eluting in TFE containing 0.02 M trifluoroacetate was performed against poly(methyl methacrylate) standards, operating at 40 °C with a flow rate of 1.0 mL/min using an Agilent 1200 system equipped with an isocratic pump, a degasser, an autosampler, one 50 x 8 mm<sup>2</sup> Polymer 132 Standards Service (PSS) PFG guard column, three 300 x 7.5 mm<sup>2</sup> PSS PFG analytical linear M columns with 7 μm particle size, and Agilent 1200 refractive index and UV detectors. UV-Visible spectra were recorded on an Ocean Optics USB2000+XR spectrophotometer and a Shimadzu UV-2600 spectrophotometer equipped with a temperature-controlled cell. All experiments used a 1.0 cm quartz cuvette. Cyclic voltammetry was carried out using an Epsilon Basic electrochemical workstation with C3-cell stand (BASi Instruments). Thermogravimetric analysis (TGA) was performed on a Q500 (TA instruments) thermogravimetric analyzer under nitrogen atmosphere. The temperature was swept from 30 °C to 800 °C at a temperature ramp of 10 °C/min. High-resolution transmission electron microscopy (HRTEM) was performed on a JEOL JEM-2200FX microscope using samples prepared on 400 square mesh holey carbon-coated copper grids (Electron Microscopy Sciences). Chemically exfoliated MoS<sub>2</sub> nanosheets were imaged by a scanning force microscope (Nanoscope III, Digital Instrument Co., Santa Barbara, CA) in tapping mode. Optical microscopy measurements were performed on an inverted optical microscope (Zeiss Axiovert 200) equipped with a QImaging camera (Retiga-2000R Fast 1394 Mono Cooled). Domain spacings of BT polymer films were characterized using small and wide-angle X-

ray scattering (SAXS/WAXS) using a Ganesha SAXS/WAXS-LAB instrument with Cu K $\alpha$  0.154 nm line on SAXS or WAXS mode. Raman spectra were measured using a Raman microscope (LabRAM HR Evolution, HORIBA Scientific) with a 532 nm laser. Mapping data were fit to Lorentzian functions using a custom Matlab script. Device measurements were carried out using a ceramic leadless chip carrier for sample holding and then measured under vacuum with a Keithley 2540 or Keysight B1500A. All device data were collected at room temperature.

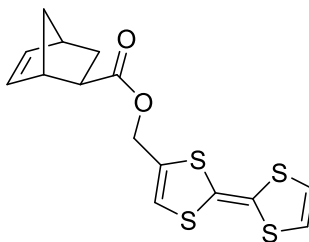
### 7.3 Methods

#### Synthesis of 2-Hydroxymethyltetrathiafulvalene (TTF-OH)<sup>1</sup>



To a stirring solution of 2-formyl tetrathiafulvalene (1.24 g, 5.31 mmol) and methanol (120 mL) was added sodium borohydride (0.37 g, 10 mmol) over a period of 5 minutes. The mixture was allowed to stir for 30 minutes, and the bright yellow solution was concentrated by rotary evaporation. The residue was purified by column chromatography on silica gel, eluting with dichloromethane, to afford a bright yellow solid upon drying. Yield: 1.15 g, 93%. <sup>1</sup>H NMR (500 MHz, CDCl<sub>3</sub>),  $\delta$  (ppm): 6.27 (d,  $J$  = 35.4 Hz, 2H), 4.41 (s, 2H), 1.72 (t,  $J$  = 6.3 Hz, 1H).

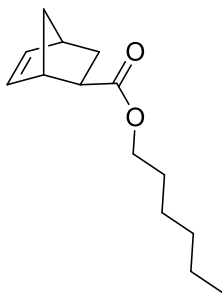
**Exo-5-norbornene-3-(hydroxymethyltetraathiafulvalene)ester (TTF-NB)<sup>2</sup>**



Exo-5-norbornene-3-carboxylic acid (0.55 g, 4.0 mmol), EDC (0.7 g, 4.5 mmol), DMAP (0.045 g, 0.35 mmol), and anhydrous dichloromethane (20 mL) were combined in a roundbottom flask, degassed for 15 min with nitrogen gas, and cooled to 0 °C. To the resulting mixture was added, dropwise, a degassed solution of compound 1 (0.86 g, 3.7 mmol) in anhydrous dichloromethane (10 mL). The reaction mixture was allowed to warm to room temperature and stirred overnight under a nitrogen atmosphere. The resulting solution was washed with saturated aqueous NaHCO<sub>3</sub> solution followed by 3 washes with water. The organic layer was separated, dried over MgSO<sub>4</sub> and the excess solvent was removed by rotary evaporation. Purification of the residue was performed by column chromatography on silica gel using a dichloromethane:hexanes mixture (1:1 volume ratio) as the mobile phase, followed by drying under vacuum to afford the product as yellow crystals. Yield: 1.06 g, 75%. <sup>1</sup>H NMR (500 MHz, CDCl<sub>3</sub>), δ (ppm): 6.32 (d, *J* = 2.3 Hz, 3H), 6.18 – 6.08 (m, 2H), 4.83 (s, 2H), 3.07 (s, 1H), 2.94 (s, 1H), 2.26 (dd, *J* = 10.0, 4.5 Hz, 1H), 1.93 (dt, *J* = 11.7, 4.0 Hz, 1H), 1.52 (d, *J* = 8.9 Hz, 1H), 1.45-1.31 (m, 2H); <sup>13</sup>C (126 MHz, CDCl<sub>3</sub>) 30.4, 41.7, 43.0, 46.4, 46.7, 60.8, 109.3, 111.7, 118.9, 119.0, 119.1, 131.4, 135.7, 138.2, 175.7. ESI-MS: *m/z* calculated for C<sub>15</sub>H<sub>14</sub>O<sub>2</sub>S<sub>4</sub> [M<sup>+</sup>]: 353.9877, found: 353.9863.



### Exo-5-norbornene-3-hexyl ester (hexyl-NB)



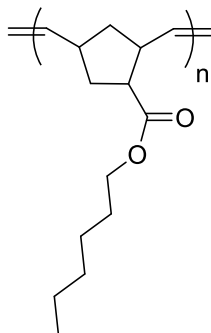
Exo-5-norbornene-3-carboxylic acid (2.0 g, 14.5 mmol), EDCI (2.9 g, 15.0 mmol), DMAP (0.065 g, 0.35 mmol), and 20 mL of anhydrous DCM were combined in a roundbottom flask, degassed for 15 min (N<sub>2</sub> purging) and cooled to 0 °C. To the resulting mixture, a degassed solution of 1-hexanol (1.6 g, 15.0 mmol) in dichloromethane (10 mL) was added dropwise by syringe. The reaction mixture was then allowed to warm to room temperature and stirred overnight. The solution obtained was washed with saturated NaHCO<sub>3</sub> solution followed by three washes with water. The organic layer was separated, dried over MgSO<sub>4</sub> and concentrated. The residue was purified by column chromatography on silica gel, eluting with hexanes:ethyl acetate (7:3 volume ratio) to afford a clear liquid after evaporation of excess solvent. Yield: 2.9 g, 90%. <sup>1</sup>H NMR (500 MHz, CDCl<sub>3</sub>), δ (ppm): 1.91 (dt, *J* = 11.8, 4.0 Hz, 1H), 1.61 (p, 2H), 1.51 (d, *J* = 8.4 Hz, 1H), 1.38 – 1.28 (m, 8H), 0.88 (t, *J* = 6.8 Hz, 3H).

### Typical procedure for ring-opening metathesis polymerization (ROMP) of TTF-substituted norbornenes.

Compounds TTF-NB and hexyl-NB, PPh<sub>3</sub>, and 0.5 mL of anhydrous THF were combined in a 20 mL vial and equipped with a septum. In a separate 20 mL vial, equipped with a

septum and a stir bar, the ruthenium benzylidene catalyst (Grubbs Generation I catalyst) was dissolved in anhydrous THF (0.5 mL). Both solutions were subjected to three freeze-pump-thaw cycles, then allowed to return to room temperature. The monomer solution was added to the catalyst solution by syringe, and the mixture was stirred for 10 min. The polymerization was terminated by the addition of excess ethyl vinyl ether (EVE) (0.2 mL), and a solution of tris(hydroxymethyl)phosphine (0.10 g, 0.75 mmol) in THF (0.5 mL) was added as a ruthenium scavenger 30 minutes after termination with the vinyl ether. This mixture was allowed to stir overnight, and the resultant solution was precipitated twice into a large excess of MeOH to give a bright yellow tacky solid.

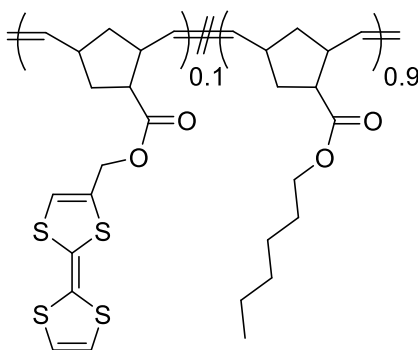
### Poly-n-hexylNB



Hexyl-NB (0.2 g, 0.9 mmol), PPh<sub>3</sub> (0.004 g, 0.015 mmol), and Grubbs Generation I catalyst (0.013 g, 0.016 mmol) were added in anhydrous THF (1 mL): Yield: 0.16 g, 84%. GPC (estimated against polystyrene standards and eluting in THF): M<sub>n</sub> = 50 kDa, PDI = 1.20. <sup>1</sup>H NMR (500 MHz, CDCl<sub>3</sub>), δ (ppm): 5.35 (broad, s, 2H *trans* from polymer backbone), 5.15-5.25 (broad, m, 2H *cis* from polymer backbone), 2.70-2.90 (broad, m, 3H), 2.35-2.50 (broad, m, 2H), 1.70-1.95 (broad, m, 6H), 1.25-1.45 (broad, m, 4H), 0.90-1.10 (broad, m, 5H). <sup>13</sup>C NMR (125 MHz, CDCl<sub>3</sub>), δ (ppm): 176.48, 133.70-134.50 (multiple), 132.9-133.5

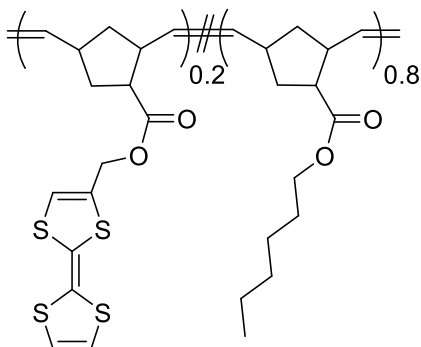
(multiple), 64.77, 49.80-51.00 (multiple), 43.62, 43.34, 42.94, 42.29, 41.55, 38.85, 38.61, 33.33, 32.56, 32.39, 31.65, 28.91, 25.81, 22.75.

### PolyTTFNB-10 (P1a)



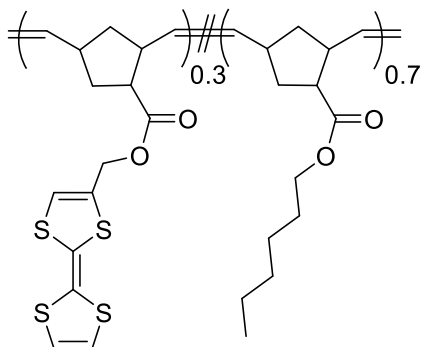
TTF-NB (0.035 g, 0.1 mmol), hexyl-NB (0.2 g, 0.9 mmol), PPh<sub>3</sub> (0.004 g, 0.015 mmol), and Grubbs Generation I catalyst (0.013 g, 0.016 mmol) were added in anhydrous THF (1 mL). Monomer conversion from <sup>1</sup>H NMR: 60%. Yield: 0.12 g, 85%. GPC (*versus* PS in THF): M<sub>n</sub> = 25 kDa, PDI = 1.26. <sup>1</sup>H NMR (500 MHz, CDCl<sub>3</sub>), δ (ppm): 6.31(s, 2H from TTF ring), 6.29 (s, 1H from TTF ring), 5.30-5.50 (m, 4H *trans* from polymer backbone) 5.15-5.28 (m, 4H *cis* from polymer backbone), 4.72-4.87 (broad, m, 2H TTF methylene spacer), 4.00-4.10 (broad, m, 2H), 3.08 (broad, s, 4H, *cis*), 2.96 (broad, s, 4H, *cis*), 2.45-2.80 (broad, m, 10H), 2.01-2.15 (broad, m, 2H), 1.89-2.00 (broad, m, 2H), 1.54-1.73 (broad, m, 4H), 1.25-1.39 (broad, m, 6H from hexyl chain), 1.09-1.22 (broad, m, 2H), 0.88 (t, 3H, J = 6.2Hz, from hexyl chain). <sup>13</sup>C NMR (125 MHz, CDCl<sub>3</sub>), δ (ppm): 176.14, 175.47, 130.60-133.80 (multiple), 128.65, 126.14, 119.29, 119.18, 111.79, 109.40, 64.67, 60.86, 51.05, 50.46, 50.16, 49.00-50.05 (multiple), 47.00-48.10 (multiple), 43.15, 42.10, 41.29, 37.37, 36.36, 31.60, 28.84, 25.77, 22.72, 14.25.

### PolyTTFNB-20 (P1b)



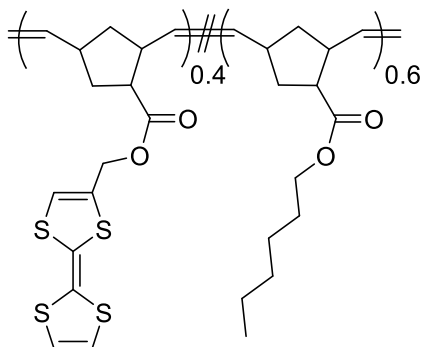
TTF-NB (0.070 g, 0.2 mmol), hexyl-NB (0.18 g, 0.8 mmol),  $\text{PPh}_3$  (0.004 g, 0.015 mmol), and Grubb's Generation I catalyst (0.013 g, 0.016 mmol) were added in anhydrous THF (1 mL). Monomer conversion from  $^1\text{H}$  NMR: 90%. Yield: 0.16 g, 76%. GPC (*versus* PS in THF)  $M_n$ : 55 kDa, PDI = 1.16.  $^1\text{H}$  NMR (500 MHz,  $\text{CDCl}_3$ ),  $\delta$  (ppm): 6.31(s, 2H from TTF ring), 6.29 (s, 1H from TTF ring), 5.29-5.50 (m, 4H *trans* from polymer backbone) 5.10-5.27 (m, 4H *cis* from polymer backbone), 4.73-4.87 (broad, m, 2H TTF methylene spacer), 4.00-4.10 (broad, m, 2H), 3.08 (broad, s, 4H, *cis*), 2.96 (broad, s, 4H, *cis*), 2.45-2.80 (broad, m, 10H), 2.00-2.15 (broad, m, 2H), 1.88-1.99 (broad, m, 2H), 1.54-1.72 (broad, m, 4H), 1.25-1.38 (broad, m, 6H from hexyl chain), 1.11-1.23 (broad, m, 2H from hexyl chain), 0.88 (t, 3H,  $J = 6.2\text{Hz}$ ).  $^{13}\text{C}$  NMR (125 MHz,  $\text{CDCl}_3$ ),  $\delta$  (ppm): 176.14, 175.47, 130.80-133.84 (multiple), 128.65, 126.14, 119.29, 119.18, 111.79, 109.40, 64.67, 60.86, 51.05, 50.46, 50.16, 49.10-49.71 (multiple), 47.00-48.20 (multiple), 43.15, 42.10, 41.29, 37.37, 36.36, 31.60, 28.84, 25.77, 22.72, 14.25.

### PolyTTFNB-30 (P1c)



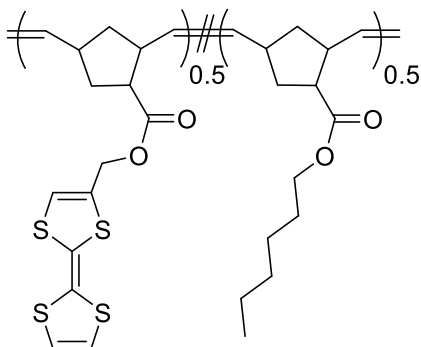
TTF-NB (0.11 g, 0.3 mmol), hexyl-NB (0.15 g, 0.7 mmol),  $\text{PPh}_3$  (0.004 g, 0.015 mmol), and Grubbs Generation I catalyst (0.014 g, 0.017 mmol) were added in anhydrous THF (1 mL). Monomer conversion from  $^1\text{H}$  NMR: 93%. Yield: 0.14 g, 58%. GPC (*versus* PS in THF)  $M_n$ : 42 kDa, PDI: 1.12.  $^1\text{H}$  NMR (500 MHz,  $\text{CDCl}_3$ ),  $\delta$  (ppm): 6.31(s, 2H from TTF ring), 6.29 (s, 1H from TTF ring), 5.29-5.48 (m, 4H *trans* from polymer backbone) 5.13-5.27 (m, 4H *cis* from polymer backbone), 4.72-4.86 (broad, m, 2H TTF methylene spacer), 3.98-4.08 (broad, m, 2H), 3.08 (broad, s, 4H, *cis*), 2.96 (broad, s, 4H, *cis*), 2.44-2.77 (broad, m, 10H), 1.98-2.14 (broad, m, 2H), 1.88-1.97 (broad, m, 2H), 1.53-1.71 (broad, m, 4H), 1.23-1.38 (broad, m, 6H from hexyl chain), 1.08-1.22 (broad, m, 2H), 0.87 (t, 3H,  $J = 6.2\text{Hz}$ , hexyl).  $^{13}\text{C}$  NMR (125 MHz,  $\text{CDCl}_3$ )  $\delta$  (ppm): 176.13, 175.46, 130.50-134.50 (multiple), 128.66, 126.13, 119.28, 119.15, 111.89, 109.40, 64.66, 60.86, 51.05, 50.46, 49.00-49.78 (multiple), 46.90-48.10 (multiple), 43.19, 42.07, 41.24, 37.27, 37.02, 36.37, 31.60, 28.87, 25.76, 22.72, 14.23.

### PolyTTFNB-40 (P1d)



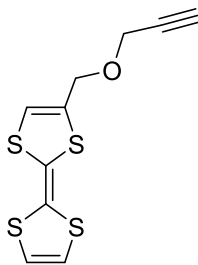
TTF-NB (0.14 g, 0.4 mmol), hexyl-NB (0.13 g, 0.6 mmol), PPh<sub>3</sub> (0.005 g, 0.019 mmol), and Grubbs Generation I catalyst (0.015 g, 0.018 mmol) were added in anhydrous THF (1 mL). Monomer conversion <sup>1</sup>H NMR: 85%. Yield: 0.17 g, 74%. GPC (*versus* PS in THF) M<sub>n</sub>: 40 kDa, PDI: 1.22. <sup>1</sup>H NMR (500 MHz, CDCl<sub>3</sub>) δ (ppm) 6.31 (s, 2H from TTF ring), 6.29 (s, 1H from TTF ring), 5.28-5.47 (m, 4H *trans* from polymer backbone) 5.13-5.27 (m, 4H *cis* from polymer backbone), 4.72-4.86 (broad, m, 2H, TTF methylene spacer), 3.98-4.08 (broad, m, 2H), 3.08 (broad, s, 4H, *cis*), 2.96 (broad, s, 4H, *cis*), 2.40-2.80 (broad, m, 10H), 1.99-2.15 (broad, m, 2H), 1.87-1.96 (broad, m, 2H), 1.53-1.74 (broad, m, 4H), 1.23-1.36 (broad, m, 6H, from hexyl chain), 1.07-1.22 (broad, m, 2H), 0.87 (t, 3H, J = 6.2Hz, from hexyl chain). <sup>13</sup>C NMR (125 MHz, CDCl<sub>3</sub>) δ (ppm): 176.13, 175.46, 130.40-134.80 (multiple), 128.65, 126.13, 119.28, 119.16, 111.87, 109.39, 64.66, 60.85, 51.04, 50.45, 49.10-50.50 (multiple), 47.00-48.20 (multiple), 43.23, 42.09, 41.20, 37.26, 37.02, 36.34, 31.59, 28.83, 25.76, 22.71, 14.24.

### PolyTTF-NB-50 (P1e)



TTF-NB (0.18 g, 0.5 mmol), hexyl-NB (0.11 g, 0.5 mmol), PPh<sub>3</sub> (0.005 g, 0.019 mmol), and (0.016 g, 0.019 mmol) Grubbs Generation I catalyst were added in anhydrous THF (1 mL). Monomer conversion estimated by <sup>1</sup>H NMR: 82%. Yield 0.20 g, 84%. GPC (*versus* PS in THF) M<sub>n</sub>: 38 kDa, PDI: 1.20. <sup>1</sup>H NMR (500 MHz, CDCl<sub>3</sub>) δ (ppm) 6.31(s, 2H from TTF ring), 6.29 (s, 1H from TTF ring), 5.30-5.47 (m, 4H *trans*, from polymer backbone) 5.14-5.28 (m, 4H *cis*, from polymer backbone), 4.72-4.86 (broad, m, 2H, TTF methylene spacer), 3.98-4.08 (broad, m, 2H), 3.08 (broad, s, 4H, *cis*), 2.96 (broad, s, 4H, *cis*), 2.45-2.78 (broad, m, 10H), 2.00-2.14 (broad, m, 2H), 1.88-1.99 (broad, m, 2H), 1.54-1.74 (broad, m, 4H), 1.24-1.38 (broad, m, 6H, from hexyl chain), 1.10-1.23 (broad, m, 2H), 0.88 (t, 3H, J = 6.2Hz, from hexyl chain). <sup>13</sup>C NMR (125 MHz, CDCl<sub>3</sub>) δ (ppm) 176.14, 175.47, 130.50-134.50 (multiple), 128.65, 126.14, 119.29, 119.18, 111.79, 109.40, 64.67, 60.86, 51.05, 50.46, 49.00-50.50 (multiple), 47.00-48.40 (multiple), 43.15, 42.10, 41.29, 37.37, 36.85, 36.36, 31.60, 28.84, 25.77, 22.72, 14.25.

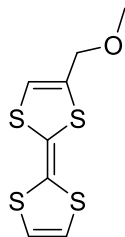
## 2-Propargyloxymethyltetraathiafulvalene



Sodium hydride (38 mg, 1.6 mmol) was added under a nitrogen blanket to a dry, nitrogen purged flask, and the flask was cooled to 0 °C. Anhydrous THF (45 mL) was added by syringe, and the resulting suspension stirred for 5 minutes. A solution of TTF-OH (500 mg, 2.13 mmol) in dry THF (3 mL) was then added dropwise. The solution obtained was stirred for 15 minutes, followed by the dropwise addition of propargyl bromide (80% wt in toluene, 0.34 g, 2.3 mmol). The mixture was allowed to warm to room temperature and stirred for 12 hours. The mixture was quenched with methanol (3 mL) and extracted using dichloromethane and water. The organic layer was dried over anhydrous magnesium sulfate, filtered, and concentrated by rotary evaporation. The residue was purified by column chromatography over silica gel, eluting with dichloromethane to afford the desired compound as an orange solid upon drying. Yield: 91% 0.53 g  $^1\text{H}$  NMR (500 MHz,  $\text{CDCl}_3$ ),  $\delta$  (ppm): 2.45 (t, 1H); 4.17 (d, 2H); 4.33 (s, 2H); 6.25 (s, 1H); 6.28 (s, 2H).  $^{13}\text{C}$  NMR (125 MHz,  $\text{CDCl}_3$ ),  $\delta$  (ppm): 56.88, 66.17, 75.56, 77.23, 78.98, 109.62, 111.58, 117.79, 119.16, 119.32, 133.43. FAB-MS:  $m/z$  calculated for  $\text{C}_{10}\text{H}_8\text{OS}_4$  [ $\text{M}^+$ ]: 271.9458, found: 271.9486.



## 2-Methoxymethyltetrathiafulvalene



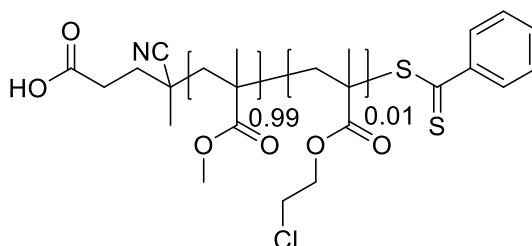
Sodium hydride (0.0143 g, 0.5975 mmol) was added under a nitrogen blanket to a dry, nitrogen-purged flask. The flask was cooled to 0 °C, anhydrous tetrahydrofuran (30 mL) was added and the resulting suspension stirred for 5 minutes. A solution of TTF-OH (0.1000 g, 0.427 mmol) in dry tetrahydrofuran (1 mL) was then added drop-wise, and the solution was stirred for 15 minutes, followed by the drop-wise addition of methyl iodide (133  $\mu$ L, 2.134 mmol). The content of the flask was allowed to warm to room temperature and stirred for 12 hours. The reaction mixture was quenched with 3 mL of methanol, and extracted using dichloromethane/water. The organic fractions were combined and dried over magnesium sulfate, filtered, and brought to dryness by rotary evaporation. The resulting residue was purified by silica flash chromatography, eluting with dichloromethane to afford the desired compound as an orange solid (stored at -20°C, under N<sub>2</sub>). Yield: 82% (0.872 g). <sup>1</sup>H NMR (500 MHz, CDCl<sub>3</sub>),  $\delta$  (ppm): 3.19 (s, 3H); 4.18 (s, 2H); 6.21 (s, 1H); 6.31 (s, 2H).

### **Preparation of chloroethyl-functionalized polymer precursors (P2a-h) via reversible addition-fragmentation chain-transfer polymerization (RAFT).**

2-Chloroethyl methacrylate, methyl methacrylate or butyl methacrylate 4-cyano-4-(phenylcarbonothioylthio)pentanoic acid, azobisisobutyronitrile (AIBN), and anisole were

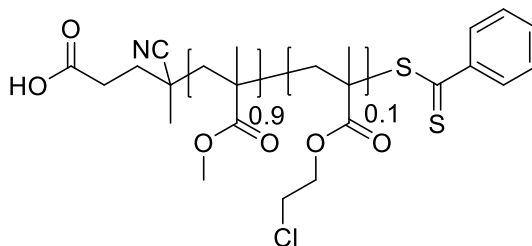
combined in a flask equipped with a septum and degassed for 25 min (N<sub>2</sub> purging). The reaction mixture was immersed in an oil bath preheated to 80 °C. The flask was sealed and the content stirred for 8 hours (ca. 50% monomer conversion was targeted to circumvent any radical transfer by chloroethyl functionalities). The reaction was quenched by immersion in liquid nitrogen, and the mixture precipitated twice in methanol. The resulting pale pink polymers were collected by centrifugation and dried under vacuum.

### PMMA-Cl-co-PMMA (P2a)



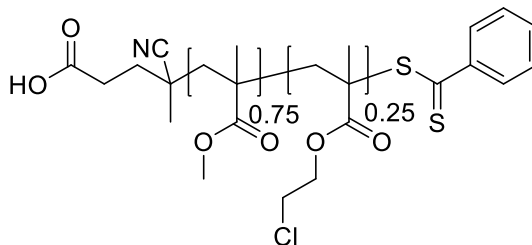
Methyl methacrylate (2.9736 g, 29.700 mmol), 2-chloroethyl methacrylate (0.0446 g, 0.300 mmol), 4-cyano-4-(phenylcarbonothioylthio)pentanoic acid (14.1 mg, 0.0503 mmol), and AIBN (1.7 mg, 0.010 mmol) were added to anisole (6 mL). Monomer conversion by <sup>1</sup>H NMR: 59.4%. Yield of light pink powder: 71%, 1.2640 g. GPC (versus PMMA in THF): M<sub>n</sub> = 35 kDa, PDI = 1.13. <sup>1</sup>H NMR (500 MHz, CDCl<sub>3</sub>), δ (ppm): 0.65-1.48 (m, 6H from methacrylate backbone); 1.56-2.12 (m, 4H from methacrylate backbone); 3.55 (s, 3H from methyl methacrylate pendent group); 3.69 (s, 2H from 2-chloroethylmethacrylate) 4.17 (s, 2H from 2-chloro-ethylmethacrylate pendent group) <sup>13</sup>C NMR (125 MHz, CDCl<sub>3</sub>), δ (ppm): 16.63 (broad), 18.89, 19.14, 41.42, 41.61, 44.71, 45.06, 45.69, 51.99, 54.37 (broad), 54.60 (broad), 64.71, 64.86, 177.14 (broad), 177.29, 177.96 (broad), 178.25 (multiple).

### PMMA-Cl-co-PMMA (P2b)



Methyl methacrylate (2.7032 g, 27.000 mmol), 2-chloroethyl methacrylate (0.4458 g, 3.000 mmol), 4-cyano-4-(phenylcarbonothioylthio)pentanoic acid (14.7 mg, 0.053 mmol), and AIBN (1.7 mg, 0.011 mmol) were added to anisole (6 mL). Monomer conversion by  $^1\text{H}$  NMR: 55.7%. Yield of light pink powder: 76%, 1.3235 g. GPC (versus PMMA in THF):  $M_n = 33$  kDa, PDI = 1.14.  $^1\text{H}$  NMR (500 MHz,  $\text{CDCl}_3$ ),  $\delta$  (ppm): 0.66-1.52 (m, 6H from methacrylate backbone); 1.64-2.11 (m, 4H from methacrylate backbone); 3.58 (s, 3H from methyl methacrylate pendent group); 3.69 (s, 2H from 2-chloro-ethylmethacrylate); 4.20 (s, 2H from 2-chloro-ethylmethacrylate pendent group)  $^{13}\text{C}$  NMR (125 MHz,  $\text{CDCl}_3$ ),  $\delta$  (ppm): 16.62 (broad), 18.85 (multiple), 41.41, 41.59, 44.89 (multiple), 45.69, 51.97, 54.45 (broad), 64.71, 64.86, 176.41, 177.11, 177.27, 177.95, 178.24.

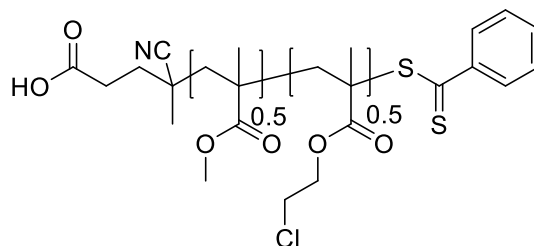
### PMMA-Cl-co-PMMA (P2c)



Methyl methacrylate (2.2527 g, 22.500 mmol), 2-chloroethyl methacrylate (1.1144 g, 7.500 mmol), 4-cyano-4-(phenylcarbonothioylthio)pentanoic acid (15.7 mg, 0.0561

mmol), and AIBN (1.8 mg, 0.011 mmol) were added anisole (6 mL). Monomer conversion by  $^1\text{H NMR}$ : 55.6%. Yield of light pink powder: 69%, 1.2961 g. GPC (versus PMMA in THF):  $M_n = 34$  kDa, PDI = 1.14.  $^1\text{H NMR}$  (500 MHz,  $\text{CDCl}_3$ ),  $\delta$  (ppm): 0.63-1.55 (m, 6H from methacrylate backbone); 1.62-2.19 (m, 4H from methacrylate backbone); 3.58 (s, 3H from methyl methacrylate pendent group); 3.70 (s, 2H from 2-chloro-ethylmethacrylate); 4.20 (s, 2H from 2-chloro-ethylmethacrylate pendent group)  $^{13}\text{C NMR}$  (125 MHz,  $\text{CDCl}_3$ ),  $\delta$  (ppm): 16.64 (broad), 18.88 (multiple), 41.43, 41.61, 44.91 (multiple), 45.70, 51.99, 54.53 (broad), 64.58, 64.76, 64.90, 176.46, 177.12, 177.30, 177.59, 177.96, 178.26, 178.54.

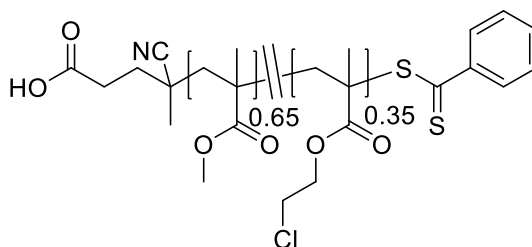
#### PMMA-Cl-co-PMMA (P2d)



Methyl methacrylate (1.5018 g, 15.000 mmol), 2-chloroethyl methacrylate (2.2289 g, 15.000 mmol), 4-cyano-4-(phenylcarbonothioylthio)pentanoic acid (17.4 mg, 0.0622 mmol), and AIBN (2.0 mg, 0.012 mmol) were added to anisole (6 mL). Monomer conversion by  $^1\text{H NMR}$ : 59.3%. Yield of light pink powder: 75%, 1.6670 g. GPC (versus PMMA in THF):  $M_n = 38$  kDa, PDI = 1.19.  $^1\text{H NMR}$  (500 MHz,  $\text{CDCl}_3$ ),  $\delta$  (ppm): 0.67-1.55 (m, 6H from methacrylate backbone); 1.64-2.16 (m, 4H from methacrylate backbone); 3.59 (s, 3H from methyl methacrylate pendent group); 3.71 (s, 2H from 2-chloro-ethylmethacrylate); 4.21 (s, 2H from 2-chloro-ethylmethacrylate pendent group)  $^{13}\text{C NMR}$

(125 MHz, CDCl<sub>3</sub>),  $\delta$  (ppm): 16.64 (broad), 18.83 (multiple), 41.43, 41.61, 44.92 (multiple), 45.52, 52.04, 54.38 (broad), 64.77, 64.581, 64.92, 176.35, 176.54, 177.24, 177.54, 177.87, 178.18.

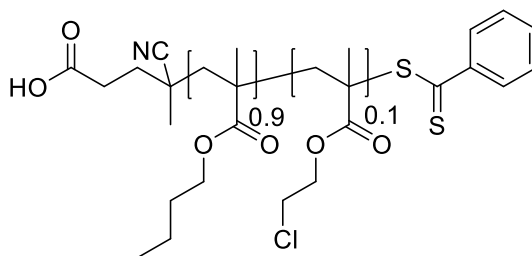
**PMMA-Cl-*block*-PMMA (P2e)**



Methyl methacrylate (3.0036 g, 30.000 mmol), 4-cyano-4-(phenylcarbonothioylthio)pentanoic acid (0.0140 g, 0.050 mmol), and azobisisobutyronitrile (0.0016 g, 0.010 mmol) were combined in a round-bottom flask equipped with a septum and degassed for 25 min (N<sub>2</sub> purging). The reaction mixture was immersed in an oil bath preheated to 80 °C and stirred 2 hours. The reaction was quenched by immersion in liquid nitrogen and precipitated twice in methanol. The resulting pale pink polymer was collected by centrifugation and dried under vacuum. To achieve chain extension, the methacrylate polymer obtained (0.8300 g), 2-chloroethyl methacrylate (1.010 g, 6.800 mmol), AIBN (0.0016 g, 0.010 mmol), and anisole (2 mL) were added to a round-bottom flask (equipped with a septum) and degassed for 25 min (N<sub>2</sub> purging). The flask was immersed in an oil bath preheated to 80 °C and stirred for 2 additional hours, quenched by immersion in liquid nitrogen, and precipitated twice in methanol. The resulting pale pink polymer was collected by centrifugation and dried under vacuum. Monomer conversion by <sup>1</sup>H NMR: poly(methyl methacrylate) block - 29.9%; poly(2-chloroethyl methacrylate) block - 47.7%. Yield: 69%, 0.9520 g. GPC (versus PMMA in

THF):  $M_n = 29$  kDa, PDI = 1.17 (PMMA block:  $M_n = 20.0$  kDa, PDI=1.09).  $^1\text{H}$  NMR (500 MHz,  $\text{CDCl}_3$ ),  $\delta$  (ppm): 0.66-1.58 (m, 6H from methacrylate backbone); 1.63-2.18 (m, 4H from methacrylate backbone); 3.57 (s, 3H from methyl methacrylate pendent group); 3.69 (s, 2H from 2-chloro-ethylmethacrylate); 4.20 (s, 2H from 2-chloro-ethylmethacrylate pendent group)  $^{13}\text{C}$  NMR (125 MHz,  $\text{CDCl}_3$ ),  $\delta$  (ppm): 16.66 (broad), 16.93 (broad), 18.90 (broad), 19.15 (broad), 41.50, 41.66, 44.73 (multiple), 45.04, 45.31, 52.01, 54.37, 54.61, 64.85, 65.00, 176.33 (multiple), 176.53, 177.15, 177.32 (multiple), 177.45 (multiple), 177.99, 178.27 (multiple), 178.58.

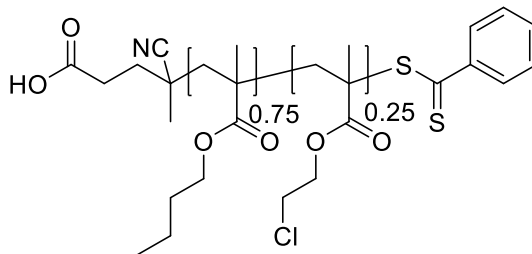
#### PMMA-Cl-co-PBMA (P2f)



Butyl methacrylate (3.8394 g, 27.000 mmol), 2-chloroethyl methacrylate (0.4458 g, 3.00 mmol), 4-cyano-4-(phenylcarbonothioylthio)pentanoic acid (20.0 mg, 0.0714 mmol), and AIBN (2.3 mg, 0.013 mmol) were added to anisole (6 mL). Monomer conversion by  $^1\text{H}$  NMR: 78.2%. Yield of light pink amorphous solid: 84%, 2.0679 g. GPC (versus PMMA in THF):  $M_n = 42$  kDa, PDI = 1.11.  $^1\text{H}$  NMR (500 MHz,  $\text{CDCl}_3$ ),  $\delta$  (ppm): 0.76-1.29 (m, 6H from methacrylate backbone and 3H from butyl pendent group); 1.40 (s, 2H from butyl pendent group); 1.61 (s, 2H from butyl methacrylate pendent group); 1.71-2.11 (m, 4H from methacrylate backbone); 3.69 (s, 2H from 2-chloro-ethylmethacrylate); 3.94 (s, 2H from butyl methacrylate pendent group); 4.19 (s, 2H from 2-chloro-ethylmethacrylate

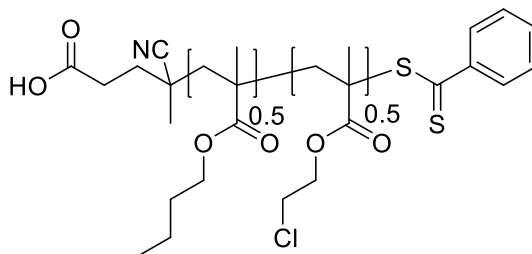
pendent group)  $^{13}\text{C}$  NMR (125 MHz,  $\text{CDCl}_3$ ),  $\delta$  (ppm): 13.91, 16.67 (broad), 18.55 (broad), 19.51, 30.39, 41.43 (multiple), 44.91, 45.30, 52.47 (broad), 54.36 (broad), 64.90 (broad), 177.01 (multiple, broad), 177.70 (multiple, broad), 178.04 (multiple, broad).

**PMMA-Cl-co-PBMA (P2g)**



Butyl methacrylate (3.1995 g, 22.500 mmol), 2-chloroethyl methacrylate (1.1144 g, 7.500 mmol), 4-cyano-4-(phenylcarbonothioylthio)pentanoic acid (20.1 mg, 0.0719 mmol), and AIBN (2.4 mg, 0.014 mmol) were added to anisole (6 mL). Monomer conversion by  $^1\text{H}$  NMR: 73.7%. Yield of light pink amorphous solid: 93%, 2.3173 g. GPC (versus PMMA in THF):  $M_n = 45$  kDa, PDI = 1.15.  $^1\text{H}$  NMR (500 MHz,  $\text{CDCl}_3$ ),  $\delta$  (ppm): 0.78-1.29 (m, 6H from methacrylate backbone and 3H from butyl pendent group); 1.39 (s, 2H from butyl pendent group); 1.61 (s, 2H from butyl methacrylate pendent group); 1.69-2.10 (m, 4H from methacrylate backbone); 3.69 (s, 2H from 2-chloro-ethylmethacrylate); 3.93 (s, 2H from butyl methacrylate pendent group); 4.20 (s, 2H from 2-chloro-ethylmethacrylate pendent group)  $^{13}\text{C}$  NMR (125 MHz,  $\text{CDCl}_3$ ),  $\delta$  (ppm): 13.91, 16.69 (broad), 18.72 (broad), 19.51, 30.39, 41.44 (multiple), 44.95, 45.92, 52.43 (broad), 54.34 (broad), 64.91 (broad), 176.99 (multiple, broad), 177.67 (multiple, broad), 178.04 (multiple, broad).

### PMMA-Cl-co-PBMA (P2h)



Butyl methacrylate (2.1330 g, 15.000 mmol), 2-chloroethyl methacrylate (2.2289 g, 15.000 mmol), 4-cyano-4-(phenylcarbonothioylthio)pentanoic acid (20.3 mg, 0.0727 mmol), and AIBN (2.4 mg, 0.015 mmol) were added to anisole (6 mL). Monomer conversion by  $^1\text{H}$  NMR: 72%. Yield of light pink amorphous solid: 97%, 2.5992 g. GPC (versus PMMA in THF):  $M_n = 40$  kDa, PDI = 1.20.  $^1\text{H}$  NMR (500 MHz,  $\text{CDCl}_3$ ),  $\delta$  (ppm): 0.79-1.30 (m, 6H from methacrylate backbone and 3H from butyl pendent group); 1.36 (s, 2H from butyl pendent group); 1.58 (s, 2H from butyl methacrylate pendent group); 1.72-2.21 (m, 4H from methacrylate backbone); 3.70 (s, 2H from 2-chloro-ethylmethacrylate); 3.94 (s, 2H from butyl methacrylate pendent group); 4.20 (s, 2H from 2-chloro-ethylmethacrylate pendent group)  $^{13}\text{C}$  NMR (125 MHz,  $\text{CDCl}_3$ ),  $\delta$  (ppm): 13.92, 16.80 (broad), 18.80 (multiple), 19.51, 30.37, 30.45, 41.48 (multiple), 44.98, 45.29, 45.92, 52.50 (broad), 54.35 (broad), 64.94 (broad), 176.70 (multiple, broad), 177.24 (multiple, broad).

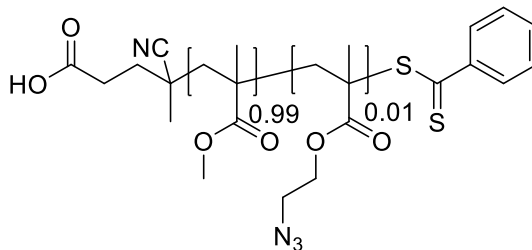
### Preparation of azidoethyl-functionalized polymer precursors (P3a-h).

Chloroethyl-functionalized polymers **P2a-h**, sodium azide, a catalytic amount of 18-crown-6, and N,N-dimethylformamide (DMF) were combined in a 20 mL scintillation vial, stirred at 65 °C for 72 hours, and precipitated in a 1:1 mixture of methanol and water. The resulting powder was collected by centrifugation, washed with methanol, dried, and



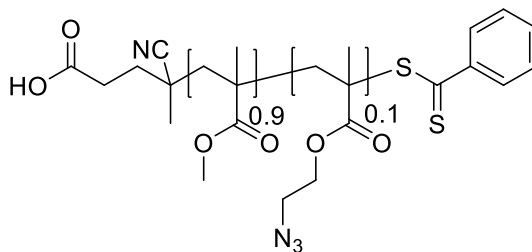
redissolved in chloroform (3 mL). The solution obtained was reprecipitated in a 1:1 mixture of methanol and water. The resulting white solid was collected by centrifugation and dried under vacuum.

### PMMA-N<sub>3</sub>-co-PMMA (P3a)



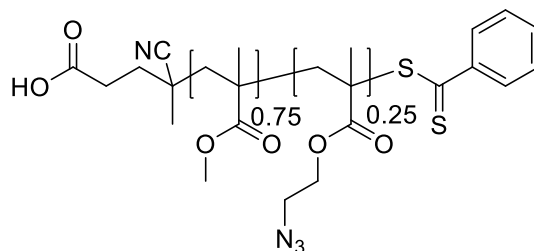
**P2a** (0.1500 g), sodium azide (0.5000 g, 7.700 mmol), and 18-crown-6 (2 mg, 0.0139 mmol) were added to DMF (8 mL). Yield: 69%, 0.1047 g. GPC (versus PMMA in THF): Mn = 37 kDa, PDI = 1.15. <sup>1</sup>H NMR (500 MHz, CDCl<sub>3</sub>), δ (ppm): 0.71-1.51 (m, 6H from methacrylate backbone); 1.74-2.10 (m, 4H from methacrylate backbone); 3.50 (s, 2H from 2-azido-ethylmethacrylate); 3.60 (s, 3H from methyl methacrylate pendent group); 4.11 (s, 2H from 2-azido-ethylmethacrylate pendent group) <sup>13</sup>C NMR (125 MHz, CDCl<sub>3</sub>), δ (ppm): 16.48 (broad), 18.73, 18.97, 44.56, 44.89, 51.87, 53.43 (broad), 54.22 (broad), 54.43 (broad), 63.80, 176.18, 176.30, 176.99, 177.15, 177.81, 178.10 (multiple), 178.39, 178.43.

### PMMA-N<sub>3</sub>-co-PMMA (P3b)



**P2b** (0.1500 g), sodium azide (0.5000 g, 7.700 mmol), and 18-crown-6 (2 mg, 0.0139 mmol) were added to DMF (8 mL). Yield: 75%, 0.1120 g. GPC (versus PMMA in THF):  $M_n = 37$  kDa, PDI = 1.18.  $^1\text{H}$  NMR (500 MHz,  $\text{CDCl}_3$ ),  $\delta$  (ppm): 0.70-1.53 (m, 6H from methacrylate backbone); 1.56-2.15 (m, 4H from methacrylate backbone); 3.49 (s, 2H from 2-azido-ethylmethacrylate); 3.59 (s, 3H from methyl methacrylate pendent group); 4.11 (s, 2H from 2-azido-ethylmethacrylate pendent group)  $^{13}\text{C}$  NMR (125 MHz,  $\text{CDCl}_3$ ),  $\delta$  (ppm): 16.65 (broad), 18.89 (multiple), 44.71, 44.87, 45.05, 45.20, 49.67 (multiple), 49.81, 51.99 (multiple), 52.71 (broad), 54.47 (broad), 63.81, 63.96, 176.48 (multiple, broad), 177.14, 177.31 (multiple, broad), 177.96 (multiple), 178.26 (multiple).

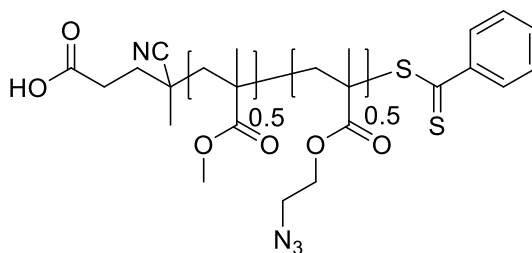
**PMMA-N<sub>3</sub>-co-PMMA (P3c)**



**P2c** (0.1500 g), sodium azide (0.5000 g, 7.700 mmol), and 18-crown-6 (2 mg, 0.0139 mmol) were added to DMF (8 mL). Yield: 70%, 0.1039 g. GPC (versus PMMA in THF):  $M_n = 37$  kDa, PDI = 1.20.  $^1\text{H}$  NMR (500 MHz,  $\text{CDCl}_3$ ),  $\delta$  (ppm): 0.70-1.54 (m, 6H from methacrylate backbone); 1.60-2.21 (m, 4H from methacrylate backbone); 3.49 (s, 2H from 2-azido-ethylmethacrylate); 3.59 (s, 3H from methyl methacrylate pendent group); 4.11 (s, 2H from 2-azido-ethylmethacrylate pendent group)  $^{13}\text{C}$  NMR (125 MHz,  $\text{CDCl}_3$ ),  $\delta$  (ppm): 16.68 (broad), 18.89 (multiple), 44.71, 44.90, 45.05, 45.20, 49.65 (multiple), 49.78, 51.99

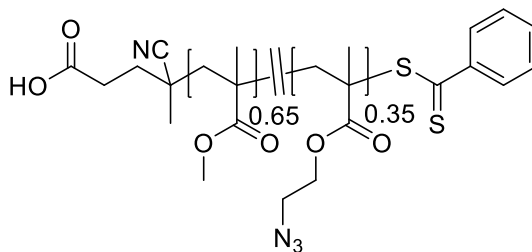
(multiple), 52.71 (broad), 54.37 (broad), 63.90 (multiple), 176.46 (broad), 177.12, 177.26, 177.34, 177.64, 177.95 (multiple), 178.25.

### PMMA-N<sub>3</sub>-*co*-PMMA (P3d)



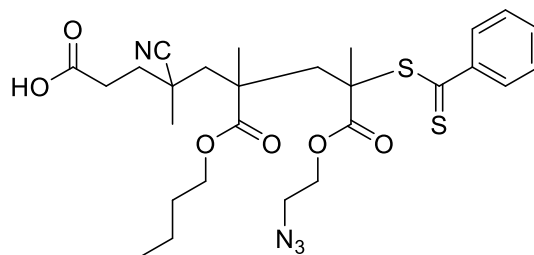
**P2d** (0.1500 g), sodium azide (0.5000 g, 7.700 mmol), and 18-crown-6 (2 mg, 0.0139 mmol) were added to DMF (8 mL). Yield: 75%, 0.1128 g. GPC (versus PMMA in THF): M<sub>n</sub> = 43 kDa, PDI = 1.26. <sup>1</sup>H NMR (500 MHz, CDCl<sub>3</sub>), δ (ppm): 0.73-1.52 (m, 6H from methacrylate backbone); 1.78-2.21 (m, 4H from methacrylate backbone); 3.50 (s, 2H from 2-azido-ethylmethacrylate); 3.60 (s, 3H from methyl methacrylate pendent group); 4.12 (s, 2H from 2-azido-ethylmethacrylate pendent group) <sup>13</sup>C NMR (125 MHz, CDCl<sub>3</sub>), δ (ppm): 16.81 (broad), 18.99 (multiple), 44.78, 44.95, 45.09, 45.25, 49.68 (multiple), 49.81, 52.07 (multiple), 52.79 (broad), 54.33 (broad), 64.01 (multiple), 176.43, 177.29, 177.63, 177.89, 178.23.

### PMMA-N<sub>3</sub>-*block*-PMMA (P3e)



**P2e** (0.1500 g), sodium azide (0.5000 g, 7.700 mmol), and 18-crown-6 (2 mg, 0.0139 mmol) were added to DMF (8 mL). Yield: 66%, 0.0986 g. GPC (versus PMMA in THF):  $M_n = 36$  kDa, PDI = 1.16.  $^1\text{H}$  NMR (500 MHz,  $\text{CDCl}_3$ ),  $\delta$  (ppm): 0.67-1.56 (m, 6H from methacrylate backbone); 1.74-2.27 (m, 4H from methacrylate backbone); 3.50 (s, 2H from 2-azido-ethylmethacrylate); 3.59 (s, 3H from methyl methacrylate pendent group); 4.12 (s, 2H from 2-azido-ethylmethacrylate pendent group)  $^{13}\text{C}$  NMR (125 MHz,  $\text{CDCl}_3$ ),  $\delta$  (ppm): 16.62, 17.07, 18.88, 19.03, 44.70, 44.91, 45.04, 45.24, 49.61 (multiple), 49.73, 51.98 (multiple), 52.74 (broad), 54.33, 54.58, 63.88, 64.02, 176.25 (multiple), 176.46, 177.12 (multiple), 177.29, 177.42 (multiple), 177.96 (multiple), 178.25 (multiple).

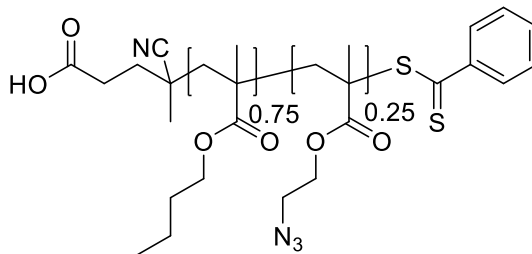
**PMMA-N<sub>3</sub>-co-PBMA (P3f)**



**P2f** (0.1500 g), sodium azide (0.5000 g, 7.700 mmol), and 18-crown-6 (2 mg, 0.0139 mmol) were added to DMF (8 mL). Yield: 73%, 0.1095 g. GPC (versus PMMA in THF):  $M_n = 46$  kDa, PDI = 1.15.  $^1\text{H}$  NMR (500 MHz,  $\text{CDCl}_3$ ),  $\delta$  (ppm): 0.79-1.30 (m, 6H from methacrylate backbone and 3H from butyl pendent group); 1.38 (s, 2H from butyl pendent group); 1.60 (s, 2H from butyl methacrylate pendent group); 1.76-2.09 (m, 4H from methacrylate backbone); 3.47 (s, 2H from 2-azido-ethylmethacrylate); 3.93 (s, 2H from butyl methacrylate pendent group); 4.09 (s, 2H from 2-azido-ethylmethacrylate pendent group)  $^{13}\text{C}$  NMR (125 MHz,  $\text{CDCl}_3$ ),  $\delta$  (ppm): 13.90 (multiple), 16.86 (broad), 18.65

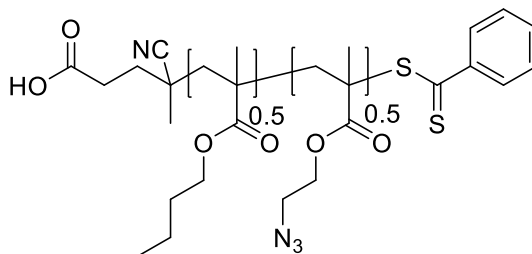
(broad), 19.01 (broad) 19.45, 30.36 (multiple), 44.94, 45.26, 45.91, 49.66, 49.79, 52.54 (broad), 54.34 (broad), 63.81 (broad), 64.93 (broad), 177.51 (multiple, broad), 177.51 (multiple, broad).

### PMMA-N<sub>3</sub>-co-PBMA (P3g)



**P2g** (0.1500 g), sodium azide (0.5000 g, 7.700 mmol), and 18-crown-6 (2 mg, 0.0139 mmol) were added to DMF (8 mL). Yield: 73%, 0.1095 g. GPC (versus PMMA in THF):  $M_n = 48$  kDa, PDI = 1.23.  $^1\text{H}$  NMR (500 MHz,  $\text{CDCl}_3$ ),  $\delta$  (ppm): 0.73-1.30 (m, 6H from methacrylate backbone and 3H from butyl pendent group); 1.38 (s, 2H from butyl pendent group); 1.59 (s, 2H from butyl methacrylate pendent group); 1.71-2.11 (m, 4H from methacrylate backbone); 3.47 (s, 2H from 2-azido-ethylmethacrylate); 3.92 (s, 2H from butyl methacrylate pendent group); 4.09 (s, 2H from 2-azido-ethylmethacrylate pendent group)  $^{13}\text{C}$  NMR (125 MHz,  $\text{CDCl}_3$ ),  $\delta$  (ppm): 13.89 (multiple), 16.68 (broad), 18.58 (broad), 19.50, 30.37 (multiple), 44.90, 45.27, 45.92, 49.64, 49.77, 52.71 (broad), 54.31 (broad), 63.84 (broad), 65.03 (broad), 176.76, 176.96, 177.41, 177.53, 177.69 (multiple), 178.02.

### PMMA-N<sub>3</sub>-co-PBMA (P3h)



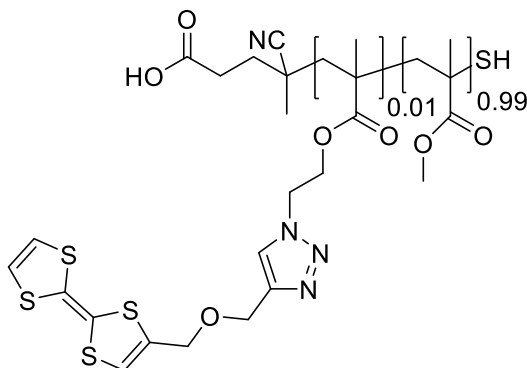
**P2h** (0.1500 g), sodium azide (0.5000 g, 7.700 mmol), and 18-crown-6 (2 mg, 0.0139 mmol) were added to DMF (8 mL). Yield: 76%, 0.1140 g. GPC (versus PMMA in THF): Mn = 49 kDa, PDI = 1.28. <sup>1</sup>H NMR (500 MHz, CDCl<sub>3</sub>), δ (ppm): 0.73-1.30 (m, 6H from methacrylate backbone and 3H from butyl pendent group); 1.38 (s, 2H from butyl pendent group); 1.59 (s, 2H from butyl methacrylate pendent group); 1.70-2.10 (m, 4H from methacrylate backbone); 3.47 (s, 2H from 2-azido-ethylmethacrylate); 3.92 (s, 2H from butyl methacrylate pendent group); 4.09 (s, 2H from 2-azido-ethylmethacrylate pendent group) <sup>13</sup>C NMR (125 MHz, CDCl<sub>3</sub>), δ (ppm): 13.89 (multiple), 16.66 (broad), 18.53 (broad), 19.50, 30.41 (multiple), 44.91, 45.27, 45.91, 49.67, 49.79, 52.60 (broad), 54.32 (broad), 63.78 (broad), 64.89 (broad), 176.98, 177.15, 177.52, 177.68 (multiple), 178.03 (multiple, broad).

### Preparation of TTF-containing polymers P4a-h via “click” chemistry

Polymers **P3a-h**, 2-propargyloxymethyltetrahydrofulvalene, N,N,N',N'',N''-pentamethyldiethylenetriamine, and tetrahydrofuran, were combined in a round bottom flask and degassed for 20 min (N<sub>2</sub> purging). Under a nitrogen blanket, copper(I) bromide was added, and the solution degassed for additional 20 min. The reaction mixture was stirred at 40 °C for 4 h (FT-IR control: disappearance of the azide stretch at 2140 cm<sup>-1</sup>).

The solution was precipitated in hexanes, centrifuged, dissolved in THF, and passed through a short basic alumina column into another solution of hexanes. The resulting yellow powder was collected by centrifugation and dried under reduced pressure.

### PolyTTFMMA-1 (P4a)

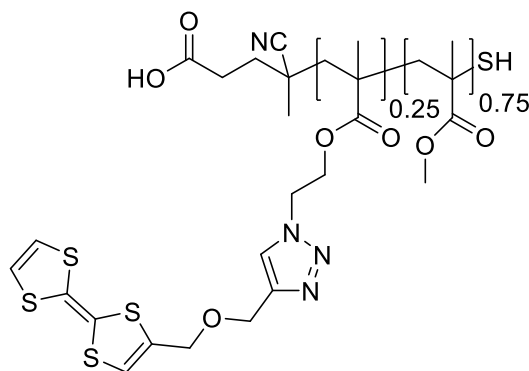


**P3a** (0.1453 g), **6** (0.0047 g, 0.020 mmol), copper (I) bromide (0.0020 g, 0.0139 mmol), and N,N,N',N'',N'''-pentamethyldiethylenetriamine (20  $\mu$ L, 0.0166 g, 0.096 mmol) were added to tetrahydrofuran (6 mL). Yield: 63%, 0.0945 g. GPC (versus PMMA in THF):  $M_n$  = 36 kDa, PDI = 1.14.  $^1\text{H}$  NMR (500 MHz,  $\text{CDCl}_3$ ),  $\delta$  (ppm): 0.66-2.10 (m, 10H from methacrylate backbone); 3.59 (s, 3H from methyl methacrylate pendent group); 4.35 (m, 2H from methylene adjacent to TTF group and 2H from ethylmethacrylate pendent group); 4.63 (s, 2H from ethylmethacrylate pendent group); 4.72 (2H from propargyl methylene); 6.33 (3H aryl protons from TTF moiety); 7.68-7.78 (m, 1H from triazole ring)  $^{13}\text{C}$  NMR (125 MHz,  $\text{CDCl}_3$ ),  $\delta$  (ppm): 16.65, 18.92, 19.18, 29.71, 44.74, 45.08, 52.01, 52.89, 53.62, 54.41, 54.63, 63.35, 67.37, 117.27, 119.27, 119.36, 123.78, 134.18, 145.09, 177.18, 177.33, 177.99 (multiple) 178.28 (multiple), 178.57.



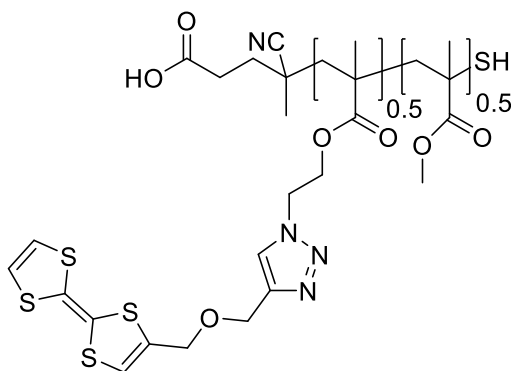


### PolyTTFMMA-25 (P4c)



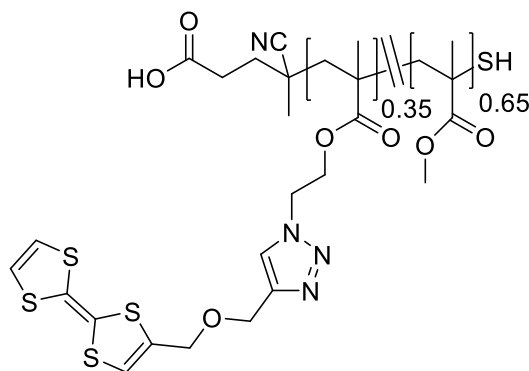
**P3c** (0.0874 g), **6** (0.0626 g, 0.267 mmol), copper (I) bromide (0.0020 g, 0.0139 mmol), and N,N,N',N'',N'''-pentamethyldiethylenetriamine (20  $\mu$ L, 0.0166 g, 0.096 mmol) were added to tetrahydrofuran (6 mL). Yield: 79%, 0.1103 g. GPC (versus PMMA in THF): Mn = 31 kDa, PDI = 1.28.  $^1\text{H}$  NMR (500 MHz,  $\text{CDCl}_3$ ),  $\delta$  (ppm): 0.41-2.19 (m, 10H from methacrylate backbone); 3.59 (s, 3H from methyl methacrylate pendent group); 4.34 (m, 2H from methylene adjacent to TTF group and 2H from ethylmethacrylate pendent group); 4.67 (m, 2H from ethylmethacrylate pendent group and 2H from propargyl methylene); 6.33 (3H aryl protons from TTF moiety); 7.69-7.87 (m, 1H from triazole ring)  $^{13}\text{C}$  NMR (125 MHz,  $\text{CDCl}_3$ ),  $\delta$  (ppm): 13.93, 13.97, (broad), 19.53, 30.41, 30.49, 44.93, 45.32, 48.77, 49.95, 54.36, 54.81 63.25 (multiple), 64.94 (multiple), 67.31, 109.91, 111.21, 117.19, 119.22, 119.37, 123.83, 134.20, 144.92, 145.06, 176.98, 177.49, 177.73 (multiple) 178.06 (multiple).

### PolyTTFMMA-50 (P4d)



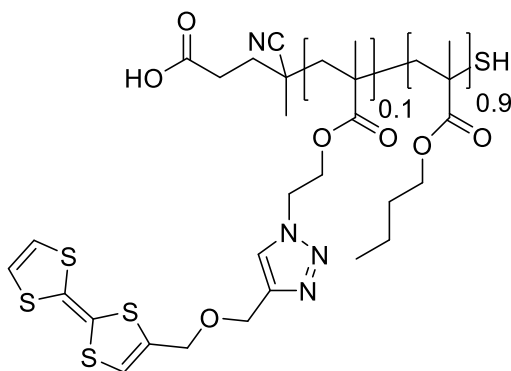
**P3d** (0.0658 g), **6** (0.0842 g, 0.359 mmol), copper (I) bromide (0.0020 g, 0.0139 mmol), and N,N,N',N'',N'''-pentamethyldiethylenetriamine (20  $\mu$ L, 0.0166 g, 0.096 mmol) were added to tetrahydrofuran (6 mL). Yield: 60%, 0.0816 g. GPC (versus PMMA in THF):  $M_n$  = 20 kDa, PDI = 1.29.  $^1\text{H}$  NMR (500 MHz,  $\text{CDCl}_3$ ),  $\delta$  (ppm): 0.69-1.32 (m, 6H from methacrylate backbone and 3H from butyl pendent group); 1.39 (s, 2H from butyl pendent group); 1.60 (s, 2H from butyl methacrylate pendent group); 1.66-2.05 (m, 4H from methacrylate backbone); 3.93 (s, 2H from butyl methacrylate pendent group); 4.34 (m, 2H from methylene adjacent to TTF group and 2H from ethylmethacrylate pendent group); 4.67 (m, 2H from ethylmethacrylate pendent group and 2H from propargyl methylene); 6.33 (3H aryl protons from TTF moiety); 7.69-7.87 (m, 1H from triazole ring)  $^{13}\text{C}$  NMR (125 MHz,  $\text{CDCl}_3$ ),  $\delta$  (ppm): 13.91, 13.97, (broad), 19.51, 30.40, 30.53, 44.98, 45.35, 48.74, 49.93, 54.37, 54.77 63.30 (multiple), 64.99 (multiple), 67.35, 109.96, 111.27, 117.18, 119.19, 119.44, 123.87, 134.33, 144.93, 145.02, 176.98, 177.48, 177.66 (multiple) 178.10 (multiple).

### PolyTTF-*block*-MMA-35 (P4e)



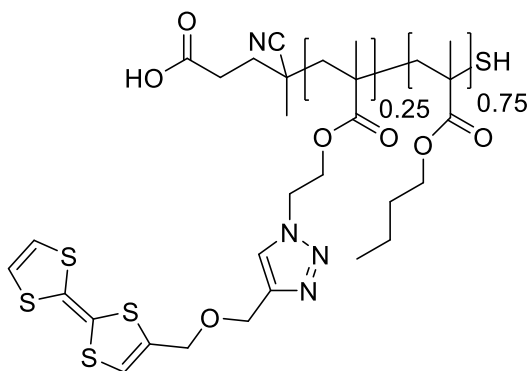
**P4e** (0.0500 g), **6** (0.0502 g, 0.214 mmol), copper (I) bromide (0.0020 g, 0.0139 mmol), and N,N,N',N'',N'''-pentamethyldiethylenetriamine (20  $\mu$ L, 0.0166 g, 0.096 mmol) were added to tetrahydrofuran (4 mL). Yield: 57%, 0.0523 g. GPC (versus PMMA in THF):  $M_n$  = 19 kDa, PDI = 1.14.  $^1\text{H}$  NMR (500 MHz,  $\text{CDCl}_3$ ),  $\delta$  (ppm): 0.42-2.11 (m, 10H from methacrylate backbone); 3.59 (s, 3H from methyl methacrylate pendent group); 4.32 (broad, m, 2H from methylene adjacent to TTF group and 2H from ethylmethacrylate pendent group); 4.66 (broad, m, 2H from ethylmethacrylate pendent group and 2H from propargyl methylene); 6.33 (3H aryl protons from TTF moiety); 7.86 (broad), 1H from triazole ring)  $^{13}\text{C}$  NMR (125 MHz,  $\text{CDCl}_3$ ),  $\delta$  (ppm): 16.70, 18.92, 19.53, 44.76, 45.03 (multiple), 54.40, 54.63, 63.25 (multiple), 64.94 (multiple), 67.31, 109.91, 111.21, 117.19, 119.22, 119.37, 123.83, 134.20, 144.92, 145.06, 177.20, 177.35, 178.02 (multiple) 178.31 (multiple).

## PolyTTFBMA-10 (9f)



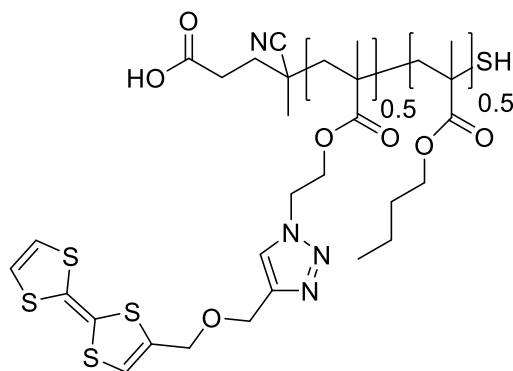
**P3f** (0.1222 g), **6** (0.0278 g, 0.119 mmol), copper (I) bromide (0.0020 g, 0.0139 mmol), and N,N,N',N'',N'''-pentamethyldiethylenetriamine (20  $\mu$ L, 0.0166 g, 0.096 mmol) were added to tetrahydrofuran (6 mL). Yield: 50%, 0.0737 g. GPC (versus PMMA in THF):  $M_n$  = 47 kDa, PDI = 1.17.  $^1\text{H}$  NMR (500 MHz,  $\text{CDCl}_3$ ),  $\delta$  (ppm): 0.69-1.32 (m, 6H from methacrylate backbone and 3H from butyl pendent group); 1.39 (s, 2H from butyl pendent group); 1.60 (s, 2H from butyl methacrylate pendent group); 1.66-2.05 (m, 4H from methacrylate backbone); 3.93 (s, 2H from butyl methacrylate pendent group); 4.33 (s, 2H from methylene adjacent to TTF group); 4.35 (broad s, 2H from ethylmethacrylate pendent group); 4.63 (s, 2H from ethylmethacrylate pendent group); 4.71 (s, 2H from propargyl methylene); 6.33 (3H aryl protons from TTF moiety); 7.68-7.86 (m, 1H from triazole ring)  $^{13}\text{C}$  NMR (125 MHz,  $\text{CDCl}_3$ ),  $\delta$  (ppm): 13.93, 13.97, (broad), 19.53, 30.41, 30.49, 44.93, 45.32, 48.77, 49.95, 54.36, 54.81 63.25 (multiple), 64.94 (multiple), 67.31, 109.91, 111.21, 117.19, 119.22, 119.37, 123.83, 134.20, 144.92, 145.06, 176.98, 177.49, 177.73 (multiple) 178.06 (multiple).

### PolyTTFBMA-25 (P4g)



**P3g** (0.0961 g), **6** (0.0539 g, 0.230 mmol), copper (I) bromide (0.0020 g, 0.0139 mmol), and N,N,N',N'',N'''-pentamethyldiethylenetriamine (20  $\mu$ L, 0.0166 g, 0.096 mmol) were added to tetrahydrofuran (6 mL). Yield: 75%, 0.1058 g. GPC (versus PMMA in THF):  $M_n$  = 51 kDa, PDI = 1.23.  $^1\text{H}$  NMR (500 MHz,  $\text{CDCl}_3$ ),  $\delta$  (ppm): 0.43-1.28 (m, 6H from methacrylate backbone and 3H from butyl pendent group); 1.39 (s, 2H from butyl pendent group); 1.60 (s, 2H from butyl methacrylate pendent group); 1.70-2.13 (m, 4H from methacrylate backbone); 3.93 (s, 2H from butyl methacrylate pendent group); 4.33 (s, 2H from methylene adjacent to TTF group); 4.37 (broad s, 2H from ethylmethacrylate pendent group); 4.65 (s, 2H from ethylmethacrylate pendent group); 4.69 (s, 2H from propargyl methylene); 6.33 (3H aryl protons from TTF moiety); 7.69-7.89 (m, 1H from triazole ring)  $^{13}\text{C}$  NMR (125 MHz,  $\text{CDCl}_3$ ),  $\delta$  (ppm): 14.00 (broad), 19.56, 30.42, 30.50, 44.94, 45.31, 48.81, 54.40, 63.31 (multiple), 65.07 (multiple), 67.33, 109.86, 111.27, 117.31, 119.37, 123.95, 134.22, 144.96, 177.75 (multiple).

### PolyTTFBMA-50 (9h)

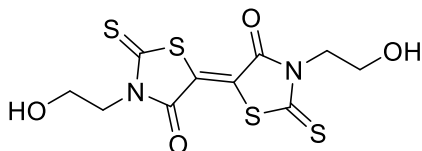


**P3h** (0.0715 g), **6** (0.0785 g, 0.335 mmol), copper (I) bromide (0.0020 g, 0.0139 mmol), and N,N,N',N'',N'''-pentamethyldiethylenetriamine (20  $\mu$ L, 0.0166 g, 0.096 mmol) were added to tetrahydrofuran (6 mL). Yield: 86%, 0.1177 g. GPC (versus PMMA in THF):  $M_n$  = 42 kDa, PDI = 1.27.  $^1\text{H}$  NMR (500 MHz,  $\text{CDCl}_3$ ),  $\delta$  (ppm): 0.39-1.29 (m, 6H from methacrylate backbone and 3H from butyl pendent group); 1.38 (s, 2H from butyl pendent group); 1.59 (s, 2H from butyl methacrylate pendent group); 1.70-2.09 (m, 4H from methacrylate backbone); 3.92 (s, 2H from butyl methacrylate pendent group); 4.32 (s, 2H from methylene adjacent to TTF group); 4.37 (broad s, 2H from ethylmethacrylate pendent group); 4.68 (m, 2H from ethylmethacrylate pendent group, 2H from propargyl methylene); 6.33 (3H aryl protons from TTF moiety); 7.68-7.91 (m, 1H from triazole ring)  $^{13}\text{C}$  NMR (125 MHz,  $\text{CDCl}_3$ ),  $\delta$  (ppm): 14.04 (broad), 19.56, 30.41, 30.49, 44.90, 45.22, 48.79, 54.31, 63.36 (multiple), 65.13, 67.39, 109.83, 111.32, 117.40, 119.44, 124.11, 134.23, 144.83, 176.12 (multiple, broad), 177.20 (multiple, broad).

### General procedure for the synthesis of ((*E*)-3,3'-substituted-5,5'-bithiazolidinylidene-4,4'-dione)<sup>3</sup>

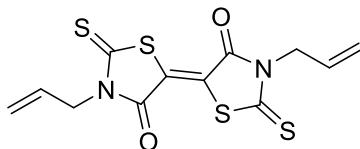
To a 20 mL scintillation vial, chilled to 0 °C in an ice bath, was added amine (2 eq.) in DMF. Carbon disulfide (2 eq.) was added dropwise (very exothermic) and the now yellow/orange solution was stirred for 10 minutes. Dimethylacetylene dicarboxylate (1 eq.) was then added dropwise, the now dark red/black solution was stirred for an additional 10 minutes. The solution was precipitated in an excess of methanol:water (1:1) to yield an orange crystalline precipitate. The orange solid was collected by vacuum filtration and dried under vacuum to give the product.

### Synthesis of BT-diol



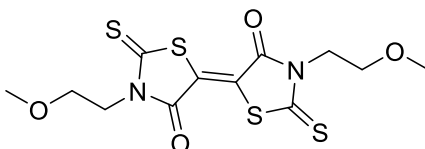
Yield: 40% <sup>1</sup>H NMR (500 MHz, DMSO) δ: 4.92 (t, *J* = 6.1 Hz, 1H), 4.12 (s, 2H), 3.66 (q, *J* = 6.0 Hz, 2H). <sup>13</sup>C NMR (126 MHz, DMSO) δ: 195.57, 166.77, 124.02, 56.66, 46.73. ESI-MS: calculated for C<sub>10</sub>H<sub>10</sub>N<sub>2</sub>O<sub>2</sub>S<sub>4</sub> [M<sup>+</sup>]: 348.9451 g/mol, found: 348.9420. FT-IR ν(cm<sup>-1</sup>) 3100-3500 (b, -OH), 2966-2822 (w, alkyl C-H), 1687,1703 (s, C=O), 1254 (m, C=S), 1067 (m, -N-C=S)

### Synthesis of allyl-BT



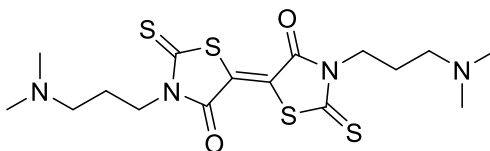
Yield: 46%, <sup>1</sup>H NMR (400 MHz, DMSO) δ: 5.83 (ddt, *J* = 17.0, 10.5, 5.2 Hz, 1H), 5.29 – 5.05 (m, 2H), 4.64 (d, *J* = 5.2 Hz, 2H). <sup>13</sup>C NMR (101 MHz, DMSO) δ: 195.39, 166.74, 130.32, 124.75, 118.71, 46.64. ESI-MS: calculated for C<sub>12</sub>H<sub>10</sub>N<sub>2</sub>O<sub>2</sub>S<sub>4</sub> [M<sup>+</sup>]: 341.9631 g/mol, found: 341.9681. FT-IR ν(cm<sup>-1</sup>) 2989-2990 (w, alkyl C-H), 3090-3000 (m, allyl C-H), 1695,1675 (s, C=O), 1640 (w, C=C), 1289 (m, C=S), 1025 (m, N-C=S).

### Synthesis of methoxyethyl-BT



Yield: 50%, <sup>1</sup>H NMR (500 MHz, CDCl<sub>3</sub>) δ: 4.35 (t, *J* = 5.6 Hz, 2H), 3.69 (t, *J* = 5.6 Hz, 2H), 3.33 (s, 3H). <sup>13</sup>C NMR (126 MHz, CDCl<sub>3</sub>) δ 194.87, 167.10, 124.86, 68.22, 59.07, 43.79. ESI-MS: calculated for C<sub>12</sub>H<sub>14</sub>N<sub>2</sub>O<sub>4</sub>S<sub>4</sub> [M<sup>+</sup>]: 377.98 g/mol, found [M+Na]: 400.973. FT-IR ν(cm<sup>-1</sup>) 2995-2784 (w, alkyl C-H), 1687 (s, C=O), 1271 (m, C=S), 1060 (m, N-C=S)

### Synthesis of dimethylamino-BT (DMABT)



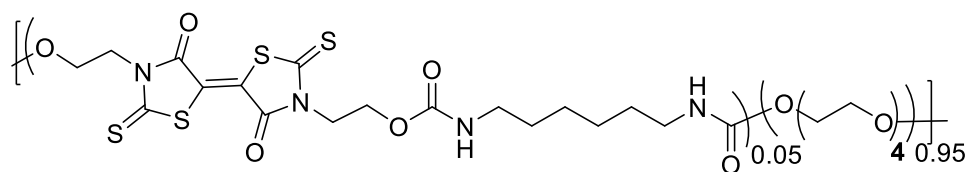


Yield: 35%,  $^1\text{H}$  NMR (500 MHz,  $\text{CDCl}_3$ )  $\delta$ : 4.20 (t,  $J = 7$  Hz, 2H), 2.37 (t,  $J = 7$  Hz, 2H), 2.19 (s, 6H), 1.87 (p,  $J = 7$  Hz, 2H).  $^{13}\text{C}$  NMR (126 MHz,  $\text{CDCl}_3$ )  $\delta$ : 194.69, 167.10, 124.76, 56.98, 45.50, 43.43, 24.71. ESI-MS: calculated for  $\text{C}_{16}\text{H}_{24}\text{N}_4\text{O}_2\text{S}_4$   $[\text{M}^+]$ : 432.08 g/mol, found  $[\text{M}+\text{H}]$ : 433.085. FT-IR  $\nu(\text{cm}^{-1})$  2985-2677 (m, alkyl C-H), 1691 (s, C=O), 1253 (m, C=S), 1073 (m, N-C=S).

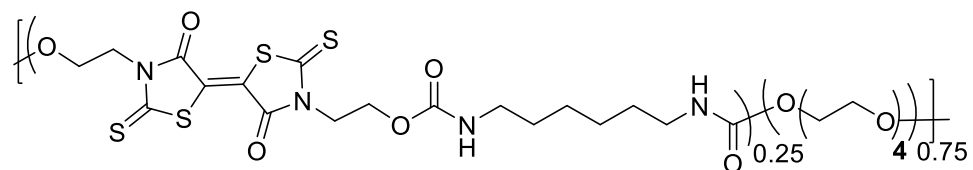
### General procedure for the synthesis of polyurethanes (P5a-c)

To a flame-dried 25 mL round-bottomed flask went BT-diol and tetraethyleneglycol in DMSO. DBDTL and HMDI were added quickly and the mixture stirred at 40 °C for 48 hours. The viscous polymer solution was precipitated into methanol and collected by filtration to yield orange fibers. Further purification by dialysis was performed in THF using 3500 Da molecular weight cutoff dialysis membranes. The THF solutions were again precipitated in methanol, collected by vacuum filtration and dried overnight under vacuum.

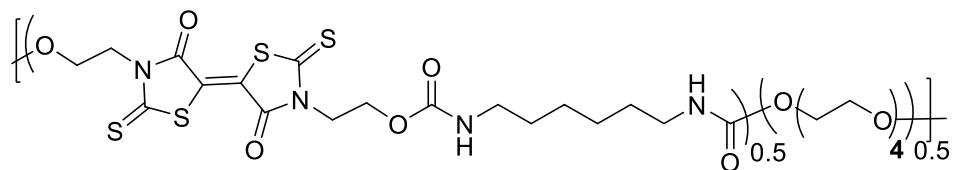
### P5a



Yield: 90%  $^1\text{H}$  NMR (500 MHz, DMSO)  $\delta$  (ppm) 7.15-7.17 (m), 4.25 (s), 4.02-4.04 (t), 3.54-3.56 (t), 3.51 (s), 2.94 (q), 1.3-1.4 (m), 1.15-1.25 (m).  $^{13}\text{C}$  NMR (126 MHz, DMSO)  $\delta$  (ppm) 195.20, 166.59, 156.15, 156.09, 123.88, 69.79, 69.72, 68.92, 63.18, 60.23, 44.22, 40.74, 29.38, 25.97. FT-IR  $\nu(\text{cm}^{-1})$  3321 (s, urethane N-H), 2988-2788 (s, alkyl C-H), 1682 (s, urethane C=O), 1250 (m, C=S), 1053 (m, N-C=S).

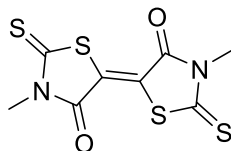
**P5b**

Yield: 86%,  $^1\text{H}$  NMR (500 MHz, DMSO)  $\delta$  (ppm) 7.15-7.17 (m), 7.08 (t), 4.20-4.30 (s), 4.02-4.05 (t), 3.53-3.57 (t), 3.51 (s), 2.94 (q), 2.88 (q), 1.3-1.4 (m), 1.16-1.25 (m).  $^{13}\text{C}$  NMR (126 MHz, DMSO)  $\delta$  (ppm) 195.59, 167.03, 156.59, 156.23, 124.33, 70.25, 70.18, 69.38, 63.44, 59.93, 44.66, 40.62, 29.83, 26.42. FT-IR  $\nu(\text{cm}^{-1})$  3320 (m, urethane N-H), 2988-2796 (m, alkyl C-H), 1685 (s, urethane C=O), 1253 (m, C=S), 1054 (m, -N-C=S).

**P5c**

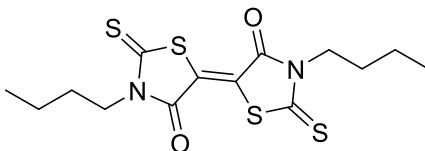
Yield: 84%,  $^1\text{H}$  NMR (500 MHz, DMSO)  $\delta$  (ppm) 7.15-7.20 (m), 7.08 (m), 4.20-4.30 (s), 4.02-4.10 (m), 3.53-3.57 (m), 3.48 (s), 2.90-3.00 (m), 2.80-2.90 (m), 1.3-1.4 (m), 1.16-1.25 (m).  $^{13}\text{C}$  NMR (126 MHz, DMSO)  $\delta$  (ppm) 195.59, 173.80, 167.03, 156.59, 156.22, 124.34, 70.25, 70.18, 69.38, 63.44, 59.93, 44.58, 40.64, 29.83, 26.43. FT-IR  $\nu(\text{cm}^{-1})$  3331 (m, broad, urethane N-H), 2983-2814 (m, alkyl C-H), 1690 (s, urethane C=O), 1250 (m, C=S), 1052 (m, N-C=S).

### Synthesis of ((*E*)-3,3'-methyl-5,5'-bithiazolidinylidene-4,4'-dione) (methyl-BT)



To a 20 mL scintillation vial, chilled to 0° C in an ice bath, was added methylamine (2 eq.) in DMF. Carbon disulfide (2 eq.) was added dropwise and the resulting yellow/orange solution was stirred for 10 minutes. Dimethylacetylene dicarboxylate (1 eq.) was then added dropwise and the dark solution was stirred for an additional 10 minutes. The solution was then placed in the refrigerator and allowed to stand overnight. Red crystals precipitated from the solution and were collected by vacuum filtration and washed with methanol. The solid was dried under vacuum overnight to give the product in 30% yield (1.1 g). <sup>1</sup>H NMR (500 MHz, DMSO) δ: 3.54 (s) <sup>13</sup>C NMR (126 MHz, CDCl<sub>3</sub>) δ 194.71, 193.99, 187.45, 166.98, 160.41, 129.25, 125.02, 51.70, 32.08, 31.81, 31.25. \*\* Peak doubling in the <sup>13</sup>C NMR was observed (potentially representing E/Z isomers). Mass spectroscopy confirms a single molecular ion peak. ESI-MS: calculated for C<sub>12</sub>H<sub>10</sub>N<sub>2</sub>O<sub>2</sub>S<sub>4</sub> [M<sup>+</sup>]: 290.3901 g/mol, found: 312.9207 [M+Na].

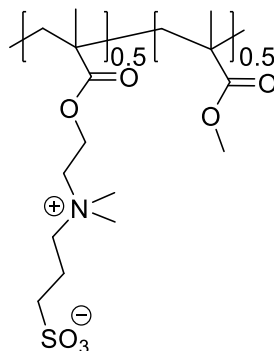
### Synthesis of ((*E*)-3,3'-butyl-5,5'-bithiazolidinylidene-4,4'-dione) (butyl-BT)



To a 20 mL scintillation vial, chilled to 0° C in an ice bath was added n-butylamine (2 equiv.) in DMF. Carbon disulfide (2 equiv.) was added dropwise and the resulting

yellow/orange solution was stirred for 10 minutes. Dimethylacetylene dicarboxylate (1 eq.) was then added dropwise, the dark solution was stirred for an additional 10 minutes. The solution was precipitated in cold methanol and the resulting orange crystals were collected by vacuum filtration and washed with methanol. The solid was dried under vacuum overnight to give the product in 45% yield (3.5 g).  $^1\text{H}$  NMR (500 MHz,  $\text{CDCl}_3$ )  $\delta$  (ppm): 4.13 (t, 4H,  $J = 7.6$  Hz.), 1.71 (t, 4H,  $J = 7.6$  Hz.), 1.40 (t, 4H,  $J = 7.5$  Hz.) 0.97 (t, 6H,  $J = 7.36$  Hz.).  $^{13}\text{C}$  NMR (126 MHz,  $\text{CDCl}_3$ )  $\delta$  194.49 (C=S), 166.90 (C=O), 124.67 (C=C), 44.55, 29.12, 20.04, 13.65. MALDI-MS: calculated for  $\text{C}_{14}\text{H}_{18}\text{N}_2\text{O}_2\text{S}_4$   $[\text{M}^+]$ : 374.0251 g/mol, found: 374.792.

### *Synthesis of PSBMA-co-PMMA*



SBMA (1 g, 3.6 mmol), MMA (0.36 g, 3.56 mmol), and AIBN (0.007 g, 0.045 mmol) in TFE (14 mL) were introduced in a 25 mL round-bottomed flask. The solution was degassed with  $\text{N}_2$  for 30 minutes before heating to  $70^\circ\text{C}$  in an oil bath. The reaction was allowed to stir at  $70^\circ\text{C}$  for 6 hours after which the reaction was quenched by exposure to oxygen. The polymer solution was purified by precipitation in methanol. The solid was collected by

centrifugation and washed several times with fresh methanol. The solid was then dried under vacuum overnight and lyophilized to remove excess water. Yield: 0.75 g, 55%

#### **Chemical Exfoliation of MoS<sub>2</sub>.**

MoS<sub>2</sub> nanosheets were prepared according to the method previously reported by Joenson *et al.* with minor modifications<sup>4</sup>. MoS<sub>2</sub> powder (0.3 g) was added to a flame-dried 50 mL round-bottom flask, equipped with a magnetic stir bar and a septum, and purged with N<sub>2</sub>. N-butyllithium (3.0 mL, 1.6 M in hexanes) was then added, and the resulting mixture was stirred for 2 days at room temperature. The solution was then diluted to *ca.* 40 mL with anhydrous hexanes and the suspension was filtered under a nitrogen nitrogen blanket (Millipore 0.45µm pore size). The Li-intercalated MoS<sub>2</sub> was then carefully introduced to 300 mL of Milli-Q water and sonicated at low power for 1 hour resulting in a black homogeneous suspension. The nanosheets were then dialyzed (10 kDa cutoff, Spectra/Por® (Spectrum Labs) regenerated cellulose) against deionized water for 5 days to remove residual salts. The sheets were used immediately to minimize restacking.

#### **MoS<sub>2</sub> suspension stabilization:**

To remove water, MoS<sub>2</sub> nanosheets were centrifuged at 10k rpm for 30 min. (1.5 mL per sample). The samples were decanted and polymers **PMMA**, **PBMA**, **PolyHexNB**, **P1a-e**, and **P4a-f** in THF were added to the remaining solid. The samples were then sonicated at low power for 30 min., after which the samples were monitored over the following days to assess the solution stability.

#### **Liquid exfoliation of MoS<sub>2</sub>:**

In a procedure by Neill and Khan<sup>5</sup>, MoS<sub>2</sub> powder (0.3 g) was suspended in NMP (30 mL). The solution was sonicated using a bath sonicator at high power for 1 hour. The resulting suspension was centrifuged at 3000 rpm for 10 min and the supernatant decanted which contained pristine MoS<sub>2</sub> nanosheets in low concentration. The homogeneous suspensions were used in further experiments as prepared.

### **Spectroelectrochemistry.**

*In situ* spectroelectrochemical data acquisition was performed on an Ocean Optics USB2000+XR spectrophotometer coupled with a BASi Epsilon potentiostat scanning voltage from -0.10 to 1.00 V. Spectral data were collected upon linear sweep voltammetry scans (50 mV/s scan rate) of the polymer films (drop-cast from a 10 mg/mL solution in toluene) on indium tin oxide (ITO)-coated glass slides (7 × 50 × 0.7 mm, sheet resistance,  $R_s = 8\text{--}12 \Omega/\text{cm}^2$ , purchased from Delta Technologies, Ltd.) in a 1 cm quartz cuvette. The experiments were performed in 0.1 M TBAPF<sub>6</sub> solution in acetonitrile under a nitrogen atmosphere using the ITO/glass slide as the working electrode, a silver wire pseudo-reference electrode, and a platinum wire as the counter electrode. For clarity, the absorption spectra obtained were smoothed using OriginPro 7.5 Adjacent Averaging function.

### **Kelvin Probe Force Microscopy (Mechanically exfoliated MoS<sub>2</sub>).**

MoS<sub>2</sub> (purchased from SPI Supplies) flakes were mechanically exfoliated on a glass substrate using the Scotch tape method<sup>6</sup> and located using photoluminescence imaging (ProEM512 camera, Princeton Instrument). AFM/KPFM measurements were then conducted on the selected MoS<sub>2</sub> nanosheets before and after polymer doping, recording the

differences in surface potential. Polymer doping was achieved by drop-casting a thin film of **P1e** from 0.001 mg/ml solution in THF. The glass substrates for KPFM were prepared plasma cleaning, rinsing with DI water, and subjecting to a NRD Static Control LLC. deionizer to remove the static charges.

### **Kelvin Probe Force Microscopy (CVD grown MoS<sub>2</sub>).**

KPFM was performed on MoS<sub>2</sub> that was CVD grown on Si/SiO<sub>2</sub> or sapphire substrates. The substrate was scanned initially to obtain the work function of the as-grown MoS<sub>2</sub> and then coated with a polymer (casted from a 0.001 mg/mL solution in CHCl<sub>3</sub>) and the same area was scanned again to monitor changes in the height and surface potential of the polymer-coated MoS<sub>2</sub>. A control was carried out by scanning MoS<sub>2</sub> before and after drop-casting chloroform on an area of interest. The figure above shows the height and SPC before and after coating along with height and SPC histograms showing almost no change in height and SPC after addition of chloroform.

### **Computational Methods.**

Density functional theory (DFT) calculations were performed using the Vienna *Ab Initio* Simulation Package (VASP).<sup>7</sup> The projector-augmented wave method was employed to represent core and valence electrons.<sup>8,9</sup> From convergence tests, a plane-wave cutoff of 400 eV was employed with a Brillouin zone sampling equivalent to a  $\Gamma$ -centered  $8\times 8\times 1$  mesh for the MoS<sub>2</sub> primitive cell. Electronic wavefunctions were converged to within  $10^{-4}$  eV in conjunction with a Gaussian smearing 0.05 eV. As semi-local DFT functionals do not account for van der Waals interactions, which we expect to be significant for adsorption of

TTF molecules on MoS<sub>2</sub>, we employed a non-local functional (optB86b-vdW<sup>10</sup> which is designed to capture van der Waals (vdW) interactions more accurately. Cell vectors for the MoS<sub>2</sub> monolayer were optimized with a force tolerance of 0.01 eV/Å using the optB86b-vdW functional; in subsequent calculations of adsorbed TTF, only atomic positions were relaxed with a force tolerance of 0.01 eV/Å keeping the cell vectors fixed at the optB86b-vdW-optimized value of 3.173 Å. These optB86b-optimized atomic positions were used without further relaxation for additional calculations using the Heyd-Scuseria-Ernzerhof (HSE) functional,<sup>11</sup> which is known to be more accurate for electronic structure calculations than semi-local functionals across a range of gapped and molecular systems.<sup>12</sup> Periodic images were separated by a minimum of 10 Å of vacuum normal to the MoS<sub>2</sub> sheet to prevent spurious interlayer coupling. Work functions were obtained as the difference between the vacuum level, calculated from the planar-averaged local potential (excluding the exchange-correlation potential), and the Fermi level. Dipole corrections<sup>13</sup> were found to be necessary only for the case of MoS<sub>2</sub> with a basal-plane sulfur vacancy; the work function in this case is reported as an average of the work functions calculated on the TTF and non-TTF sides of the structure. A Bader analysis was used to partition charge between the TTF molecule and MoS<sub>2</sub> monolayer from which the net charge transferred between the two constituents was estimated.<sup>14</sup> A 4×4 monolayer MoS<sub>2</sub> supercell was used in all calculations unless explicitly noted otherwise.

### **X-ray scattering (WAXS/SAXS)**

X-ray scattering was performed on film of polymer **P5b** casted from a 50 mg/mL solution onto a glass cover slip. The film was allowed to dry before being mounted onto a scattering



stage for analysis. The same film was annealed on a hotplate at 100 °C for 24 hours and subsequently analyzed again for domain size changes.

### **Graphene Synthesis and Device Fabrication**

Graphene was transferred to p-type silicon wafer with 285 nm oxide layer. The graphene was synthesized by CVD as described by others with some adaptations.<sup>15</sup> For graphene transfer, the copper was etched by ammonium persulfate (Merck, >98%). The graphene layer was formed into the desired shapes using AZ nLOF 2020 negative tone resist followed by oxygen plasma etch. On the top of the graphene bar, six electrodes (Ti/Pd 5/55 nm) were patterned by electron-beam lithography using PMMA and metallized by electron-beam evaporation followed by lift off.

### **Patterning of PSBMA–PMMA copolymer**

A solution of 10 mg PSBMA–PMMA copolymer was dissolved in 1 mL of TFE. The solution was stirred for 72 h at room temperature before use. The sample was spin-coated with the solution (500 rpm/5s, 3000 rpm/45s) and baked for 2 min at 120 °C on a hot plate. The polymer was exposed to a 30 kV e-beam (VEGA3, Tescan) with a dosage of 1200  $\mu\text{C}/\text{cm}^2$  and developed in preheated NMP (100 °C) for 3 min (for a clean silicon substrate) or 1 min (for a silicon/graphene substrate) followed by 30 s in air (allowing the sample to cool down gradually), soaked for 30s in IPA, and blow-dried by nitrogen flow.

## 7.4 References

1. Garin, J. *et al.* Improved Syntheses of Carboxytetrathiafulvalene, Formyltetrathiafulvalene and (Hydroxymethyl)tetrathiafulvalene: Versatile Building Blocks for New Functionalised Tetrathiafulvalene Derivatives. *Synthesis (Stuttg)*. 489–493 (1994).
2. Kreutzwiesner, E. *et al.* Contact Bactericides and Fungicides on the Basis of Amino-Functionalized Poly(norbornene)s. *J. Polym. Sci. Part A Polym. Chem.* **48**, 4504–4514 (2010).
3. Nasiri, F., Zolali, A. & Asadbegi, S. Solvent-free One-pot Synthesis of 2,2'-dithioxo-[5,5'] bithiazolidinylidene-4,4'-diones. *J. Heterocycl. Chem.* **53**, 989–992 (2015).
4. Joenson, P., Frindt, R. & Morrison, S. Single Layer MoS<sub>2</sub>. *MRS Bull.* **21**, 457–461 (1986).
5. Neill, A. O., Khan, U. & Coleman, J. N. Preparation of High Concentration Dispersions of Exfoliated MoS<sub>2</sub> with Increased Flake Size. *Chem. Mater.* **24**, 2414–2421 (2012).
6. Novoselov, K. S. *et al.* Two-dimensional atomic crystals. *Proc. Natl. Acad. Sci.* **102**, 10451–10453 (2005).
7. Kresse, G. & Furthmüller, J. Efficient iterative schemes for ab initio total-energy calculations using a plane-wave basis set. *Phys. Rev. B* **54**, 11169–11186 (1996).
8. P.E., B. Projector augmented-wave method. *Phys. Rev. B* **50**, 17953–17979 (1994).
9. Kresse, G. & Joubert, D. From ultrasoft pseudopotentials to the projector augmented-wave method G. *Phys. Rev. B* **59**, 1758–1775 (2013).
10. Klimes, J., Bowler, D. R. & Michaelides, A. Chemical accuracy for the van der Waals density functional. *J. Phys. Condens. Matter* **22**, (2010).
11. Heyd, J., Scuseria, G. & Ernzerhof, M. Hybrid functionals based on a screened Coulomb potential. *J. Chem. Phys.* **118**, 8207–8215 (2003).
12. Janesko, B. G., Henderson, T. M. & Scuseria, G. E. Screened hybrid density functionals for solid-state chemistry and physics. *Phys. Chem. Chem. Phys.* **11**, 443–454 (2009).
13. Neugebauer, J. & Scheffler, M. Adsorbate substrate and adsorbate adsorbate interactions of Na and K adlayers on Al(111). *Phys. Rev. B* **46**, 16067–16080

(1992).

14. Bader, R. F. W. A Quantum Theory of Molecular Structure and Its Applications. *Chem. Rev.* **91**, 893–928 (1991).
15. Yu, Q. *et al.* Control and characterization of individual grains and grain boundaries in graphene grown by chemical vapour deposition. *Nat. Mater.* **10**, 443–449 (2011).

## BIBLIOGRAPHY

- Aghgar, M. & Barnes, M. D. Work Function Modification in P3HT H/J Aggregate Nanostructures Revealed by Kelvin Probe Force Microscopy and Photoluminescence Imaging. *ACS Nano* 9, 7105–7112 (2015).
- Alon, H. et al. Lithographically Patterned Functional Polymer-Graphene Hybrids for Nanoscale Electronics. *ACS Nano* 12, 1928–1933 (2018).
- Bader, R. F. W. A Quantum Theory of Molecular Structure and Its Applications. *Chem. Rev.* 91, 893–928 (1991).
- Baghgar, M. et al. Morphology-dependent electronic properties in cross-linked (P3HT- b - P3MT) block copolymer nanostructures. *ACS Nano* 8, 8344–8349 (2014).
- Baik, S. S., Im, S. & Choi, H. J. Work Function Tuning in Two-Dimensional MoS<sub>2</sub> Field-Effect-Transistors with Graphene and Titanium Source-Drain Contacts. *Sci. Rep.* 7, 1–8 (2017).
- Ballesteros-Garrido, R., Rodriguez, R., Álvaro, M. & Garcia, H. Photochemistry of covalently functionalized graphene oxide with phenothiazinyl units. *Carbon*. 74, 113–119 (2014).
- Bangert, U. et al. Ion-beam modification of 2-D materials - single implant atom analysis via annular dark-field electron microscopy. *Ultramicroscopy* 176, 31–36 (2017).
- Banjoko, V., Xu, Y., Mintz, E. & Pang, Y. Synthesis of terpyridine-functionalized poly(phenylenevinylene)s: The role of meta -phenylene linkage on the Cu<sup>2+</sup> and Zn<sup>2+</sup> chemosensors. *Polymer*. 50, 2001–2009 (2009).
- Barnard, A. W. et al. Absorptive pinhole collimators for ballistic Dirac fermions in graphene. *Nat. Commun.* 8, 15418–15424 (2017).
- Bhimanapati, G. R. et al. Recent advances in two-dimensional materials beyond graphene. *ACS Nano* 9, 11509–11539 (2015).
- Bielawski, C. W. & Grubbs, R. H. Increasing the initiation efficiency of Ruthenium-based ring-opening metathesis initiators: Effect of excess phosphine. *Macromolecules* 34, 8838–8840 (2001).
- Cahen, D., Naaman, R. & Vager, Z. The cooperative molecular field effect. *Adv. Funct. Mater.* 15, 1571–1578 (2005).
- Canevet, D., Salle, M., Zhang, G., Zhang, D. & Zhu, D. Tetrathiafulvalene (TTF) derivatives: key building-blocks for switchable processes. *Chem. Commun.* 2245–2269 (2009). doi:10.1039/b818607n

- Cao, T. et al. Valley-selective circular dichroism of monolayer molybdenum disulphide. *Nat. Commun.* 3, (2012).
- Carozo, V. et al. Optical identification of sulfur vacancies: Bound excitons at the edges of monolayer tungsten disulfide. *Sci. Adv.* 3, 1–9 (2017).
- Cheianov, V. V., Fal, V. & Altshuler, B. L. The Focusing of Electron Flow and a Veselago Lens in Graphene p-n Junctions. *Science*, 315, 1252–1255 (2007).
- Chen, S. et al. Electron optics with ballistic graphene junctions. *Science*. 353, 1522–1525 (2016).
- Cheng, K. W. et al. Synthesis of Conjugated Polymers with Pendant Ruthenium Terpyridine Trithiocyanato Complexes and Their Applications in Heterojunction Photovoltaic Cells. *J. Polym. Sci. Part A Polym. Chem.* 46, 1305–1317 (2008).
- Cheng, R. et al. Electroluminescence and Photocurrent Generation from Atomically Sharp WSe<sub>2</sub>/MoS<sub>2</sub> Heterojunction p–n Diodes. *Nano Lett.* 14, 5590–5597 (2014).
- Chiang, P. T., Chen, N. C., Lai, C. C. & Chiu, S. H. Direct observation of mixed-valence and radical cation dimer states of tetrathiafulvalene in solution at room temperature: association and dissociation of molecular clip dimers under oxidative control. *Chem. - A Eur. J.* 14, 6546–6552 (2008).
- Choi, J., Zhang, H. & Choi, J. H. Modulating optoelectronic properties of two-dimensional transition metal dichalcogenide semiconductors by photoinduced charge transfer. *ACS Nano* 10, 1671–1680 (2016).
- Choi, Y. et al. On-demand doping of graphene by stamping with a chemically functionalized rubber lens. *ACS Nano* 9, 4354–4361 (2015).
- Chou, S. et al. Ligand Conjugation of Chemically Exfoliated MoS<sub>2</sub>. *J. Am. Chem. Soc.* 135, 4584–4587 (2013).
- Chung, C. et al. Biomedical applications of graphene and graphene oxide. *Acc. Chem. Res.* 46, 2211–2224 (2013).
- Coleman, J. N. et al. Two-Dimensional Nanosheets Produced by Liquid Exfoliation of Layered Materials. *Science* (80). 331, 568–572 (2011).
- Das, A. et al. Monitoring dopants by Raman scattering in an electrochemically top-gated graphene transistor. *Nat. Nano.* 3, 210–215 (2008).
- Dey, S., Matte, H. S. S. R., Shirodkar, S. N., Waghmare, U. V. & Rao, C. N. R. Charge-transfer interaction between few-layer MoS<sub>2</sub> and tetrathiafulvalene. *Chem. - An Asian J.* 8, 1780–1784 (2013).

- Ding, Q. *et al.* Basal-Plane Ligand Functionalization on Semiconducting 2H-MoS<sub>2</sub> Monolayers. *ACS Appl. Mater. Interfaces* 9, 12734–12742 (2017).
- Du, Y., Liu, H., Neal, A. T., Si, M. & Ye, P. D. Molecular Doping of Multilayer MoS<sub>2</sub> Field-Effect Transistors: Reduction in Sheet and Contact Resistances. *IEEE Electron Device Lett.* 34, 1328–1330 (2013).
- Duan, X. *et al.* Synthesis of WS<sub>2</sub>xSe<sub>2-2x</sub> Alloy Nanosheets with Composition-Tunable Electronic Properties. *Nano Lett.* 16, 264–269 (2016).
- Eda, G. *et al.* Photoluminescence from Chemically Exfoliated MoS<sub>2</sub>. *Nano Lett.* 11, 5111–5116 (2011).
- El Kazzi, S. *et al.* MoS<sub>2</sub> synthesis by gas source MBE for transition metal dichalcogenides integration on large scale substrates. *J. Appl. Phys.* 123, 1–6 (2018).
- Elder, R. M., Neupane, M. R. & Chantawansri, T. L. Stacking order dependent mechanical properties of graphene/MoS<sub>2</sub> bilayer and trilayer heterostructures. *Appl. Phys. Lett.* 107, (2015).
- Feng, Q. *et al.* Growth of MoS<sub>2(1-x)</sub>Se<sub>2(x = 0.41-1.00)</sub> Monolayer Alloys with Controlled Morphology by Physical Vapor Deposition. *ACS Nano* 9, 7450–7455 (2015).
- Ferrari, A. C. Raman spectroscopy of graphene and graphite: Disorder, electron-phonon coupling, doping and nonadiabatic effects. *Solid State Commun.* 143, 47–57 (2007).
- Filatre-Furcate, A., Higashino, T., Lorcy, D. & Mori, T. Air-stable n-channel organic field-effect transistors based on a sulfur rich  $\pi$ -electron acceptor. *J. Mater. Chem. C* 3, 3569–3573 (2015).
- Gabor, N. *et al.* Hot Carrier-Assisted Intrinsic Photoresponse in Graphene. *Science* 334, 648–652 (2011).
- Ganatra, R. & Zhang, Q. Few-layer MoS<sub>2</sub>: A promising layered semiconductor. *ACS Nano* 8, 4074–4099 (2014).
- Garin, J. *et al.* Improved Syntheses of Carboxytetrathiafulvalene, Formyltetrathiafulvalene and (Hydroxymethyl)tetrathiafulvalene: Versatile Building Blocks for New Functionalised Tetrathiafulvalene Derivatives. *Synthesis.* 489–493 (1994).
- Georgakilas, V. *et al.* Functionalization of graphene: Covalent and non-covalent approaches, derivatives and applications. *Chem. Rev.* 112, 6156–6214 (2012).
- Gu, T. *et al.* Regenerative oscillation and four-wave mixing in graphene optoelectronics. *Nat. Photonics* 6, 554–559 (2012).
- Guo, B. *et al.* Controllable N-doping of graphene. *Nano Lett.* 10, 4975–4980 (2010).

- Herring, P. K. *et al.* Photoresponse of an electrically tunable ambipolar graphene infrared thermocouple. *Nano Lett.* 14, 901–907 (2014).
- Heyd, J., Scuseria, G. & Ernzerhof, M. Hybrid functionals based on a screened Coulomb potential. *J. Chem. Phys.* 118, 8207–8215 (2003).
- Hsu, C.-L. *et al.* Layer-by-Layer Graphene/TCNQ Stacked Films as Conducting Anodes for Organic Solar Cells. *ACS Nano* 6, 5031–5039 (2012).
- Hu, Z. *et al.* Two-dimensional transition metal dichalcogenides: Interface and defect engineering. *Chem. Soc. Rev.* 47, 3100–3128 (2018).
- Huchet, L. *et al.* Spectroelectrochemistry of Electrogenerated Tetrathiafulvalene-Derivatized Poly(thiophenes): Toward a Rational Design of Organic Conductors with Mixed Conduction. *J. Phys. Chem. B* 102, 7776–7781 (1998).
- Ishihara, S. *et al.* Metallic versus Semiconducting SWCNT Chemiresistors: A Case for Separated SWCNTs Wrapped by a Metallosupramolecular Polymer. *ACS Appl. Mater. Interfaces* 9, 38062–38067 (2017).
- Jaeger, C. D. & Bard, A. J. Electrochemical Behavior of Tetrathiafulvalene-Tetracyanoquinodimethane Electrodes in Aqueous Media. *J. Am. Chem. Soc.* 101, 1690–1699 (1979).
- Janesko, B. G., Henderson, T. M. & Scuseria, G. E. Screened hybrid density functionals for solid-state chemistry and physics. *Phys. Chem. Chem. Phys.* 11, 443–454 (2009).
- Jariwala, D., Sangwan, V. K., Lauhon, L. J., Marks, T. J. & Hersam, M. C. Emerging device applications for semiconducting two-dimensional transition metal dichalcogenides. *ACS Nano* 8, 1102–1120 (2014).
- Jeong, K. S., Deng, Z., Keuleyan, S., Liu, H. & Guyot-Sionnest, P. Air-stable n-doped colloidal HgS quantum dots. *J. Phys. Chem. Lett.* 5, 1139–1143 (2014).
- Jing, Y., Tan, X., Zhou, Z. & Shen, P. Tuning electronic and optical properties of MoS<sub>2</sub> monolayer via molecular charge transfer. *J. Mater. Chem. A* 2, 16892–16897 (2014).
- Joenson, P., Frindt, R. & Morrison, S. Single Layer MoS<sub>2</sub>. *MRS Bull.* 21, 457–461 (1986).
- Kang, D. *et al.* Controllable Nondegenerate p-Type Doping of Tungsten Diselenide by Octadecyltrichlorosilane. *ACS Nano* 9, 1099–1107 (2015).
- Kaplan, M. L., Haddon, R. C., Wudl, F. & Feit, E. D. Preparation of Some Monophenyltetrathiafulvalenes and (p-Vinylphenyl)tetrathiafulvalene and Its Polymerization. *J. Org. Chem.* 43, 4642–4646 (1978).

- Kappera, R. *et al.* Phase-engineered low-resistance contacts for ultrathin MoS<sub>2</sub> transistors. *Nat. Mater.* 13, 1128–1134 (2014).
- Kim, B. J. *et al.* High-performance flexible graphene field effect transistors with ion gel gate dielectrics. *Nano Lett.* 10, 3464–3466 (2010).
- Kim, E. *et al.* Site Selective Doping of Ultrathin Metal Dichalcogenides by Laser-Assisted Reaction. *Adv. Mater.* 28, 341–346 (2016).
- Kim, Hyunwoo; Abdala, Ahmed; Macosco, C. Graphene/Polymer Nanocomposites. *Macromolecules* 43, 6515–6530 (2010).
- Kim, S. M. *et al.* Role of Anions in the AuCl<sub>3</sub> Doping of Carbon Nanotubes. *ACS Nano* 5, 1236–1242 (2011).
- Kiriya, D., Tosun, M., Zhao, P., Kang, J. S. & Javey, A. Air-stable surface charge transfer doping of MoS<sub>2</sub> by benzyl viologen. *J. Am. Chem. Soc.* 136, 7853–7856 (2014).
- Klimes, J., Bowler, D. R. & Michaelides, A. Chemical accuracy for the van der Waals density functional. *J. Phys. Condens. Matter* 22, (2010).
- Knott, E. B. & Jeffreys, R. A. Compounds Containing Sulphur Chromophores. Part II. Attempts to Prepare Sulphide Analogues of Merocyanines. *J. Chem. Soc.* 927–933 (1955).
- Kresse, G. & Furthmüller, J. Efficient iterative schemes for ab initio total-energy calculations using a plane-wave basis set. *Phys. Rev. B* 54, 11169–11186 (1996).
- Kresse, G. & Joubert, D. From ultrasoft pseudopotentials to the projector augmented-wave method. *Phys. Rev. B* 59, 1758–1775 (2013).
- Kreuzwiesner, E. *et al.* Contact Bactericides and Fungicides on the Basis of Amino-Functionalized Poly(norbornene)s. *J. Polym. Sci. Part A Polym. Chem.* 48, 4504–4514 (2010).
- Krupka, J., Derzakowski, K., Tobar, M., Hartnett, J. & Geyer, R. G. Complex permittivity of some ultra-low loss dielectric crystals at cryogenic temperatures. *Meas. Sci. Technol.* 10, 387–392 (1999).
- Kümmel, S. & Kronik, L. Orbital-dependent density functionals: Theory and applications. *Rev. Mod. Phys.* 80, 3–60 (2008).
- Lalezari, I. & Shafiee, A. 1,2,3-Selenadiazole and Its Derivatives. *J. Org. Chem.* 36, 2836–2838 (1971).



- Lalezari, I., Shafiee, A., Khorrami, J. & Soltani, A. Selenium Heterocycles XXII: Synthesis and Antibacterial and Antifungal Activities of Arylsulfonyl-1,2,3-selenadiazoles. *J. Pharm. Sci.* 67, 1336–1338 (1978).
- Lanzillo, N. A., Simbeck, A. J. & Nayak, S. K. Strain engineering the work function in monolayer metal dichalcogenides. *J. Phys. Condens. Matter* 27, (2015).
- Le Gal, Y. *et al.* A sulfur-rich  $\pi$ -electron acceptor derived from 5,5'-bithiazolidinylidene: Charge-transfer complex: Vs. charge-transfer salt. *CrystEngComm* 18, 3925–3933 (2016).
- Lee, C. *et al.* Anomalous Lattice Vibrations of Single- and Few-Layer MoS<sub>2</sub>. *ACS Nano* 4, 2695–2700 (2010).
- Lee, H. *et al.* Poly(sulfobetaine methacrylate)s as electrode modifiers for inverted organic electronics. *J. Am. Chem. Soc.* 137, 540–549 (2015).
- Lee, S. K. *et al.* Inverse transfer method using polymers with various functional groups for controllable graphene doping. *ACS Nano* 8, 7968–7975 (2014).
- Lemme, M. C. *et al.* Gate-activated photoresponse in a graphene p-n junction. *Nano Lett.* 11, 4134–4137 (2011).
- Li, F. *et al.* Layer Dependence and Light Tuning Surface Potential of 2D MoS<sub>2</sub> on Various Substrates. *Small* 13, 1–8 (2017).
- Li, X. *et al.* One-step hydrothermal synthesis of high-percentage 1T-phase MoS<sub>2</sub> quantum dots for remarkably enhanced visible-light-driven photocatalytic H<sub>2</sub> evolution. *Appl. Catal. B Environ.* 243, 76–85 (2019).
- Li, Y. *et al.* MoS<sub>2</sub> nanoparticles grown on graphene: An advanced catalyst for the hydrogen evolution reaction. *J. Am. Chem. Soc.* 133, 7296–7299 (2011).
- Li, Y. *et al.* Photoluminescence of monolayer MoS<sub>2</sub> on LaAlO<sub>3</sub> and SrTiO<sub>3</sub> substrates. *Nanoscale* 6, 15248–15254 (2014).
- Lin, X. & Ni, J. Charge and magnetic states of Mn-, Fe-, and Co-doped monolayer MoS<sub>2</sub>. *J. Appl. Phys.* 116, (2014).
- Liscio, A. *et al.* Local surface potential of  $\pi$ -conjugated nanostructures by Kelvin Probe Force microscopy: Effect of the sampling depth. *Small* 7, 634–639 (2011).
- Liu, T. *et al.* Drug delivery with PEGylated MoS<sub>2</sub> nano-sheets for combined photothermal and chemotherapy of cancer. *Adv. Mater.* 26, 3433–3440 (2014).
- Liu, X. *et al.* P-Type Polar Transition of Chemically Doped Multilayer MoS<sub>2</sub> Transistor. *Adv. Mater.* 28, 2345–2351 (2016).

- Liu, Z. *et al.* Preparation of graphene/polymer composites by direct exfoliation of graphite in functionalised block copolymer matrix. *Carbon*. 51, 148–155 (2013).
- Love J., P., Morgan J., Trnka. T. & Grubbs. R. A Practical and Highly Active Ruthenium-Based Catalyst that Effects the Cross Metathesis of Acrylonitrile. *Angew. Chemie Int. Ed.* 41, 4035–4037 (2002).
- Lowe, A. B., Hoyle, C. E. & Bowman, C. N. Thiol-yne click chemistry: A powerful and versatile methodology for materials synthesis. *J. Mater. Chem.* 20, 4745–4750 (2010).
- Ly, T. H. *et al.* Observing grain boundaries in CVD-grown monolayer transition metal dichalcogenides. *ACS Nano* 8, 11401–11408 (2014).
- Mak, K. F. *et al.* Observation of tightly bound trions in monolayer MoS<sub>2</sub>. *Nat. Mater.* 12, 207–211 (2012).
- Maryanoff, B. E. & Rebarchak, M. C. Unusual Medium Effect on the Distribution of 1,2,3-Selenadiazole Regioisomers in the Reaction of N-Benzyl-4-homopiperidinone Semicarbazone with Selenium Dioxide. *J. Org. Chem.* 56, 5203–5207 (1991).
- Mei, Y. *et al.* Interface engineering to enhance charge injection and transport in solution-deposited organic transistors. *Org. Electron. physics, Mater. Appl.* 50, 100–105 (2017).
- Meier, H. & Menzel, I. Formation of Cyclo-octyne by Pyrolysis of Cyclo-octeno- 1,2,3-selenadiazole. *J. Chem. Soc. D Chem. Commun.* 1059 (1971).
- Melitz, W., Shen, J., Kummel, A. C. & Lee, S. Kelvin probe force microscopy and its application. *Surf. Sci. Rep.* 66, 1–27 (2011).
- Mouri, S., Miyauchi, Y. & Matsuda, K. Tunable photoluminescence of monolayer MoS<sub>2</sub> via chemical doping. *Nano Lett.* 13, 5944–5948 (2013).
- Nachman, M. & Kwiatkowski, K. The effect of thermal annealing on the abrasion resistance of a segmented block copolymer urethane elastomers. *Wear* 306, 113–118 (2013).
- Nagase, H. Studies on Fungicides. XXV. Addition Reaction of Dithiocarbamates to Fumaronitrile, Bis(alkylthio)maleonitrile, 2,3,-Dicyano-5,6-dihydro-1,4-dithiin and 4,5-Dicyano-2-oxo-1,4-dithiol. *Chem. Pharm. Bull.* 22, 505–513 (1973).
- Nagase, H. Studies on Fungicides. XXII. Reaction of Dimethyl Acetylenedicarboxylate with Dithiocarbamates, Thiocarbamates, Thiosemicarbazides and Thiosemicarbazones. *Chem. Pharm. Bull.* 21, 279–286 (1972).

- Nasiri, F., Zolali, A. & Asadbegi, S. Solvent-free One-pot Synthesis of 2,2'-dithioxo-[5,5'] bithiazolidinylidene-4,4'-diones. *J. Heterocycl. Chem.* 53, 989–992 (2015).
- Neill, A. O., Khan, U. & Coleman, J. N. Preparation of High Concentration Dispersions of Exfoliated MoS<sub>2</sub> with Increased Flake Size. *Chem. Mater.* 24, 2414–2421 (2012).
- Neugebauer, J. & Scheffler, M. Adsorbate substrate and adsorbate adsorbate interactions of Na and K adlayers on Al(111). *Phys. Rev. B* 46, 16067–16080 (1992).
- Novoselov, K. S. *et al.* Electric Field Effect in Atomically Thin Carbon Films. *Science* (80). 306, 666–669 (2004).
- Novoselov, K. S. *et al.* Two-dimensional atomic crystals. *Proc. Natl. Acad. Sci.* 102, 10451–10453 (2005).
- Osim, W., Stojanovic, A., Akbarzadeh, J., Peterlik, H. & Binder, W. H. Surface modification of MoS<sub>2</sub> nanoparticles with ionic liquid-ligands: Towards highly dispersed nanoparticles. *Chem. Commun.* 49, 9311–9313 (2013).
- P.E., B. Projector augmented-wave method. *Phys. Rev. B* 50, 17953–17979 (1994).
- Palermo, V., Palma, M. & Samori, P. Electronic characterization of organic thin films by Kelvin probe force microscopy. *Adv. Mater.* 18, 145–164 (2006).
- Park, C., Son, Y., Yang, L., Cohen, M. L. & Louie, S. G. Electron Beam Supercollimation in Graphene Superlattices. *Nano Lett.* 8, 2920–2924 (2008).
- Park, I. J. *et al.* Stretchable thin-film transistors with molybdenum disulfide channels and graphene electrodes. *Nanoscale* 10, 16069–16078 (2018).
- Pittman, C. U., Mitsuru, U. & Liang, Y. F. Synthesis and Polymerization of p-(2-Tetrathiafulvalenyl)phenyl Methacrylate. *J. Org. Chem.* 44, 3639–3642 (1979).
- Radisavljevic, B., Radenovic, A., Brivio, J., Giacometti, V. & Kis, A. Single-layer MoS<sub>2</sub> transistors. *Nat. Nanotechnol.* 6, 147–150 (2011).
- Rapoport, L. *et al.* Tribological properties of WS<sub>2</sub> nanoparticles under mixed lubrication. *Wear* 255, 785–793 (2003).
- Refaely-Abramson, S. *et al.* Gap renormalization of molecular crystals from density-functional theory. *Phys. Rev. B - Condens. Matter Mater. Phys.* 88, 1–5 (2013).
- Ren, X. *et al.* A Se-doped MoS<sub>2</sub> nanosheet for improved hydrogen evolution reaction. *Chem. Commun.* 51, 15997–16000 (2015).

- Rigato, V. *et al.* Properties of sputter-deposited MoS<sub>2</sub>/metal composite coatings deposited by closed field unbalanced magnetron sputter ion plating. *Surf. Coatings Technol.* 131, 206–210 (2000).
- Rong, L. *et al.* Impact of defects on local optical dielectric properties of Si/SiO<sub>2</sub> interfaces by layered capacitor modeling. *Appl. Phys. A Mater. Sci. Process.* 122, 1–8 (2016).
- Rosentsveig, R. *et al.* Fullerene-like MoS<sub>2</sub> nanoparticles and their tribological behavior. *Tribol. Lett.* 36, 175–182 (2009).
- Roy, T. *et al.* Dual-Gated MoS<sub>2</sub>/WSe<sub>2</sub> van der Waals Tunnel Diodes and Transistors. *ACS Nano* 9, 2071–2079 (2015).
- Sánchez, V., Benavente, E., Ana, M. A. S. & González, G. High electronic conductivity molybdenum disulfide-dialkylamine nanocomposites. *Chem. Mater.* 11, 2296–2298 (1999).
- Sandonas, L. M., Gutierrez, R., Pecchia, A., Seifert, G. & Cuniberti, G. Tuning quantum electron and phonon transport in two-dimensional materials by strain engineering: A Green's function based study. *Phys. Chem. Chem. Phys.* 19, 1487–1495 (2017).
- Secor, E. B., Ahn, B. Y., Gao, T. Z., Lewis, J. A. & Hersam, M. C. Rapid and Versatile Photonic Annealing of Graphene Inks for Flexible Printed Electronics. *Adv. Mater.* 27, 6683–6688 (2015).
- Selhorst, R. C. *et al.* Tetrathiafulvalene-containing polymers for simultaneous non-covalent modification and electronic modulation of MoS<sub>2</sub> nanomaterials. *Chem. Sci.* 7, 4698–4705 (2016).
- Selhorst, R., Wang, P., Barnes, M. & Emrick, T. Bithiazolidinylidene polymers: Synthesis and electronic interactions with transition metal dichalcogenides. *Chem. Sci.* 9, 5047–5051 (2018).
- Shastry, T. A. *et al.* Mutual Photoluminescence Quenching and Photovoltaic Effect in Large-Area Single-Layer MoS<sub>2</sub>-Polymer Heterojunctions. *ACS Nano* (2016). doi:10.1021/acsnano.6b06592
- Shimizu, T. & Yamamoto, T. Preparation of a new poly(arylacetylene) with a tetrathiafulvalene (TTF) unit in the side chain. *Chem. Commun.* 515–516 (1999). doi:10.1039/a900300b
- Shlimak, I. *et al.* Raman scattering and electrical resistance of highly disordered graphene. *Phys. Rev. B - Condens. Matter Mater. Phys.* 91, 3–6 (2015).
- Shon, Y. S. & Lee, T. R. Catalytic ring-closing olefin metathesis of sulfur-containing species: Heteroatom and other effects. *Tetrahedron Lett.* 38, 1283–1286 (1997).

- Sim, D. M. *et al.* Controlled Doping of Vacancy-Containing Few-Layer MoS<sub>2</sub> via Highly Stable Thiol-Based Molecular Chemisorption. *ACS Nano* 9, 12115–12123 (2015).
- Sinturel, C., Vayer, M., Morris, M. & Hillmyer, M. Solvent Vapor Annealing of Block Polymer Thin Films. *Macromolecules* 46, 5399–5415 (2013).
- Splendiani, A. *et al.* Emerging photoluminescence in monolayer MoS<sub>2</sub>. *Nano Lett.* 10, 1271–1275 (2010).
- Spruell, J. M. *et al.* Highly stable tetrathiafulvalene radical dimers in [3]catenanes. *Nat. Chem.* 2, 870–879 (2010).
- Stanford, M. G. *et al.* High Conduction Hopping Behavior Induced in Transition Metal Dichalcogenides by Percolating Defect Networks: Toward Atomically Thin Circuits. *Adv. Funct. Mater.* 27, 1–9 (2017).
- Tan, S. J. R. *et al.* Temperature- and Phase-Dependent Phonon Renormalization in 1T'-MoS<sub>2</sub>. *ACS Nano* 12, 5051–5058 (2018).
- Tanachutiwat, S., Lee, J., Wang, W. & Sung, C. Reconfigurable Multi-Function Logic Based on Graphene pn Junctions. *Proc. 47th Des. Autom. Conf. ACM* 883–888 (2010).
- Tian, X. *et al.* Effects of 3d transition-metal doping on electronic and magnetic properties of MoS<sub>2</sub> nanoribbons. *Phys. Chem. Chem. Phys.* 17, 1831–1836 (2015).
- Venkata Subbaiah, Y. P., Saji, K. J. & Tiwari, A. Atomically Thin MoS<sub>2</sub>: A Versatile Nongraphene 2D Material. *Adv. Funct. Mater.* 26, 2046–2069 (2016).
- Wang, H. *et al.* Integrated circuits based on bilayer MoS<sub>2</sub> transistors. *Nano Lett.* 12, 4674–4680 (2012).
- Wang, P. & Barnes, M. D. Disentangling 'bright' and 'dark' Interactions in Ordered Assemblies of Organic Semiconductors. *Nano Lett.* 17, 6949–6953 (2017).
- Wieting, T. J. & Verble, J. L. Infrared and Raman Studies of Long-Wavelength Optical Phonons in Hexagonal MoS<sub>2</sub>. *Phys. Rev. B* 3, 4286–4292 (1971).
- Williams, J. R., Low, T., Lundstrom, M. S. & Marcus, C. M. Gate-controlled guiding of electrons in graphene. *Nat. Nanotechnol.* 6, 222–225 (2011).
- Wu, S. *et al.* Vapor-Solid Growth of High Optical Near-Unity Valley Polarization Quality MoS<sub>2</sub> Monolayers with. *ACS Nano* 7, 2768–2772 (2013).
- Xia, F., Farmer, D. B., Lin, Y. M. & Avouris, P. Graphene field-effect transistors with high on/off current ratio and large transport band gap at room temperature. *Nano Lett.* 10, 715–718 (2010).

- Xia, F., Farmer, D. B., Lin, Y. M. & Avouris, P. Graphene field-effect transistors with high on/off current ratio and large transport band gap at room temperature. *Nano Lett.* 10, 715–718 (2010).
- Xue, Y., Xiao, H. & Zhang, Y. Antimicrobial polymeric materials with quaternary ammonium and phosphonium salts. *Int. J. Mol. Sci.* 16, 3626–3655 (2015).
- Yan, J., Zhang, Y., Kim, P. & Pinczuk, A. Electric field effect tuning of electron-phonon coupling in graphene. *Phys. Rev. Lett.* 98, 1–4 (2007).
- Yingjie, L. *et al.* Multiphase Structure of a Segmented Polyurethane: Effects of Temperature and Annealing. *Macromolecules* 25, 7365–7372 (1992).
- Yoon, Y., Ganapathi, K. & Salahuddin, S. How good can monolayer MoS<sub>2</sub> transistors be? *Nano Lett.* 11, 3768–3773 (2011).
- Yore, A. E. *et al.* Visualization of Defect-Induced Excitonic Properties of the Edges and Grain Boundaries in Synthesized Monolayer Molybdenum Disulfide. *J. Phys. Chem. C* 120, 24080–24087 (2016).
- Yoshizawa, M., Kumazawa, K. & Fujita, M. Room-temperature and solution-state observation of the mixed-valence cation radical dimer of tetrathiafulvalene, [(TTF)<sub>2</sub>]<sup>+</sup>, within a self-assembled cage. *J. Am. Chem. Soc.* 127, 13456–13457 (2005).
- Yu, Q. *et al.* Control and characterization of individual grains and grain boundaries in graphene grown by chemical vapour deposition. *Nat. Mater.* 10, 443–449 (2011).
- Yu, Y. *et al.* High phase-purity 1T'-MoS<sub>2</sub>- and 1T'-MoSe<sub>2</sub>-layered crystals. *Nat. Chem.* 10, 638–643 (2018).
- Yu, Y.-J. J. *et al.* Tuning the graphene work function by electric field effect. *Nano Lett.* 9, 3430–3434 (2009).
- Yue, D. *et al.* Passivated ambipolar black phosphorus transistors. *Nanoscale* 8, 12773–12779 (2016).
- Zhang, H. *et al.* Ba<sup>2+</sup> Doped CH<sub>3</sub>NH<sub>3</sub>PbI<sub>3</sub> to Tune the Energy State and Improve the Performance of Perovskite Solar Cells. *Electrochim. Acta* 254, 165–171 (2017).
- Zhang, Q. *et al.* Bandgap renormalization and work function tuning in MoSe<sub>2</sub>/hBN/Ru(0001) heterostructures. *Nat. Commun.* 7, 1–7 (2016).
- Zhang, R. *et al.* Authigenic buffer layer: Tuning surface work function in all polymer blend solar cells. *Colloids Surfaces A Physicochem. Eng. Asp.* 535, 149–156 (2017).

Zou, X. & Yakobson, B. I. An open canvas - 2D materials with defects, disorder, and functionality. *Acc. Chem. Res.* 48, 73–80 (2015).